

DEVELOPMENT OF A NOVEL ENERGY LOSS OPTICAL SCINTILLATION SYSTEM
FOR HEAVY-ION PARTICLE IDENTIFICATION

By

Sean David Dziubinski

A DISSERTATION

Submitted to
Michigan State University
in partial fulfillment of the requirements
for the degree of

Physics — Doctor of Philosophy

2025

ABSTRACT

The Energy Loss Optical Scintillation System (ELOSS) is a novel optical readout-based gaseous detector currently under development at the Facility for Rare Isotope Beams (FRIB). It is designed to enable rapid Z -identification of rare, short-lived atomic nuclei within the S800 spectrograph. Together, the S800 spectrometer and focal plane detector system employ a $B\rho$ - ΔE - ToF method to identify nuclear reaction residues. Currently, energy loss (ΔE) measurements are obtained using a gaseous transmission detector (ionization chamber), while time-of-flight (ToF) measurements are recorded with plastic scintillators positioned at two distinct locations. The atomic number (Z) is deduced according to the Bethe-Bloch equation using the ΔE and ToF . ELOSS is anticipated to significantly advance the particle identification (PID) capabilities of the S800 by offering a two-fold improvement in energy loss resolution and a detection rate increase greater than ten-fold.

The ELOSS detector comprises a large volume filled with Xenon gas. As charged particles cross the ELOSS volume they deposit energy in Xenon, producing scintillation light (approximately 175 nm) along their track. Arrays of photomultiplier tubes (PMTs), with sensitivity optimized for the Xenon emission spectrum, surround the detector's effective volume to capture the scintillation light. The high electron density of Xenon, combined with its exceptional scintillation yield (approximately 20 ph/keV for heavy ions), results in low collisional straggling and a high signal-to-noise ratio, contributing to an energy resolution of approximately 0.6% σ ($Z \sim 50$). The full emission spectrum of Xenon is emitted within a few hundred nanoseconds, characterized by decay constants of 6 ns (singlet state) and 99 ns (triplet state), allowing for a fast detector response and a detection rate of approximately 50 kHz, primarily limited by the data acquisition system (DAQ).

This thesis will detail the design and construction of the main ELOSS components,

including the PMT-based optical readout responsible for recording scintillation light from excited Xenon gas, the implementation of an external decoupling circuit for simultaneous high voltage (HV) supply and anode signal readout, the development of a suitable DAQ for processing the PMT signals, and the assembly of the mechanical support for the optical readout. Additionally, the development of a cryogenic rare gas recovery and storage system to support ELOSS operation with ultra-expensive Xenon gas is discussed.

A signal processing method using a deep neural network algorithm to correct position-dependent energy loss measurements will be explored. Position dependence arises from non-uniform light collection efficiency, which is typical of large-area scintillation detectors. This also involves the introduction of a systematic calibration of PMT anode sensitivities to correct tube-to-tube variations and achieve a deviation of less than 1% throughout the entire array. Finally, results from two fast beam tests of the ELOSS detector and its current status will be presented.

I dedicate this work to... some very important people that I haven't had the time to thank yet.

ACKNOWLEDGMENTS

1. This material is based upon work supported by the U.S. Department of Energy, Office of Science, Office of Nuclear Physics and used resources of the Facility for Rare Isotope Beams (FRIB), which is a DOE Office of Science User Facility, operated by Michigan State University, under Award Number DE-SC0000661.
2. Work supported by the US Department of Energy, Office of Science, High Energy Physics under Cooperative Agreement award number DE-SC0018362 and Michigan State University.

TABLE OF CONTENTS

LIST OF TABLES	viii
LIST OF FIGURES	ix
Chapter 1. Introduction	1
Chapter 2. Background	4
2.1 Brief Overview of the S800 Spectrograph	4
2.2 Heavy-Ion Particle Identification in a Large Acceptance Spectrometer	7
2.2.1 Magnetic Rigidity and PID	7
2.2.2 Time-of Flight and PID	9
2.2.3 Energy Loss and PID (Bethe-Bloch)	9
2.2.4 Total Kinetic Energy and PID	12
2.3 Focal plane detectors	13
2.4 PID Resolution Requirements for Increasing Z	16
2.5 ELOSS: A New Type of Energy-Loss Detector	21
2.5.1 Advantages of High- Z Gas	21
2.5.2 Xenon as a High Z , High-Luminescence Gas	25
2.5.2.1 Collection of Prompt Scintillation	26
2.5.2.2 Xenon Excimers and a VUV Wavelength	27
2.5.2.3 Primary and Secondary Scintillation Yields	29
2.5.3 Energy Loss Optical Scintillation System (ELOSS)	31
Chapter 3. Simulation-based Design Studies	33
3.1 Geant4	33
3.2 Detector Optimization	33
3.2.1 Photosensors	34
3.2.2 Geometry	37
3.3 Expected performance	39
Chapter 4. ELOSS Design and Components	41
4.1 Optical Readout	41
4.1.1 Photomultiplier Tubes	41
4.1.2 Reflector foils	44
4.2 Mechanical Structure	46
4.2.1 ELOSS vessel	46
4.2.2 Optical readout mechanical support	48
4.2.3 Pressure windows	49
4.3 Gas Handling System	51
4.4 Interfaces	56
4.4.1 The Lid	56
4.4.2 Decoupler Crate	57

4.4.3	ELOSS Channel Mapping	63
4.5	Data Acquisition System	65
Chapter 5. PMT anode sensitivity calibration		71
5.1	Introduction	71
5.2	Defining the anode sensitivity	71
5.3	Anode sensitivity calibration methodology	73
5.4	Description of the Calibration Setup	77
5.4.1	Initial Characterization	77
5.4.2	Course gain correction	79
5.4.3	Fine-tune gain correction	80
5.5	Results	87
5.6	Discussion	93
Chapter 6. Optimization and Further Studies with a Deep Neural Network		99
6.1	Introduction	99
6.2	Photon collection efficiency and photon-counting resolution	100
6.3	Deep Neural Network	104
6.4	Results	106
6.4.1	Position reconstruction	106
6.4.2	Energy loss after correction from position reconstruction	108
6.4.3	Tracking capabilities (angular)	109
6.4.4	Adding noise	110
6.4.5	Adding PMT anode sensitivity	112
6.4.6	Missing PMTs	114
Chapter 7. Experimental Results		117
7.1	Experiment 1	117
7.2	Experiment 2	123
7.2.1	Description	123
7.2.2	Results	125
7.3	Prototype Verification	134
Chapter 8. Discussion		139
BIBLIOGRAPHY		144
APPENDIX A. Channel Mapping		151
APPENDIX B. Arduino Motor Controller Code		156

LIST OF TABLES

Table 2.1: Concentration of Sn for different gate sizes with 3σ separation	18
Table 2.2: Summary of scintillation yields for Xenon	30
Table 3.1: Scintillation properties of GXe set in the ELOSS Geant4 application [37] [38]	34
Table 4.1: MDPP parameters	69
Table 5.1: MDPP parameters	86

LIST OF FIGURES

Figure 2.1:	3D model of the S800 Spectrograph including the Analysis line. A cartoon nucleus is depicted on the left entering the analysis line with a Cartesian coordinate system extending from it. The z -axis always point in the direction of the beam and is sometimes called the s -coordinate in accelerator physics because it is measured relative to accelerator components/optics.	4
Figure 2.2:	Focused mode optics of the S800 analysis line and spectrometer.	5
Figure 2.3:	Dispersion-matched mode optics of the S800 analysis line and spectrometer.	6
Figure 2.4:	Model of the S800 focal plane detector system.	13
Figure 2.5:	Picture of the S800 ionization chamber (IC) based on a stack of 16 large-area parallel plate ion chambers. The biasing scheme is labeled at the top of the IC and the electrodes made of aluminized polypropylene foil are pointed out.	14
Figure 2.6:	Illustration of 3σ separation in a histogram of equally represented Z . The left peak corresponds to In, middle to Sn, and right to Sb. 68% of Sn is within $-\sigma$ to σ , 95% in $\pm 2\sigma$ and 99.7% in $\pm 3\sigma$	17
Figure 2.7:	The $\frac{\delta Z}{Z}$ needed to achieve 3σ separation for different Z with respect to $Z \pm 1$	19
Figure 2.8:	$\frac{\delta Z}{Z}$ as a function of $\frac{\delta \Delta E}{\Delta E}$ is plotted in the solid line and the goal $\frac{\delta Z}{Z}$ is plotted with a dashed line. With zero change in ToF resolution, the energy loss resolution would need to lower to 0.6% to get $\frac{\delta Z}{Z}$ low enough to separate Z in the uranium region.	20
Figure 2.9:	Excitation and de-excitation processes for high and low pressure systems of Xe gas.	28
Figure 3.1:	Optical readout configurations	35
Figure 3.2:	ELOSS concept schematic showing four sectors divided by reflective electrodes.	37
Figure 3.3:	Optical readout configurations	38
Figure 3.4:	PID performance with the R8520 PMT configuration.	39

Figure 4.1:	Spectral responses for R8520 PMTs. The peak quantum efficiency, indicated by the arrow from R8520-406, is 30% at 175 nm.	42
Figure 4.2:	Voltage distribution ratio from R8520 PMT datasheet.	42
Figure 4.3:	Voltage-divider and anode signal readout circuit.	44
Figure 4.4:	Top left: close up view of one PMT voltage-divider in Altium 2D viewer. Top right: close up view of one PMT voltage-divider in Altium 3D viewer. Bottom: entire vertical-side PCB in Altium 2D viewer.	45
Figure 4.5:	Updated 2D ELOSS concept schematic including the chessboard-like PMT placement pattern. The side profile is from the viewpoint of looking in from the right side of the detector if the right side was taken away. . . .	46
Figure 4.6:	3D CAD drawing of the ELOSS vessel with the optical readout support and PMTs installed inside. No pressure windows or reflector foils.	47
Figure 4.7:	Left side: ELOSS optical readout (attached to lid) being lowered into the detector vessel. The crane connects to the four anchor points on the lid. Right side: one crane attaches to the top anchor point and another holds the legs of ELOSS (legs are for installation on a moving table discussed later). Lifting the top rotates the detector smoothly.	48
Figure 4.8:	Optical readout support assembled without PMTs or reflector foils.	49
Figure 4.9:	Front pressure window made of kevlar reinforced dyneema is installed on the ELOSS vessel.	50
Figure 4.10:	Schematic for the ELOSS Gas Handling System (GHS) used as a reference during operation. Labels each pressure gauge, valve, vacuum pumps and components in the same format as the procedure documents.	52
Figure 4.11:	Phase diagram for Xenon [42] with the melting point (MP) [43] and boiling point (BP) [44] indicated on the graph.	53
Figure 4.12:	Drawing of Xenon Recovery System operational principle. As the cryotrap is submerged in liquid nitrogen, Xenon is drawn into the low-pressure cryotrap where it freezes.	54
Figure 4.13:	3D model of the ELOSS vessel lid. It contains six 25-pin DSUB feedthroughs spaced down the middle, five BNC feedthroughs, and six SHV feedthroughs at the bottom of the lid.	57
Figure 4.14:	Optical readout connections schematic.	58

Figure 4.15: Decoupler Crate front panel under construction	59
Figure 4.16: Decoupler circuit that delivers the HV bias to the PMT feedthrough and decouples the bias and anode signal pulse ahead of the MDPP input.	59
Figure 4.17: Altium 2D view of decoupler PCB. Contains 16 decoupler circuits shown in Figure 4.16 and three board edge connectors.	60
Figure 4.18: Altium 3D view of decoupler PCB.	60
Figure 4.19: Top: 3D model of PMT IO adapter. Bottom: back panel view of the decoupler crate installed in the ELOSS electronics rack.	61
Figure 4.20: Circuit used to simulate the performance of the decoupler circuit and connections to the crate, namely the mismatched impedances over long cable lengths.	62
Figure 4.21: Signal measured across the 50 Ω resistor resembling the readout electronics' input showing a compromise between reflections due to impedance mismatches and an acceptable signal-to-noise ratio.	62
Figure 4.22: Schematic of PMT locations for the used naming convention.	63
Figure 4.23: More detailed PMT location schematic with full naming convention. Includes PMT serial numbers and cables/channel numbers. Each color on the outer perimeter boxes corresponds to a cable assembly.	64
Figure 4.24: HV channel mapping showing three Iseg modules of 48 channels is connected to the decoupler crate and distributed to eight decoupler PCBs with the HV adapter board.	65
Figure 4.25: Signal readout mapping taking 16 signals per decoupler PCB to a input of one of the four MDPP32-QDC modules. Modules are named after their software address and the outputs of the modules are imported in the FRIBDAQ as Tcl tree parameters following the same naming as the QDC channels.	66
Figure 4.26: MDPP schematic of hardware and software components.	67
Figure 5.1: Photoelectron collection efficiency as a function of the potential difference between the photocathode and first dynode.	76
Figure 5.2: Initial characterization setup for the anode sensitivity calibration.	78

Figure 5.3:	PMT base PCB used for the initial characterization of each PMT. PCB is fastened to calibration stand support structure and its components are painted with insulating varnish to prevent discharges.	79
Figure 5.4:	Left-hand side: LED-bias pulse in blue with shape loosely representative of Xenon’s triplet decay scintillation and the NIM-like DAQ trigger pulse in yellow. Right-hand side:	80
Figure 5.5:	Voltage-divider schematic for the first two stages of the calibration. The custom potentiometer was utilized in the second stage only in place of R8 and R9.	80
Figure 5.6:	3D model of the PMT Gain Correction Stand used for the fine-tuned gain corrections with a UV-C LED.	81
Figure 5.7:	Up close view of LED holder assembly. It fastens to the nut of the ball screw and top of the slider block to group the separate components together.	83
Figure 5.8:	Arduino shield PCB containing the interface between the operator, Arduino, motor driver, motor and limit switches.	85
Figure 5.9:	Example of a PMT’s initial characterization, measuring the anode sensitivity as a function of the voltage supplied.	87
Figure 5.10:	Comparison of the anode sensitivities measured by Hamamatsu in “current mode” and anode sensitivities measured in “pulse mode” for this study.	88
Figure 5.11:	Left hand side: example of a few PMT sensitivity curves with respect to the center-stage resistor ratio. Right hand side: same plots of left hand side normalized by their maximum.	89
Figure 5.12:	Anode sensitivities measured for all 120 PMTs after the course gain correction for 3 different light intensities. Dashed lines represent the target sensitivity for each light intensity.	90
Figure 5.13:	Example of anode sensitivity measured as a function of the PMT bias after the course calibration. The red dotted line represents the exponential fit using the sensitivities measured from 700 V to 850 V and the black dashed line represents the exponential fit using sensitivities only from 700 V to 800 V.	91
Figure 5.14:	Same as Figure 5.12, but after supplying the PMTs with the calculated calibrated voltages.	92

Figure 5.15: Same as Figure 5.14, but after the final calibration process.	93
Figure 5.16: Comparison between the original anode sensitivities recorded for each PMT at 800 V in the PMT Gain Correction Stand and the repeat of that measurement after calibration.	94
Figure 5.17: Paschen curves for common gases [?].	95
Figure 5.18: Anode sensitivity for two PMTs at each LED intensity setting. Measured in four different environments (listed in order left to right): initial Ar/air mixture at 720 Torr, Ar at 800 Torr, and air at atmosphere with two different LED connections.	96
Figure 5.19: Left: Anode sensitivity as a function of the positional offset from the targeted position detailed in the Arduino code. Right: anode sensitivity as a function of offset after adjusting the starting position of the LED to account for offset in the left figure.	98
Figure 6.1: GEANT4 generated map of the average number of photons recorded by the ELOSS optical readout as a function of the position (X,Y) of $^{80}\text{Se}^{34+}$ particle impinging on the detector area.	100
Figure 6.2: Number of photons detected by the ELOSS optical readout as a function of the position of the beam particles (with an energy of 140 MeV/u) along the x-coordinate (600 mm wide). A simulation was conducted for isotopes with atomic numbers of 28 to 35.	101
Figure 6.3: Number of photons detected by the ELOSS optical readout for beam particles with atomic numbers 28 to 35 and 140 MeV/u. The photon count peaks representing each Z are indistinguishable.	102
Figure 6.4: Panel a) An analysis of the correlation between the y-coordinate position of the beam particles used as input for GEANT4 and the values estimated by the DNN algorithm processing the simulation data outputs. Panel b) show a close up section of the correlation graph at the center of the detector.	107
Figure 6.5: Position resolution (calculated for the X axis on the left graph and the Y axis on the right one) provided by the DNN by processing the light distribution recorded by the PMTs.	107
Figure 6.6: Panel a) shows same data as Figure ?? corrected for the variation of the photon collection efficiency. Panel b) PID plot obtained from the projection of panel a) along the y-axis. All the simulated isotope are well separated - $\Delta Z_{\sigma}/Z = 0.5\%$	108

Figure 6.7:	Same as Figure 6.5 but for particle tracks with a non-normal angle of impact with respect to the ELOSS entrance windows.	109
Figure 6.8:	Intrinsic angular resolution obtained by tracking the trajectory of the particle in the ELOSS volume using the DNN algorithm applied to the data (light distributions) recorded in each sector of the ELOSS optical readout.	110
Figure 6.9:	Degradation effects on localization capability (left graph) and on energy resolution (right graph) by a progressively increased noise level on the simulated light signals.	111
Figure 6.10:	Total number of photons detected by ELOSS from a GEANT4 simulation of 3000 ^{59}Ni particles uniformly irradiating the effective area with an energy of 140 MeV/u. The photon counts for each PMT were adjusted based on the anode sensitivity of that PMT measured after coarse gain correction and after fine-tune gain correction.	113
Figure 6.11:	Total number of photons detected by ELOSS (same simulation as Figure 6.10). Photon counts were set to zero for a number of PMTs to simulate “inactive” PMTs.	114
Figure 6.12:	Same as Figure 6.11, but the inactive PMT signals were replaced with the average of its neighbors before being input to the neural network algorithm.	116
Figure 7.1:	Drawings of the E22507 location and setup with the ELOSS detector, movable table, and representations of the electronics rack and GHS. ELOSS is positioned 38” downstream of dipole BTS13:D2169, centered with the future S2 vault beamline.	118
Figure 7.2:	Schematic drawing of viewer plate installed on the entrance window of ELOSS. Viewer plate has a cross pattern of fiducials with 1 cm separation center-to-center.	119
Figure 7.3:	ELOSS Moving Table consisting of a pneumatic cylinder controlled scissor-lift for vertical motion and a motorized linear actuator mounted on the bottom of the truck platform with the wheels controlled the horizontal motion.	120
Figure 7.4:	The total charge collected on the electrode foils/energy lost as a function of the voltage supplied to the foils.	126
Figure 7.5:	Dimensions and composition of SRIM target material based on ELOSS dimensions.	127

Figure 7.6:	Orange plot is the preamplifier output if the input pulse was a delta function/integration time was infinite. Blue plot is an example preamplifier output with 100 μ s integration time and input pulse \sim 31 μ s long.	130
Figure 7.7:	Comparison of the voltage-divider and readout circuit currently used in ELOSS (left) and the proposed redesign (right). Circuit model contains the last two multiplication stages, anode, and decoupler circuit. For the same input pulse, the redesigned circuit outputs a signal 50,000 times larger.	132
Figure 7.8:	Prototype used to test the initial concepts for ELOSS. Consists of 12 PMTs with the decoupler circuit inside the prototype, such that each PMT needed a HV cable and signal cable.	135
Figure 7.9:	Picture of PMT responses to stimulated electroluminescence inside the prototype with an Ar/Xe mixture.	136
Figure 7.10:	The same prototype structure as in Figure 7.8, but more accurate spacing of foils, redesigned PMT voltage-divider PCBs, external decoupling circuit, and coaxial PMT cables.	137
Figure A.1:	152
Figure A.2:	153
Figure A.3:	154
Figure A.4:	155

Chapter 1. Introduction

The Energy Loss Optical Scintillation System (ELOSS) [1] is an innovative, highly-luminescent gaseous detector currently under development at the Facility for Rare Isotope Beams (FRIB) [2]. As part of the S800 spectrograph upgrade, ELOSS is expected to significantly enhance atomic number (Z) identification through a two-fold improvement in energy loss resolution and a ten-fold increase in counting rate capability compared to the current technology in the S800 focal plane detector system [3]. The S800 is a high-rigidity, large-acceptance spectrograph used for nuclear reaction experiments with radioactive beams produced by projectile fragmentation on targets [4]. The spectrometer and focal plane detector system of the S800 implement a $B\rho - \Delta E - ToF$ method for identifying short-lived nuclear reaction residues. The energy loss (ΔE) measurement is achieved using a gaseous transmission detector (i.e., an ionization chamber - IC), while the time of flight (ToF) measurement is recorded with plastic scintillators at two different locations. The atomic number is deduced according to the Bethe-Bloch equation using the ΔE and ToF measurements.

Over the next several years, the FRIB Power Ramp-Up program will increase primary beam power from the present 20 kW to the 400 kW design specification [5]. As a result, secondary beam intensity will increase, enabling experiments to use heavier, more exotic nuclei, which in turn poses significant performance challenges for focal plane detectors. In response, ELOSS is built to meet these challenges with an innovative design that collects prompt scintillation produced along particle tracks, rather than relying on ionized charge drifting to large-area electrode foils as in the IC.

ELOSS is structurally similar to the conventional Frisch grid-less ionization chamber, constructed in a multi-sampling, parallel-plate configuration for the S800 [6]. However, ELOSS

is distinguished by its arrays of photosensors that surround the sensitive gas volume. In this configuration, the electrode foils, traditionally used for collecting ionized charge, primarily function as mirrors that direct scintillation toward the photosensors lining the perimeter of each ion chamber segment. This optical readout-based ΔE detector leverages its low-noise environment, dictated by ambient light rather than electronic noise induced on large-area capacitive foils, to enhance the scientific reach of the S800. The combination of superior energy resolution and counting rate capability will extend the particle identification (PID) range of the S800 focal plane past the current maximum ($Z=50$), while simultaneously exploiting cocktail beams produced in low beam purity settings instead of being limited by them. Ultimately, this means taking a significant step towards realizing the unprecedented discovery potential of FRIB and providing new opportunities for rare-isotope beam experiments in nuclear astrophysics and nuclear structure. The aim of these experiments, among other objectives, is to investigate the unbound states of dripline nuclei, halo nuclei structure, and general spectroscopy for a wide range of nuclei.

The subsequent chapters will delve deeper into the technical aspects and experimental results of ELOSS. This will begin with a comprehensive background discussion, which includes an overview of the $B\rho - \Delta E - ToF$ method and its application to the S800 focal plane detector system. Additionally, a brief literature review of the current technology for Z -identification utilized in heavy-ion experiments and the physics principles governing the optimal operation of an optical readout-based gaseous detector like ELOSS will be provided in Chapter 2. Chapters 3 and 4 will take the detector concepts discussed in the first three chapters and integrate them into a detector design through GEANT4 simulation studies (Chapter 3) and finally a complete physical construction (Chapter 4). Chapter 5 will present the methodology, implementation, and outcome of a sensitivity calibration for

the photosensors making up the ELOSS optical readout. A neural network-based position reconstruction algorithm is discussed in Chapter 6 for correcting the energy loss variation due to position-dependent light collection efficiency. Chapter 7 will discuss the setup and results of two fast-beam experiments with ELOSS and the most recent prototype testing in response to the results of the last fast-beam experiment. Finally, Chapter 8 will discuss the implications of ELOSS detector development and how this impacts the S800 spectrograph and future iterations of ELOSS such as for High Rigidity Spectrometer [?].

Chapter 2. Background

2.1 Brief Overview of the S800 Spectrograph

Magnetic spectrometers can take on a variety of forms, from compact tabletop devices to towering mass spectrometers that stand three stories high. These instruments are capable of measuring properties such as the mass, charge, and energy of nuclear reaction products, providing valuable insights into the structure and behavior of atomic nuclei. At FRIB, intense beams of radioactive isotopes are produced and delivered to secondary beam experiments, including those conducted with the S800 spectrograph [4]. This allows researchers to study nuclei by comparing ions before and after they interact with a thin target placed in front of the S800 spectrometer, facilitating a deeper understanding of nuclear properties and reactions.

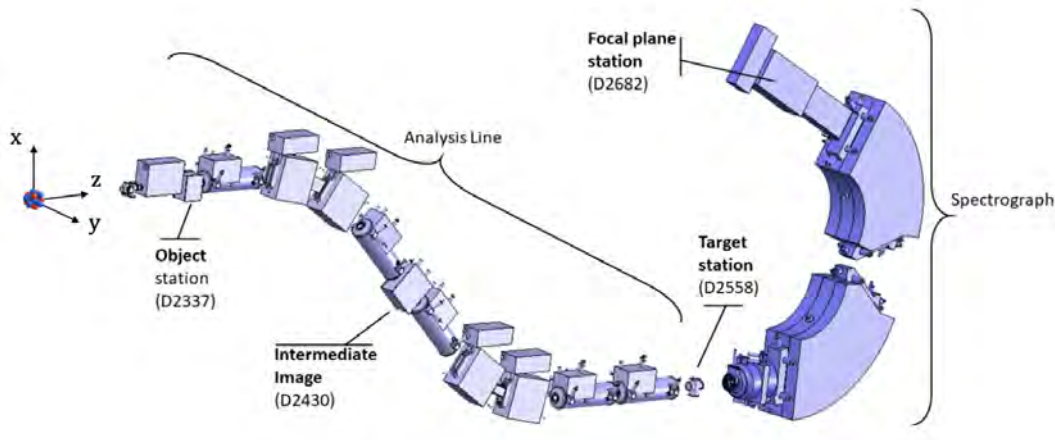


Figure 2.1: 3D model of the S800 Spectrograph including the Analysis line. A cartoon nucleus is depicted on the left entering the analysis line with a Cartesian coordinate system extending from it. The z -axis always point in the direction of the beam and is sometimes called the s -coordinate in accelerator physics because it is measured relative to accelerator components/optics.

Figure 2.1 presents a model of the S800 spectrograph, encompassing the analysis line,

target station, spectrometer section (dipole magnets), and the focal plane. The analysis line serves to transport and analyze the beam impinging on the target and to shape the beam's position and momentum profile for various operating modes of the S800. In focus mode (see Figure 2.2), the beam is achromatic in the analysis line and dispersed in the focal plane image [7]. The position along the dispersive axis of the focal plane image is correlated to particle momentum. To improve the measurement of momentum change resulting from nuclear interactions at the target, the momentum of each incoming particle must be tracked. Running in this mode provides the largest momentum acceptance ($\pm 2\%$).

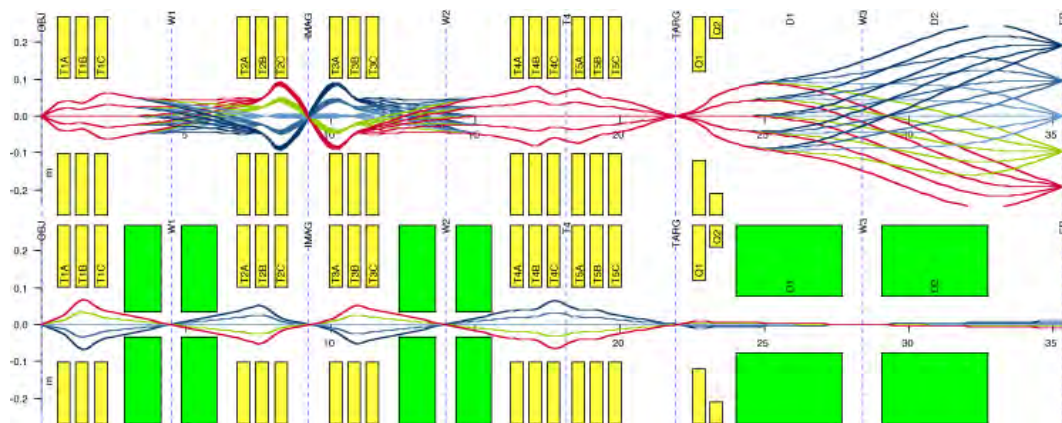


Figure 2.2: Focused mode optics of the S800 analysis line and spectrometer.

In dispersion matched mode (see Figure 2.3), a dispersed beam, with position dependent on incoming momentum, is delivered to the target [7]. The analysis line is configured to match the dispersion of the spectrometer section, resulting in an achromatic image in the focal plane. Consequently, any change in momentum from the nuclear reaction will manifest as an offset in the focal plane image, eliminating the need for momentum tracking. While momentum acceptance is smaller in this mode ($\pm 0.5\%$) and thus transmission, the energy resolution is about five times better than in focus mode.

While these simple descriptions of each mode provide a basic understanding, real exper-

2.2 Heavy-Ion Particle Identification in a Large Acceptance Spectrometer

Experiments utilizing the S800 spectrograph aim to gather a wide range of data, including scattering angles, excitation energies, cross sections, etc [4]. The ability to interpret these experimental results and accurately determine particle and reaction properties hinges on the spectrograph's proficiency in identifying reaction products and correlating the measured properties with specific isotopes. Isotopes, in the simplest sense, are defined and distinguished by their atomic number (Z) and mass (A). For heavy-ion beams, a mix of isotopes with multiple charge states is nearly unavoidable, especially after the beam interacts with a target. Therefore, identifying reaction products must also include the charge state (Q). PID in the S800 spectrometer uses a $B\rho - \Delta E - ToF$ method to obtain the Z and $\frac{A}{Q}$ for every reaction product reaching the focal plane. By measuring TKE in addition, A and Q can be disentangled.

2.2.1 Magnetic Rigidity and PID

Magnetic rigidity, a fundamental property of charged particles in motion, quantifies a particle's resistance to deflection in a magnetic field. This property is directly related to the particle's momentum-to-charge ratio and is mathematically represented as $B\rho$ in Equation 2.1.

$$B\rho = \frac{p}{q} \tag{2.1}$$

$B\rho$ plays a critical role in the identification of charged particles using magnetic spectrom-

eters such as the S800. In any experiment, the S800 spectrometer optics are tuned to bend a beam of momentum p (and a momentum spread δp dependent on the optics mode) by 60° in the XZ -plane toward the focal plane station. This controlled spectrometer rigidity, $B\rho_0$, generates a focal plane image that encodes the momentum-to-charge ratio of the particles. By analyzing the particle trajectories and their positions at the focal plane within a known magnetic field, the momentum-to-charge ratio can be determined. However, this property alone is insufficient for complete particle identification. Additional analysis is necessary, but a good starting point is with Equation 2.2.

$$B\rho = \frac{uA\gamma\beta c}{eQ} \quad (2.2)$$

Here, u is the atomic mass unit, γ is the Lorentz factor, $\beta = \frac{v}{c}$ is the relativistic velocity, c is the speed of light and e is the charge of an electron. $B\rho$ is the magnetic rigidity of the particle calculated from the particle's position at the focal plane and the magnetic rigidity of the spectrometer, $(B\rho)_0$:

$$B\rho = B\rho_0(1 + \delta) \quad (2.3)$$

where $\delta = \frac{\Delta p}{p} = \frac{\Delta x}{x_0}$ is the fractional deviation of the particle with respect to the ideal spectrometer trajectory or center position. Putting Equation 2.2 into quantities that can be measured by focal plane detectors (ToF and Δx) and known properties of the beam or spectrometer results in:

$$\frac{uAc}{eQ(\frac{c^2 ToF^2}{L^2} - 1)^{1/2}} = (B\rho)_0(1 + \frac{\Delta x}{x_0}). \quad (2.4)$$

Solve Equation 2.4 for $\frac{A}{Q}$:

$$\frac{A}{Q} = \frac{e}{uc}(B\rho)_0\left(1 + \frac{\Delta x}{x_0}\right)\left(\frac{c^2 T_{of}^2}{L^2} - 1\right)^{1/2} \quad (2.5)$$

For a beam with a uniform velocity, the positional offset would indicate the $\frac{A}{Q}$ directly, but more realistic beam conditions possess a spread in momentum/velocity because the beam is delivered in bunches of a definite size (not point-like). Therefore, velocity must be determined and this is done by measuring the time-of-flight.

2.2.2 Time-of Flight and PID

Velocity is calculated using the time-of-flight measurement. Velocity is defined as change in position over change in time in the laboratory frame. The time is recorded when a particle enters the spectrograph and recorded again when it reaches the end of the spectrograph. The distance between where the particle was at each time stamp is L . Hence, the time-of-flight from point a to point b is used to deduce the velocity. With this velocity, $\frac{A}{Q}$ can finally be calculated. However, this alone does not identify any isotope. What is needed next is the Z .

2.2.3 Energy Loss and PID (Bethe-Bloch)

When ions pass through matter, they interact with atoms in a variety of ways. For heavy-ion projectiles, Coulomb interactions tend to dominate within the target material [9]. The electric field of the ion and the electric fields of every target atom and their electrons are all simultaneously interacting with every source of charge. Therefore, the traveling ion feels the Coulomb force from all around. The electric field produced by a point particle in vacuum falls off as $1/r^2$ making the strongest force coming from target atoms for which

the projectile ion passes by in close proximity. The Coulomb Barrier discourages direct inelastic collisions between nuclei and promotes elastic collisions that transfer energy from the moving ion to a target atom. That energy transfer depends on several factors including charge, velocity, impact parameter, etc. Energy is lost by the ion and transferred to the atom it “collides” with. “Collides” is used loosely since these collisions occur over distances much larger than the size of the colliding particles. Energy exchanged in this way can be spent in an atom in many ways, but the most interesting for detector physics are the generation of a photon and the liberation of an electron. The number of photons or electron-ion pairs created are dictated by individual Coulomb interactions following Poisson statistics, but an average energy per scintillation photon w_{sc} or electron-ion pair w_1 can be used to obtain a reasonable estimation of the energy loss based on the proportional detected light or charge. The scintillation photon generated from the de-excitation of an electron and the free electron knocked out by ionization act as vessels for information about the projectile ion.

The energy needed to generate one photon or one electron from a specific material atom is relatively consistent for a particle type and target material. Therefore, by counting the number of photons produced or electron-ion pairs produced, the energy from the incident ion lost to the target material can be deduced. Derived from Rutherford’s expression for the scattering cross-section [10], the Bethe-Bloch formula [9] in Equation 2.6 is a semi-classical approach (including quantum corrections) that describes the energy lost by a charged particle, in matter, per unit length.

$$-\frac{dE}{dx} = \frac{8\pi N e^2 Z^2 \rho \tilde{Z}}{m_e c^2 \beta^2 \tilde{A}} \left[\ln \frac{2mc^2 \beta^2}{I(1 - \beta^2)} - \beta^2 - \frac{C}{Z} - \frac{\delta}{2} \right] \quad (2.6)$$

Here, N is Avogadro’s number, m_e and e are the mass and charge of an electron, Z is the

atomic number of the incoming ion, \tilde{Z} , \tilde{A} and ρ are the atomic number, mass and density of the target material, and β is the ion's velocity. Inside the correctional terms, I is the ionization potential, $\frac{C}{Z}$ is the inner shell correction that take into account screening effects, and $\frac{\delta}{2}$ is a density effect correction that for gases is negligible [9].

The Bethe-Bloch equation (Equation 2.6) simplifies quite nicely when comparing the energy loss of ions in the same detector medium because it only depends on the charge and velocity of the ion. The charge of the ion is represented by eZ . Hence, Bethe-Bloch assumes ions are fully-stripped. This will become an important point later, but for now this relationship can be simplified to

$$-\frac{dE}{dx} \propto \frac{Z^2}{\beta^2} \rightarrow Z \sim \sqrt{\Delta E \cdot \left(\frac{L}{cToF}\right)^2} \quad (2.7)$$

By integrating the equation on the left side of the arrow, over the distance a projectile travels through the effective detector volume, ΔE is deduced. The right side of the arrow rearranges the left side to solve for Z in terms of properties (L) and measurements (ΔE , ToF) from the spectrograph.

To summarize the particle identification method discussed so far, magnetic rigidity is calculated from the tracking information measured in the target and focal plane to deduce each reaction product's $\frac{A}{Q}$. However, magnetic rigidity doesn't provide the $\frac{A}{Q}$ alone, the β needs to be evaluated as well. The velocity is determined by the time-of-flight over a fixed distance within the spectrometer. With the help of an energy loss measurement, velocity is also used to find Z . Unfortunately, fully-stripped heavy ions are prone to picking up electrons as they pass through a target. Q does not equal Z in these cases. The presence of different charge states complicates the identification of isotopes using Bethe-Bloch. Q can change multiple

times as an ion travels through material, picking up and losing electrons, which makes ΔE proportional to a Q that changes over time leading to worsening energy resolution and consequently degraded identification performance. Also, Q changes in a stochastic manner with little correlation to Z , loosening the connection between Z and ΔE . This can be seen in the two dimensional PID plot - Figure X - that graphs Z vs. $\frac{A}{Q}$. Multiple charge states for each Z widen the distributions in the ΔE axis, which mixes different Z together until they are indistinguishable. Adding a third dimension Q can disentangle overlapping isotopes by spreading them out in the Q coordinate as Figure X shows.

2.2.4 Total Kinetic Energy and PID

An additional measurement that can be added to the focal plane is the total kinetic energy.

The relativistic total kinetic energy is given by Equation 2.8:

$$TKE = (\gamma - 1)mc^2 \quad (2.8)$$

Here, the mass m of the projectile nuclei is unknown, but can be solved for once TKE is measured because γ is already known from ToF . Once the mass is calculated, Q can be found. First solve for m :

$$m = \frac{TKE}{(\gamma - 1)c^2} \quad (2.9)$$

Substitute m for $u(\frac{A}{Q})Q$ and solve for Q :

$$Q = \frac{TKE}{(\gamma - 1)uc^2\frac{A}{Q}} \quad (2.10)$$

Now Q is expressed in variables deduced from the other focal plane detectors and known properties. Similarly, A is calculated as well. The expressions for Z , A , and Q have been given in this section in terms of variables that can be measured by the S800 spectrograph using the analysis line, dipole section and focal plane detector system.

2.3 Focal plane detectors

The focal plane detector system consists of two cathode readout drift chambers (CRDCs), a Frisch gridless ionization chamber, plastic scintillator and hodoscope of 32 CsI(Na) crystals, shown in Figure 2.4, for measuring the magnetic rigidity, energy loss, time-of-flight and total kinetic energy [3].

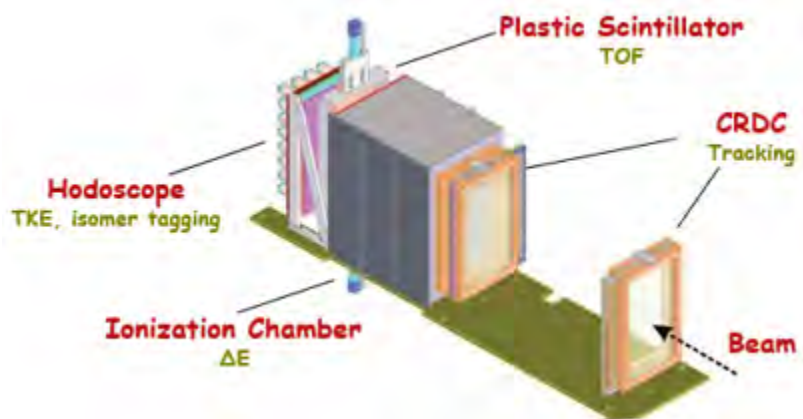


Figure 2.4: Model of the S800 focal plane detector system.

The CRDCs provide tracking information for the focal plane. Each CRDC has a $56 \times 26 \text{ cm}^2$ active area filled with $\text{CF}_4/(20\%)\text{iC}_4\text{H}_{10}$ at about 40 Torr [11]. The CRDCs measure the x and y coordinates of particles traversing them with position resolution less than 1 mm FWHM in the dispersive and non-dispersive coordinates. The Δx measured with the first CRDC is used to calculate $B\rho$, and subsequently goes into computing $\frac{A}{Q}$. Additionally, the CRDCs are spaced 1 m apart so the position can be recorded at different points along its

trajectory in the focal plane. The momentum vector can be reconstructed from the angles measured with this information and utilized in corrections to magnetic rigidity, energy loss, and time-of-flight.

The energy loss in the S800 focal plane is recorded by a stack of 16 parallel plate, Frish grid-less ionization chambers (IC) - see Figure 2.5. Each chamber is 1.5 cm thick and the detector is filled with 300-600 Torr of P10 (90% Ar, 10% methane) gas depending on the velocity and Z of the isotope of interest.

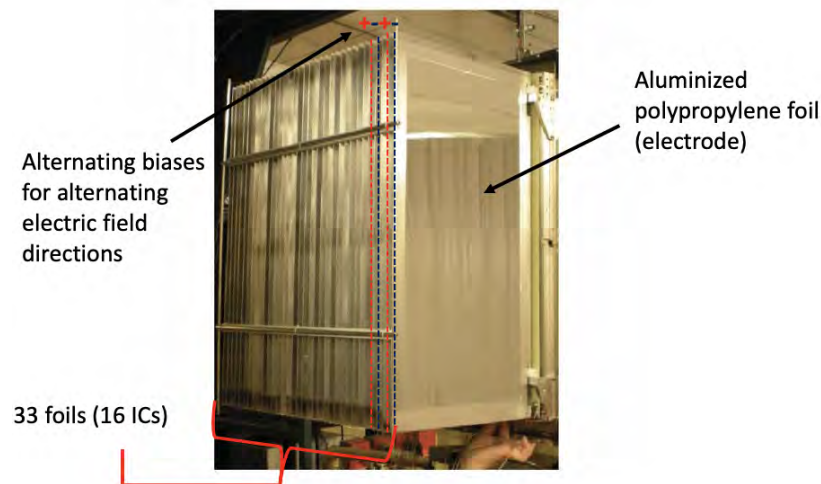


Figure 2.5: Picture of the S800 ionization chamber (IC) based on a stack of 16 large-area parallel plate ion chambers. The biasing scheme is labeled at the top of the IC and the electrodes made of aluminized polypropylene foil are pointed out.

The energy loss is calculated by the total charge induced on the electrode foils from drifting the electrons and ions in an electric field. The charge and energy loss are proportional by the ionization potential of the detection gas. The foils are biased at different voltages (typically 0 V and +200 V) such that the potential difference generates an electric field 0.133 kV/cm^2 [11]. The foils are biased so that they have an alternating polarity. This means the charge induced on one foil is actually the charge produced in the gas volumes on each side of the foil. The current induced on the foils is sent into small charge sensitive

preamplifiers inside the chamber that outputs a low-noise pulse with amplitude proportional to the total induced charge. This pulse is passed into a shaping amplifier and then into an analog-to-digital converter (ADC) to bin pulse heights proportional to the energy loss recorded.

The limitations of the ionization chamber are similar to the drift chambers. Drifting charge is slow and for large energy loss the build up of ions in the detection volume create space charge effects for high beam rates. Additionally, each ionization chamber segment is comprised of two large-area parallel foils that create a noisy environment due to the high capacitance between foils. This is remedied partially by stacking 16 ionization chambers together to lower the overall capacitance and thus the noise. With the low signal-to-noise ratio, the IC is limited to an energy resolution about 1.2% σ and the rate capability is limited to around 5 kHz [3].

There are two plastic scintillators used in the S800 spectrograph to measure time-of-flight. One is located in the object plane of the analysis line, which starts the time-of-flight counter. The other is in the focal plane between the ionization chamber and the hodoscope. The following will concentrate on the focal plane scintillator. There are two options for scintillator thickness (1 mm and 5 mm). The thicker detector is opted for in experiments using lighter ions to increase the total energy loss in the detector and consequently increase timing resolution. The scintillation is readout by photomultiplier tubes (PMTs) that are optically coupled to the scintillator on the top and bottom of the large scintillator. The intrinsic detector resolution for a point particle sized beam is around 100 ps. However, for highly dispersed beams in the focal plane, the resolution is degraded significantly (up to 1 ns) by the path length differences of traversing nuclei [11].

The S800 measures TKE at the focal plane with the a hodoscope positioned at the very

end of the focal plane box, doubling as a beam stop [11]. The hodoscope is positioned downstream of the E1 scintillator and is the last detector in the focal plane where the beam must stop. The hodoscope is composed of 32 sodium-doped cesium iodide CsI(Na) scintillating crystals. Each crystal is 5.1 cm thick and 7.6 cm in both transverse directions defining the 57.76 cm^2 crystal active area. In total, the hodoscope covers the same $60 \times 30 \text{ cm}^2$ active area of the upstream focal plane detectors by arranging the crystals in an 8×4 layout [12]. White Teflon reflective material optically isolates the crystals from each other. A particle's TKE is equal to the energy lost in the hodoscope since the particle stops in the crystals.

2.4 PID Resolution Requirements for Increasing Z

Heavy-ion beams, with energies ranging from 100 to 150 MeV/u, surpass the Coulomb barrier, enabling direct interactions between projectile and target nuclei [13]. A plethora of nuclear reactions are possible, but projectile fragmentation is by far the most prevalent in this regime. The cross-sections for projectile fragmentation increase with beam energy, while other reaction mechanisms diminish [12]. Employing thin, low- Z targets in combination with carefully selected ion beams facilitates the production of specific isotopes. Even so, nuclei exiting the target generally exhibit a broad range of Z , A , Q , and energy states. Consequently, the focal plane detectors must effectively separate isotopes with Z , A , and Q values differing by as little as 1. Over the past two decades, a minimum 3σ separation between Z and $Z \pm 1$ or A and $A \pm 1$ has been the benchmark for reliable and efficient PID. This 3σ range includes 99.7% of the data for a given Z within $Z \pm 1$. Figure 2.6 illustrates the application of the 3σ rule, using $Z = 50$ as a representative example.

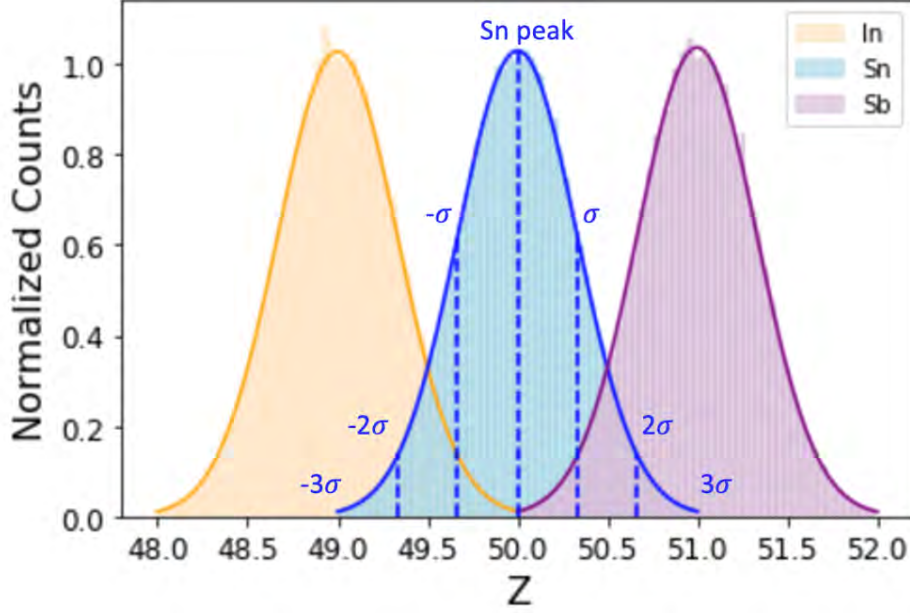


Figure 2.6: Illustration of 3σ separation in a histogram of equally represented Z . The left peak corresponds to In, middle to Sn, and right to Sb. 68% of Sn is within $-\sigma$ to σ , 95% in $\pm 2\sigma$ and 99.7% in $\pm 3\sigma$.

Isotopes are analyzed on an event-by-event basis, with each DAQ-registered event containing key parameters such as the trajectory from the CRDCs, energy loss from the IC, timestamp from the plastic scintillator, and total kinetic energy from the hodoscope. These measurements can be synchronized with detectors at the reaction target, enabling a detailed correlation between the nuclear physics observed at the target and the reaction products identified in the focal plane.

Data analysis often involves applying data acquisition gates to isolate events under specific conditions. For instance, studying the nuclear physics associated with the production of tin (Sn) isotopes, a gate can be placed around the peak at $Z = 50$ in the histogram of atomic numbers (i.e. Figure 2.6. This approach restricts the analysis to events within the gated range, such that only the gamma spectrum (or momentum, angular distribution, etc.) of these filtered events is observed. For data separated by 3σ from Z to $Z + 1$, a gate around

$Z = 50$ from $Z = 49.33$ to $Z = 50.66$ ($Z - 2\sigma$ to $Z + 2\sigma$) would contain only 75% of the total Sn isotopes, assuming In, Sn, and Sb were equally represented. In contrast, a 1σ gate centered at $Z = 50$ would correctly correlate 94.6% of target and focal plane events while utilizing 68% of the total Sn counts.

Table 2.1 illustrates various gate size scenarios and their impact on the composition of filtered data. Figure 2.6 and Table 2.1 help relay that the separation between successive peaks ($Z = 49, 50, 51$ for instance) must be at least 3σ or higher. Any less significantly limits the usable data while increasing the presence of unwanted isotopes.

Table 2.1: Concentration of Sn for different gate sizes with 3σ separation

Number of σ between successive peaks	Percentage of the total Sn inside the gated region	Percent of gated data that is In	Percent of gated data that is Sn	Percent of gated data that is Sb
σ	68%	3.2%	94.6%	3.2%
2σ	95%	12.5%	75%	12.5%
3σ	99.7%	25%	50%	25%

As higher Z beams get delivered on target, the Z -resolution needs to improve in conjunction to maintain 3σ separation. The Z -resolution is denoted as $\frac{\delta Z}{Z}(\%)$, where δZ is the standard deviation of the Gaussian-like peak at Z given as a percent. A low $\frac{\delta Z}{Z}(\%)$ means a more accurate measurement, analogous to better resolution. Occasionally, the Z -resolution is said to increase, if it is not explicitly referred to in the form: $\frac{\delta Z}{Z}(\%)$, then it can be assumed that the resolution is improving, thus $\frac{\delta Z}{Z}(\%)$ is actually decreasing. Figure 2.7 shows the Z -resolution required to achieve 3σ of separation between Z and $Z \pm 1$.

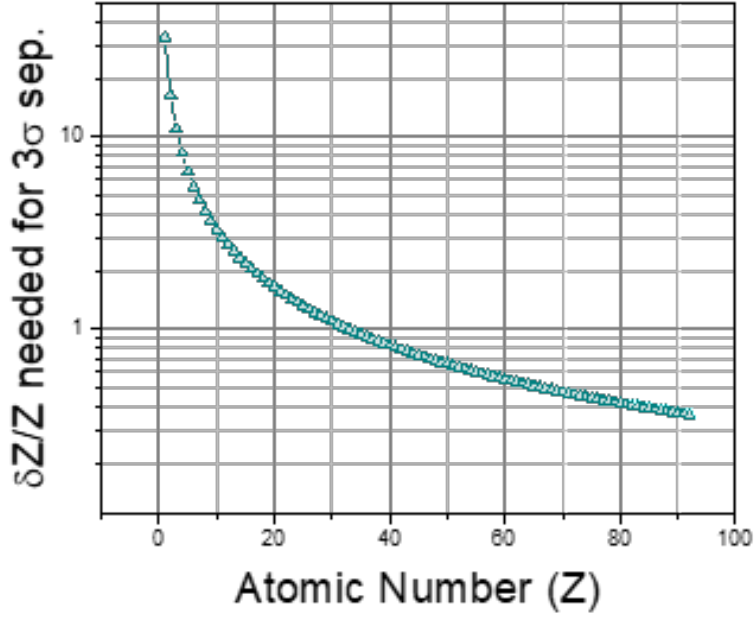


Figure 2.7: The $\frac{\delta Z}{Z}$ needed to achieve 3σ separation for different Z with respect to $Z\pm 1$.

From Figure 2.7, the $\frac{\delta Z}{Z}$ needed to separate Uranium (U) from Protactinium (Pa) and Neptunium (Np) by 3σ is 0.36%. Likewise, for the example used earlier $Z = 50$, the Z -resolution has to be better than 0.66% for 3σ separation. Section 2.2.3 explained that Z can't be measured directly, instead it is computed from the combination of ΔE and ToF . Thus, the resolution of Z directly depends on the energy resolution of the ionization chamber and timing resolution of the plastic scintillator. The relationship, derived from Equation 2.7, is presented below.

$$\frac{\delta Z}{Z} = \left(\left(\frac{1}{2} \frac{\delta(\Delta E)}{\Delta E} \right)^2 + \left(\frac{\delta ToF}{ToF} \right)^2 \right)^{1/2} \quad (2.11)$$

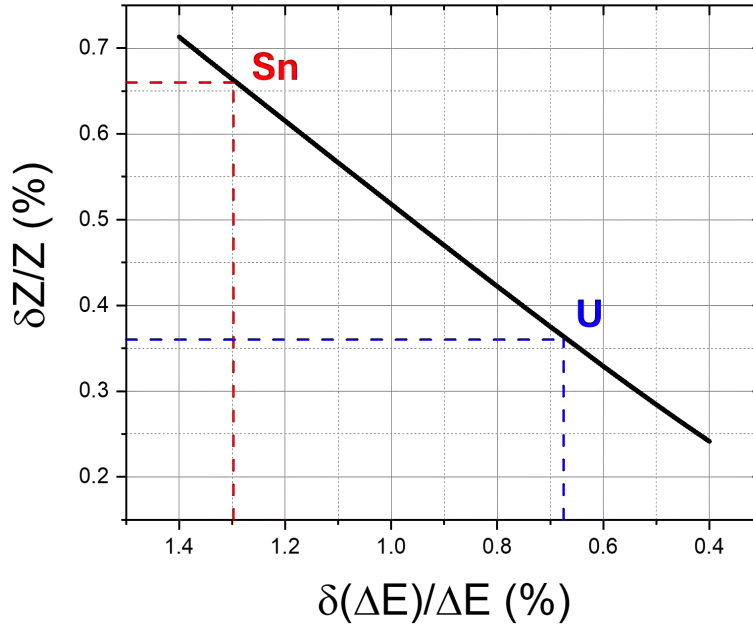


Figure 2.8: $\frac{\delta Z}{Z}$ as a function of $\frac{\delta \Delta E}{\Delta E}$ is plotted in the solid line and the goal $\frac{\delta Z}{Z}$ is plotted with a dashed line. With zero change in ToF resolution, the energy loss resolution would need to lower to 0.6% to get $\frac{\delta Z}{Z}$ low enough to separate Z in the uranium region.

Figure 2.8 shows the Z -resolution as a function of the energy loss resolution assuming no change in the ToF measurement. The ToF was set to 148 ns and the timing resolution was set to 200 μ s. Given these conditions, Figure 2.8 indicates that the Z -resolution needed for Sn can be achieved with energy resolution less than 1.3% and less than 0.68% for U. Consequently, the design goal for a new ΔE detector has been defined: achieve $\frac{\delta(\Delta E)}{\Delta E} < 0.68\%$ in order to separate U from Pa and Np by at least 3σ .

2.5 ELOSS: A New Type of Energy-Loss Detector

2.5.1 Advantages of High-Z Gas

The multi-segmented, ionization chamber in a stacked parallel plate configuration has been the standard for heavy-ion atomic number identification for many years [14] [15] [16] [17], but as the science needs become more demanding and the particle accelerator beams become more powerful, the need for a new state-of-the-art detector becomes ever more necessary. A simple, but effective idea has recently been tested at FRIB. The idea uses the same ionization chamber geometry employed over the last two plus decades, but changes out the P10 gas for pure Krypton. Preliminary results from a low- Z region cocktail beam suggest an energy loss resolution of about 0.8% σ for Krypton compared to the 1.2% σ with P10.

$$\Omega_{\Delta E}^2 = \Omega_{Bohr}^2 + \Omega_{cex}^2 + \Omega_N^2 + \Omega_{det}^2 \quad (2.12)$$

The improved energy resolution can be explained by investigating how the different contributions of $\Omega_{\Delta E}^2$ (Equation 2.12) change as a function of \tilde{Z} since the detector dimensions and pressure stay the same (only difference is \tilde{Z}). Ω_{Bohr}^2 denotes the Bohr straggling, Ω_{cex}^2 represents the straggling caused by charge exchange collisions, and Ω_{det}^2 accounts for the resolution of the detector and its components, also considered the noise level.

The average increase in energy loss fluctuation from collisional straggling is defined by Lindhard and Sorensen [18] as

$$\frac{d\Omega_{col}^2}{dx} = 4\pi Z^2 e^4 N \tilde{Z} \quad (2.13)$$

The integral of Equation 2.13 over the thickness of the detector results in the Bohr straggling expression [19].

$$\Omega_{Bohr}^2 = 4\pi Z^2 e^4 N \tilde{Z} \Delta x \quad (2.14)$$

Bohr's expression for collisional energy straggling only includes the fluctuations in energy loss due to stochastic close-range collisions, primarily at high projectile energy. Directly comparing the Bohr straggling between the IC with different gases simplifies down to the relationship in Equation 2.15

$$\Omega_{Bohr}^2 \sim \tilde{Z} \quad (2.15)$$

Thus, the relative Bohr straggling $\frac{\Omega_{Bohr}}{\Delta E}$ (%) is proportional to $1/\sqrt{\tilde{Z}}$, since ΔE is proportional to \tilde{Z} , indicating a higher \tilde{Z} will improve the overall energy loss resolution from less collisional straggling.

At a lower energy regime where charge exchange is more likely, charge exchange straggling has to be considered as well.

$$\Omega_{cex}^2 = \Delta x \frac{F_0 F_1}{N (\sigma_{01} + \sigma_{10})} (S_0 - S_1)^2 \quad (2.16)$$

Collisional straggling with charge exchange between two charge states can be expressed as Equation 2.16 [20]. Here, Δx is the detector thickness, F_0 and F_1 are the equilibrium charge state fractions, N is the number of target atoms (gas density), S_0 and S_1 are the partial stopping powers, and σ_{01} and σ_{10} are the charge exchange cross sections.

Weick states that the sum of the charge exchange cross sections can be expressed as

$$\sum_j \sigma_{ij} = \frac{1}{N\lambda_i} \quad (2.17)$$

and since the mean free path λ is inversely proportional to \tilde{Z} , it can be concluded that $N(\sigma_{01} + \sigma_{10}) \sim \tilde{Z}$.

For the case of two charge states, F_0 can be expressed as x and F_1 as $1 - x$ where the maximum F_0F_1 is achieved when $x = 0.5$. Likewise, the maximum product of equilibrium charge state fractions decreases with a higher number of possible charge states ($\sim (\frac{1}{N})^N$). It can also be shown that the charge exchange straggling decreases as the number of charge exchanges N_c increases. Recently, a team at the Rare Isotope Beam Factory (RIBF) carried out a study using the simulation code GLOBAL that explored the relationship between heavy-ion beams, the filling gas of an ionization chamber and the number of charge exchange collisions in the detector. In their paper titled, “Xenon-gas ionization chamber to improve particle identification of heavy ion beams with $Z > 70$ ”, they show that the energy resolution from charge exchange straggling depends on the average number of charge exchange collisions [15].

RIBF can produce ^{238}U beams in the energy region of 200-300 MeV/u. Their multisampling ionization chamber (MUSIC) has been successful at identifying isotopes with $Z < 50$ in this energy regime. Energy resolutions ranged from 1.9-3.0% (FWHM) for ^{238}U beams at energies between 165 and 344 MeV/u. The 0.8 – 1.3% σ resolutions proved to be inadequate for Z around Uranium. As a result, they proposed and tested a Xe-based IC that would increase the number of charge exchange collisions and lower the energy loss straggling.

A GLOBAL simulation with a P10-filled MUSIC, using ^{100}Zr ions, averaged 0 charge state changes for a gas length of 40 cm and 760 Torr pressure, but with ^{205}Pb ions, the average

number of charge state changes was about 2. The authors show the energy resolution from charge exchange straggling is at its worse when $N_c = 2$. Meanwhile, for the Xe-based MUSIC at 280 Torr (pressure difference is to normalize the energy lost in each case), the number of charge exchange collisions N_{cc} was simulated to be 23 for the same 40 cm gas length. At this N_{cc} , the Ω_{cex} (R_{cc} in RIBF paper) is sufficient for 3σ Z -separation.

After showing a significant improvement in energy straggling, correlated to N_c , they tested their Xe-filled MUSIC with the same ^{238}U beams (165 and 344 MeV/u) and measured an energy resolution of 1.4-1.6% FWHM ($\sim 0.59 - 0.68\% \sigma$). Thus, concluded that gases of higher \tilde{Z} initiate more charge exchange collisions on average leading to better energy resolution. Ultimately, 3σ Z -separation was achieved for $Z = 40 - 90$ using the Xe-filled IC.

Going back to Equation 2.16, $(S_0 - S_1)^2$ is the difference in partial stopping powers. For the same detector, but different gases, $S_i \sim \tilde{Z} Z_i^2$. For two charge states, this looks like

$$(S_0 - S_1)^2 \sim \tilde{Z}^2 (Z_0^2 - Z_1^2) \quad (2.18)$$

If $Z_0 = Z$ and $Z_1 = Z - 1$,

$$\tilde{Z}^2 (Z_0^2 - Z_1^2) = \tilde{Z}^2 (2Z^2 - 1) \sim \tilde{Z}^2 Z^2 \quad (2.19)$$

All together comparing the charge exchange collisional straggling between gases of different \tilde{Z} ,

$$\Omega_{cex}^2 \sim \tilde{Z} \quad (2.20)$$

As a result, the full collisional straggling $\Omega_{col}^2 = \Omega_{Bohr}^2 + \Omega_{cex}^2$ is proportional to the atomic

number \tilde{Z} of the detector gas. Furthermore, with higher \tilde{Z} the energy loss in the different gases increases resulting in more electron-ion pairs. Increasing the number of electrons/ions aka. information carriers for each detected beam particle increases the confidence in the charge information collected at the IC readout (foils). Confidence in the information collected is analogous to the resolution of the energy loss measurement. The number of electron-ion pairs follows a Poisson distribution, thus, $\Omega_N^2 \sim N$ where N is the number of electron-ion pairs. Since the amount of ionized charge is directly proportional to the energy loss, the relationship $\Omega_N^2 \sim \tilde{Z}$ can be deduced. Rewriting Equation 2.12 in terms of \tilde{Z} gives

$$\Omega_{\Delta E}^2 \sim \tilde{Z} + \tilde{Z} + \tilde{Z} + \Omega_{det}^2 \quad (2.21)$$

Finally, the relative total energy resolution is determined to be Equation 2.22, where $\Delta E \sim \tilde{Z}$.

$$\frac{\Omega_{\Delta E}}{\Delta E} (\%) \sim \frac{\sqrt{3\tilde{Z} + \Omega_{det}^2}}{\Delta E} \rightarrow \frac{1}{\sqrt{\tilde{Z}}} \quad (2.22)$$

The $\frac{1}{\sqrt{\tilde{Z}}}$ dependence implies the energy loss resolution improves as the detector gas is replaced with a higher- \tilde{Z} option. Thus, the improvement in $\frac{\Omega_{\Delta E}}{\Delta E}$ (also written as $\frac{\delta(\Delta E)}{\Delta E}$ in Section 2.4) when switching the ionization chamber gas from P10 to Krypton (S800) or Xenon (RIBF) is justified, suggesting a next generation energy loss detector should use Xenon for the best energy resolution.

2.5.2 Xenon as a High Z, High-Luminescence Gas

Xenon has been identified as an ideal gas for a new ΔE -detector due to its high \tilde{Z} . A high- \tilde{Z} gas significantly enhances energy loss resolution due to the inverse relationship be-

tween $\frac{\delta(\Delta E)}{\Delta E}$ and \tilde{Z} . This improvement is critical for accurately identifying nuclear reaction products that require exceptional energy resolution for 3σ separation in Z , but the benefits of Xenon don't end there.

2.5.2.1 Collection of Prompt Scintillation

By the 1980s, noble gases such as Argon (Ar), Krypton (Kr), and Xenon (Xe) had become widely recognized as effective solutions for gas scintillation detectors in heavy-ion experiments [21]. This was due to their high luminescence yield (often shifting the far UV light to visible with wavelength shifters), fast decay times enabling excellent time resolution, and an approximately linear relationship between light output and energy deposition. Among the noble gases, Xenon stands out with the highest scintillation yield, leading to higher energy resolution than other rare gases due to $\Omega_N \sim \frac{1}{\sqrt{N}}$.

Scintillation, needing less energy than what is needed to create an electron-ion pair, generates more information carriers (photons) compared to ionization and thus the argument can be made that $\frac{\Omega_N}{\Delta E}$ (%) decreases by collecting Xenon's scintillation rather than its ionized charge. However, this is generally only true if all of the light produced is collected, which is nearly impossible in large-area gaseous scintillation detectors. The real advantage of a scintillation detector over the conventional ionization chamber is the readout mechanism. Light is collected in extremely sensitive photosensors, typically capable of measuring down to single photoelectron sensitivity because of its built-in amplification stage [22]. Photomultiplier tubes, for instance, can achieve an electron gain from 10^4 to 10^6 [23], well above the noise floor introduced by the signal collection and processing electronics. For the ionization chamber, the noise threshold is equivalent to about 500 to 1000 electrons [?], meaning a charge induced on the electrode foils must exceed this level to be measured. Being able to measure

a signal is generally not a problem with fast heavy ions, but achieving a high signal-to-noise ratio (SNR) is important in terms of energy resolution. Ω_{det}^2 (Equation 2.12 can be thought of as the noise level in the detector, subsequently $\frac{\Omega_{det}}{\Delta E}(\%)$ is lower for PMT-based detectors rather than detectors, such as the IC, with large capacitive foils. This term is equivalent to the inverse SNR, indicating that for higher energy loss the SNR will increase and improve energy resolution.

2.5.2.2 Xenon Excimers and a VUV Wavelength

The primary mechanism for de-excitation of Xe is through the formation of excited dimers (excimers) that dissociate with vacuum ultra-violet (VUV) photon emission [21]. Heavy charged particles excite and ionize the Xe gas along a particle's trajectory to create Xe^* and Xe^+ . In low pressure environments, Xe^* has sufficient time to decay back down to its ground state and emit a UV photon, but at higher pressures Xe^* will collide with a ground state Xe and form either Xe_2^* (excimers) or Xe_2^{**} (doubly excited dimers) [9]. Primarily, three-body collisions are responsible for producing Xe_2^{**} , which becomes the more dominant interaction as gas pressure is raised.



Xe_2^{**} has two transition paths it can take [24] [21].



Equation 2.24 shows Xe_2^{**} dissociate into two ground state Xe atoms with the emission of a high energy photon that makes up the sharply peaked “first continuum” at 147 nm [21]. It is more likely, however, that the process described in Equation 2.25 occurs. At higher pressure ($P \geq 400$ Torr), the doubly excited excimer cools faster resulting in the vibrationally relaxed molecular state Xe_2^* . From here, the excited electron in Xe_2^* can transition from either the triplet or singlet excited state down to its ground state. The de-excitation releases a VUV photon in the “second continuum”, which is the most common form of scintillation emission from the excited Xe detector medium. The second continuum is peaked at 175 nm and is 10 nm in FWHM [25]. The excitation and de-excitation processes in Xe are illustrated in Figure 2.9

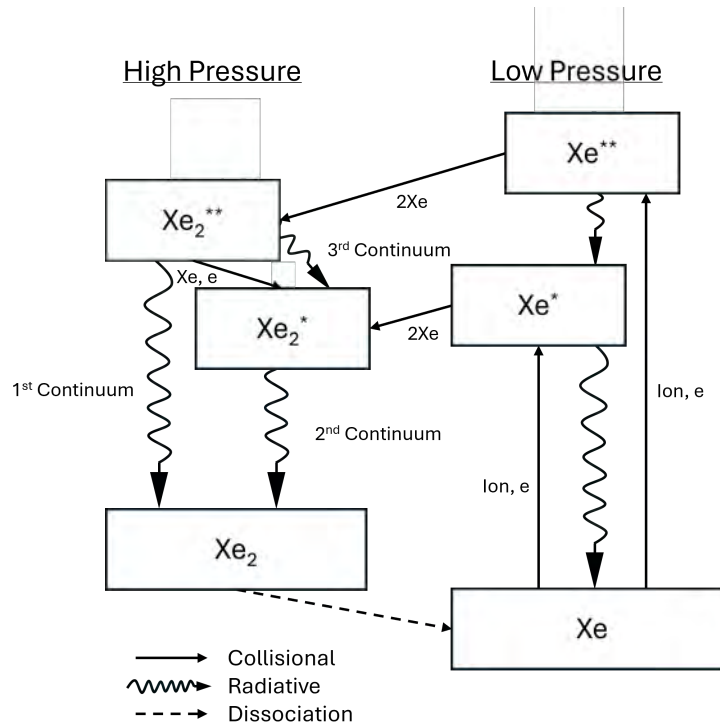


Figure 2.9: Excitation and de-excitation processes for high and low pressure systems of Xe gas.

The triplet to ground and singlet to ground transitions emit the same energy photon, but the decay times are quite different. Reported decay times vary, depending on pressure,

particle type, and measurement techniques [26] but generally follow: $\tau_s=6$ ns and $\tau_t=99$ ns [27]. Excitation by X-rays, electrons, and ions each favor different populations of excited states. Heavy ions, for instance, predominately fill the singlet excited state and therefore the emission spectrum is closer to a τ_s decay constant [28].

Heavy ions lose energy throughout the scintillating gas medium, which excites the gas atoms at different times according to the position of the heavy ion. Therefore, giving a short rise time to the photon emission spectrum. For GXe, approximately 90% of the scintillation is produced within 200 ns of the heavy ion traversing the detector. PMT signals from GXe scintillation become a convolution of all individual photons to make a continuous pulse with a fast rise time and short exponential decay. The result is a detector signal with a much larger amplitude and smaller pulse width than an ionization chamber could produce with a drifted charge readout.

Ultimately, charge-based readouts have a typical noise level equivalent to about 100-1000 electrons, they are slow (about $10.6 \mu\text{s}$ rise time for Xenon in the S800 IC [29]) and have a low SNR. Optical readouts are faster, while providing a larger SNR due to their independence from the detector medium, built-in signal amplification (photomultiplier tubes) and lower limit of detection (down to single photoelectrons).

2.5.2.3 Primary and Secondary Scintillation Yields

Experimental data shows that Xenon has a scintillation yield higher than any of the other common scintillator gases with Argon (14.7 ph/keV [30]) and Krypton (8.8 ph/keV [31]) being the closest. Scintillation yields have been measured in a variety of experimental setups that change the electric field, particle type used for excitation, gas pressure, temperature and detected emission wavelengths, producing a range of values. Table 2.2 summarizes

scintillation yields found for Xenon along with the the particle type that caused the excitation of the gas, the energy of that particle, the pressure and electric field if reported.

Table 2.2: Summary of scintillation yields for Xenon

SY (ph/keV)	Radiation	Energy (keV)	Pressure (atm)	E-Field (V cm ⁻¹)	Ref.
23.9	x-rays/ γ	5.9-60	1.18	70-300	[32]
27.3	alphas	2500	1.18	70-300	[32]
17.9	alphas	5500	0.372-0.43	-	[30]
12.5	x-rays	5.9	1.05	<418	[33]
16.9	alphas	5500	1.0	66.7	[34]
20.1	alphas	5500	1.0	0	[34]

In previous section, the scintillation process of Xe was discussed, but it was not the complete picture because Xe^+ atoms were ignored. Xe^+ can collide with a ground state Xe to form the dimer Xe_2^+ .



Recombination of a free electron and ionized dimer produces an excited Xe when there is no electric field present. In the presence of an electric field, electrons are accelerated, depending on the electric field strength, and can act as projectiles. They collide with ground state Xe to excite Xe^* that dissociate as described earlier. This is called stimulated electroluminescence and is how ELOSS will achieve even better energy resolution than originally perceived. According to [35], the reduced electroluminescence yield is a linear function dependent on the reduced electric field as Equation 2.27.

$$\frac{Y}{p}(\text{photons electron}^{-1} \text{ cm}^{-1} \text{ bar}^{-1}) = 140 \frac{E}{p} - 116 \quad (2.27)$$

The reduced electric field is normalized by pressure so its units are $\text{kV cm}^{-1} \text{ bar}^{-1}$. This relationship has its limits, however, below $1.3 \text{ kV cm}^{-1} \text{ bar}^{-1}$ the electroluminescence yield is 0. At the other end, above $8 \text{ kV cm}^{-1} \text{ bar}^{-1}$ the linear behavior changes to exponential as the ionization threshold has been reached and an avalanche process starts.

2.5.3 Energy Loss Optical Scintillation System (ELOSS)

In this chapter, the $B\rho - \Delta E - \text{ToF}$ PID method was defined, singling out the ΔE measurement used in atomic number identification. It was determined that $\frac{\delta(\Delta E)}{\Delta E}(\%)$ must be less than $1.30\% \sigma$ to achieve 3σ separation around $Z = 50$ and $0.68\% \sigma$ around $Z = 92$. The ionization chamber currently stationed in the S800 focal plane reaches a maximum energy resolution about $1.2\% \sigma$ with a multisampling Frish grid-less parallel plate configuration and P10 gas. It has been demonstrated that a simple change, such as using a higher Z gas like Xenon, can improve energy resolution to near $0.6\% \sigma$.

The next generation ΔE -detector, called the Energy Loss Optical Scintillation System (ELOSS), will take all of the concepts discussed in this chapter to improve energy resolution to less than $0.6\% \sigma$ and identify short-lived nuclei in the S800 at a rate over 80 kHz. It will do so by filling a large gas vessel — effective area equal to the rest of the focal plane detectors ($60 \times 30 \text{ cm}^2$) — with 300-900 Torr of pure Xenon gas. Inside the vessel, arrays of photosensors will line the detector volume's walls facing the beam path. This optical readout arrangement is designed to collect the prompt (primary) scintillation that gets generated along particle tracks. As the particles traverse the Xenon volume inside ELOSS, they lose energy to the excitation and ionization of the Xenon gas. The massive amount of light produced from heavy ions interacting with the Xenon is proportional to the energy lost by the heavy ions inside the effective volume. By summing the photosensor signals, an ΔE

measurement can be obtained and used for identifying the Z of incident ions.

Chapter 3. Simulation-based Design Studies

3.1 Geant4

The optimization of the detector geometry and optical readout was carried out through a series of systematic simulations using the Geant4 software. Geant4 is an object-oriented simulation toolkit primarily used in high energy physics, space/radiation science and medical physics to simulate the passage of particles through matter [36]. Geant4 facilitates the development of a radiation detector model and the simulation of its primary operational processes. To create accurate and comprehensive simulations of detector interactions with primary and secondary particles, an extensive list of software components is readily available (e.g. C++ toolkit classes).

3.2 Detector Optimization

The initial ELOSS conception, built within Geant4, consists of an inside volume filled with gaseous Xe. The entrance and exit openings are covered by 14 mg/cm^2 Kevlar windows, chosen for its superior strength (can withstand a pressure difference of 1.3 atm over a $60 \times 30 \text{ cm}^2$ area) and low material budget. Scintillation light collected by the arrays of photosensors originates in what is defined as the effective volume. This is distinct from the whole Xenon volume that completely fills the detector because only energy deposited/light produced in the effective volume is recorded. The photosensors making up the optical readout face towards the effective Xe volume. Outside of the optical readout is the gas containment vessel made of stainless steel. The vessel is not considered within Geant4 because particle interactions

with this volume are minimal and irrelevant to the detector’s performance.

The Xe pressure was set to 1 atm to ensure an accurate ΔE comparison between the IC and ELOSS, despite the IC being thicker. The scintillation properties of Xe for the Geant4 ELOSS are summarized in Table 3.1.

Table 3.1: Scintillation properties of GXe set in the ELOSS Geant4 application [37] [38]

Property	Entry 1	Entry 2	Entry 3
Photon Energy	6.91 eV	6.98 eV	7.05 eV
Fraction of Emission Spectrum	0.1	1.0	0.1
Refractive Index	1.0	1.0	1.0
Absorption Length	100 m	100 m	100 m
Scattering Length	100 m	100 m	100 m

Three photon energies were selected to represent the second continuum of Xe with the peak at 177.6 nm (6.98 eV). A refractive index, absorption length and scattering length in Xe were initialized for each photon energy. They were set to make Xe a transparent volume at the specified scintillation wavelengths. Two scintillation decay components were added to the Xe material properties corresponding to the fast (singlet) and slow (triplet) transitions. The singlet decay constant was set to 4.1 ns and the triplet decay constant was set to 21 ns. Lastly, the scintillation yield was set to 13 photons/keV, which is a conservative value taken from [33] [38].

3.2.1 Photosensors

Three different photosensor technologies were considered for the construction of the ELOSS optical readout, including (a) 120 Hamamatsu R8520-406 PMTs, (b) 30 Hamamatsu R12699-

406 PMTs and (c) 6 large-area MCP-PMTs. A detector configuration for each photosensor type is schematically illustrated in Figure 3.1. In each configuration, the arrangement of the photosensors was cost-effective and optimized for maximum photon collection efficiency (PCE). PCE is the fraction of photons collected by the photosensitive surfaces of the detector over the total number of generated photons given as a percentage. It was calculated by counting the number of photons that cross from the effective Xe volume to a photosensor volume and the total number of photons generated in the effective Xe volume.

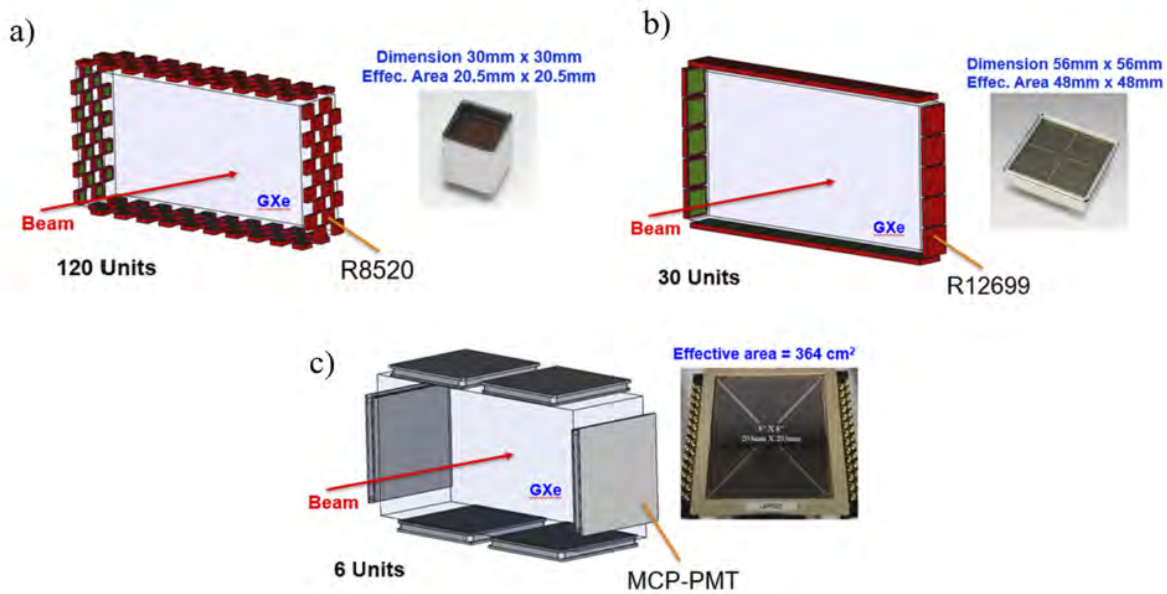


Figure 3.1: Optical readout configurations

A chessboard-like pattern was instated for the smaller ($30 \times 30 \text{ mm}^2$ area) R8520 PMTs and split into four equally spaced sectors. The R12699 PMTs have a $50.8 \times 50.8 \text{ mm}^2$ multianode photosensitive area that were arranged into a single equivalent sector. The photocathode coverage is about 75% for the R12699 PMTs compared to 58% for the R8520s. Both PMTs have a similar spectral response and photon detection efficiency. The results, however, favor the R8520 PMTs since the energy straggling is below the required energy

resolution ($0.6\% \sigma$). For 4 layers of R8520 PMTs (each 30 mm thick), totaling 120 mm of Xe at 1atm, the relative energy straggling was $0.55\% \sigma$ compared to $0.77\% \sigma$ in the single layer R12699 configuration 56 mm thick. Energy straggling is inversely proportional to material thickness, thus a thicker detector improves energy resolution. However, keeping the same number of photosensor units, but increasing the detector thickness, meant sacrificing PCE and consequently the energy resolution for the R12699 configuration. Another factor to consider is the maximum rate capability, which depends on the number of photoelectrons detected per photosensor. For the larger area R12699, the maximum rate was around 10 kHz compared to 50 kHz with the R8520.

The third configuration based on the large-area MCP PMTs has significant areal coverage ($300 \times 300 \text{ mm}^2$) per MCP-PMT with only 6 units. They have a photon detection efficiency around 18% when coupled to a CsI-based photocathode, and boast a very good time resolution ($<20 \text{ ps}$, σ). The MCP-PMTs (also referred to as Large Area Picosecond PhotoDetectors - LAPPDs), provided the largest light collection efficiency (11.3%) in the open-volume configuration and the second highest collection efficiency in a short volume with reflector foils (38%) and a long volume with reflectors (38%). The resulting Z -resolution was the best in every one of the configurations, partially do to the five times greater energy deposition from the much thicker detector. A ΔZ of 0.29 in the open configuration is sufficient for 3σ separation, measured using a ^{108}Sn beam at 80 MeV/u. However, the huge amount of light being collected is only split between six photodetectors, which can saturate them leading to loss in linearity. With stable gain at 1 MHz/cm^2 , a detection rate of only 3.5 kHz is possible, which would be a downgrade from the current IC.

The four sector chessboard-like configuration with the R8520 PMTs was ultimately selected as the optimal optical readout based on its compromise between performance and

cost. Important to the performance is the energy resolution, counting rate and timing. Factored into the cost was the number of individual detectors needed and consequently the DAQ channels, interfaces and equipment.

3.2.2 Geometry

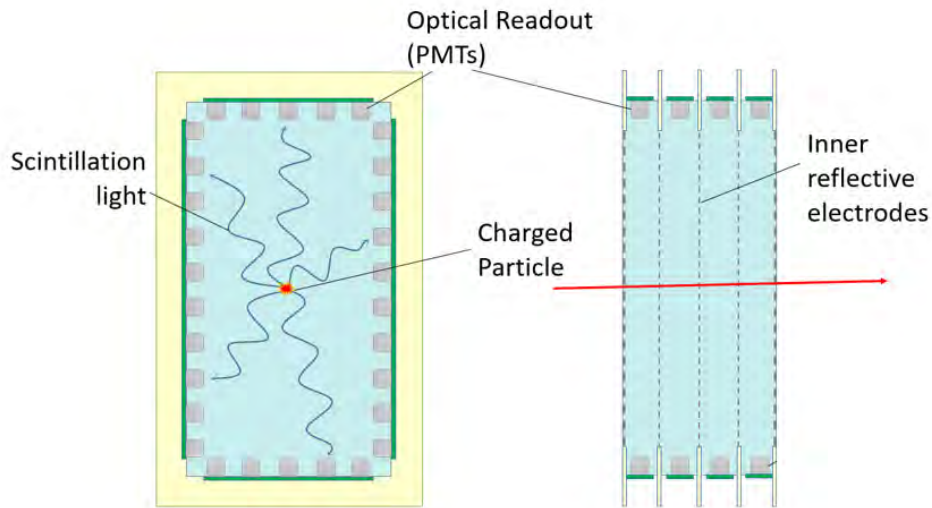


Figure 3.2: ELOSS concept schematic showing four sectors divided by reflective electrodes.

As discussed in Chapter 2, there are two possible modes of operation in ELOSS. The first is based on the collection of Xe’s prompt scintillation from the passage of a charged particle. The second method still collects scintillation, but instead of the primary scintillation, ELOSS will collect the secondary scintillation generated by the electroluminescence process when a suitable electric field is present inside the detector. In order to produce an electric field across the effective Xe volume, a potential difference needs to be established. This can be done similar to the ionization chamber with parallel aluminized polypropylene foils stacked in the direction of the beam such as in Figure 3.2.

A series of GEANT4 simulations were developed to study the affect of reflectors on

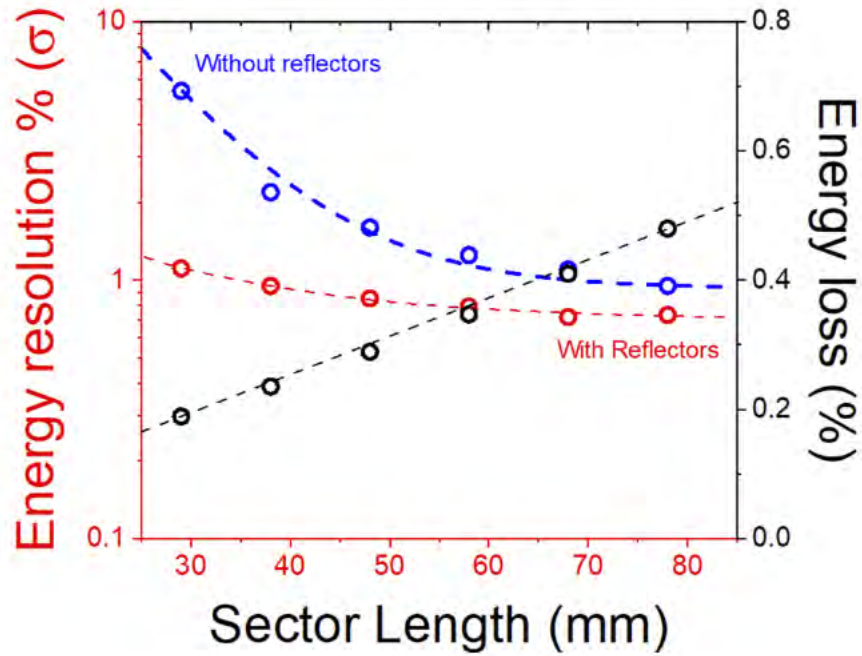


Figure 3.3: Optical readout configurations

the energy resolution. The Monte Carlo simulation study recorded the energy resolution as the sector thickness was increased for an ELOSS with and without reflectors between sectors. The results shown in Figure 3.3 demonstrate an improvement in energy resolution as the sector length is increased corresponding to the larger energy loss. However, it also demonstrates that the ELOSS configuration with reflectors achieves a much better energy resolution than the ELOSS without reflectors at a shorter sector length. A short distance between reflectors is desired because they also will act as the electrodes for setting up an electric field. The closer they are, the lower voltage is needed to generate the minimum 1.3 kV/cm/bar reduced field defined in Section 2.5.2.3. Too high of a foil bias may cause unstable operations, resulting in sporadic and harmful discharges between the components at high voltage and the ground (especially the forethought and bias cables) with a high probability of damaging different detector components. As a compromise between light collection efficiency (energy resolution) and the operation stability, a sector length of 47.5 mm was chosen.

3.3 Expected performance

In order to optimize the design of ELOSS and its components, a performance evaluation in terms of PID based on a Geant4 evaluation was carried out using the configuration shown in Figure 3.1 (a). The study included 5 separate simulations with five different isotopes. Each isotope was fully stripped and started with 100 MeV/u energy. The isotopes chosen, $^{108}\text{Cd}^{48+}$, $^{108}\text{In}^{49+}$, $^{108}\text{Sn}^{50+}$, $^{108}\text{Sb}^{51+}$, and $^{108}\text{Te}^{52+}$, all have the same mass and span a range of 5 Z . This is an important region to test because $Z=50$ is the current PID limit of the ionization chamber. By using the same mass, the ToF is pretty much the same making the impact of the energy resolution more visible. For this experiment, ELOSS was at 1 atm and did not contain reflectors. The PID is shown in Figure 3.4.

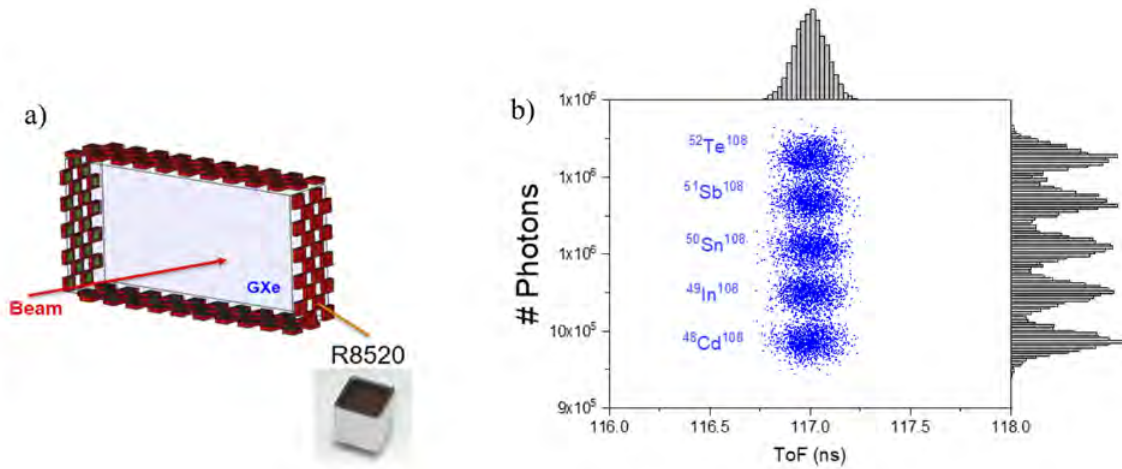


Figure 3.4: PID performance with the R8520 PMT configuration.

In this configuration, the light collection efficiency was estimated to be 16.3%. The system was able to reach an energy resolution of 1.2% σ corresponding to σ_Z of 0.62%. This is sufficient for 3σ separation in this Z region. Increasing the pressure to 1.3 atm and implementing position corrections to the energy loss, energy resolutions below 0.6% are

possible corresponding to $\sigma_Z < 0.4\%$. This is on the fringe of acceptable resolution for 3σ separation in the Uranium region of Z .

Chapter 4. ELOSS Design and Components

4.1 Optical Readout

Light is collected using arrays of Hamamatsu R8520-406 PMTs, arranged in four sectors along the periphery of the detector's $30 \times 60 \text{ cm}^2$ effective area. There are ten equally spaced PMTs in each sector along each side of the long vertical direction (dispersed beam coordinate) and five equally spaced PMTs along each side of the short horizontal direction (non-dispersed beam coordinate) adding up to a total of 120 PMTs.

4.1.1 Photomultiplier Tubes

The PMTs used in ELOSS (Hamamatsu model R8520-406 [39]) are specifically engineered for dark matter search experiments like XENON100 [40] that submerge them in liquid Xenon. Their synthetic silica windows transmit ultraviolet (UV) radiation down to 160 nm, a significant improvement over the more commonly used borosilicate windows, which have a 300 nm UV cut-off [23]. By combining a deep UV transparent window with a bi-alkali photocathode, a spectral range of 160 nm to 650 nm is achieved. A graphical representation of the quantum efficiency within this spectral range, as depicted in Figure 4.1, illustrates a peak quantum efficiency of 30% at 175 nm [39]. This wavelength is particularly noteworthy as it aligns with the second continuum in Xenon's scintillation spectrum.

The PMTs are positively biased at the anode and grounded at the photocathode. This biasing configuration enhances single photoelectron sensitivity by mitigating noise that could be introduced on the photocathode by the high voltage power supply. Additionally, it minimizes potential interference with the electric field between electrode foils during stimulated

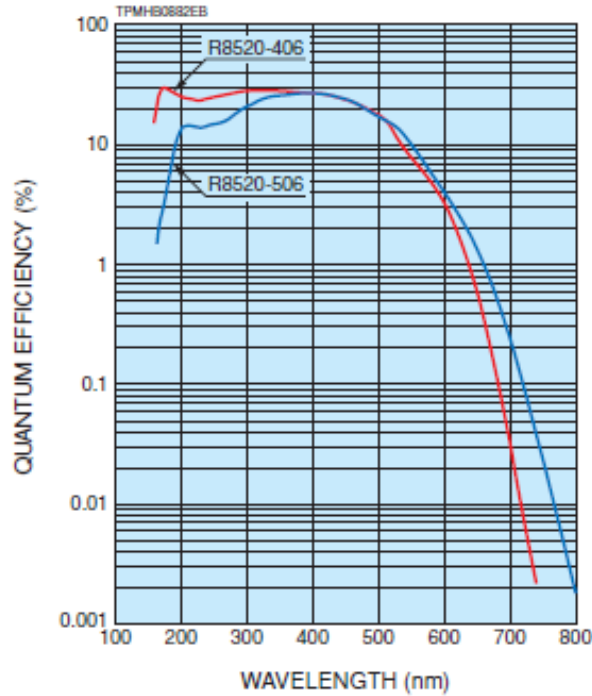


Figure 4.1: Spectral responses for R8520 PMTs. The peak quantum efficiency, indicated by the arrow from R8520-406, is 30% at 175 nm.

electroluminescence mode operation.

The positive anode bias is divided among ten dynodes and a grid-like focusing element positioned between the photocathode and first dynode. The potential differences established between successive dynodes facilitate the electron multiplication, while the focusing element is included for shaping the electric field, which aims to maximize photoelectron collection efficiency. Figure 4.2 displays the voltage distribution suggested by Hamamatsu. With this distribution, electron multiplication can reach a gain of 10^6 at the nominal 800 V supply voltage, while exhibiting a 1.8 ns anode pulse rise time and 0.8 ns (FWHM) transit time spread [39].

VOLTAGE DISTRIBUTION RATIO AND SUPPLY VOLTAGE

Electrodes	K	G	Dy1	Dy2	Dy3	Dy4	Dy5	Dy6	Dy7	Dy8	Dy9	Dy10	P
Ratio	0.5	1.5	2	1	1	1	1	1	1	1	1	1	0.5

Supply voltage: 800 V, K: Cathode, G: Grid, Dy: Dynode, P: Anode

Figure 4.2: Voltage distribution ratio from R8520 PMT datasheet.

In DC operation of PMTs, where a constant light source is used, the output current should generally only be 1/100th of the divider current to achieve linearity better than $\pm 1\%$ [23]. However, in pulse mode operation, such as in ELOSS, the peak output current can be thousands of times higher than the divider current by placing a series of decoupling capacitors connected in parallel to the last few dynode stages. This configuration provides the dynodes with a supply of charge that stabilizes the potential differences at the end of the multiplication stage and also at the anode collection. However, the average anode current should still be less than 25% of the divider current for optimal linearity. By raising the peak output current, PMT sensitivity improves. Additionally, ELOSS employs a voltage-divider with five times smaller total resistance than suggested by Hamamatsu in the R8520 datasheet. With a smaller resistance, higher divider current flows at the same supply voltage, corresponding directly to more sensitive PMTs and higher counting rates. Hamamatsu’s suggested voltage-divider is tailored to temperature-sensitive environments such as PMTs submerged in LXe, but ELOSS operates at atmospheric pressure, which is less susceptible to heat generated by currents in the resistive elements of the voltage-divider PCB bases. The improvement in sensitivity increases the optical readout dynamic range, which is critical for heavy-ion PID.

In the scintillation counting (“pulse”) mode of PMT operation, the PMT output is read-out through a drop down resistor that connects the anode to ground. The voltage measured across this resistor is proportional to the number of incident photons by the resistance value, PMT gain, photodetection efficiency, etc. For PMTs with a positive voltage applied to their anode, a decoupling capacitor is needed to extract the light response from the steady high voltage at the anode. The capacitor blocks the steady divider current and passes the sharp current pulse, so that the output is only a negative voltage pulse with a zero offset.

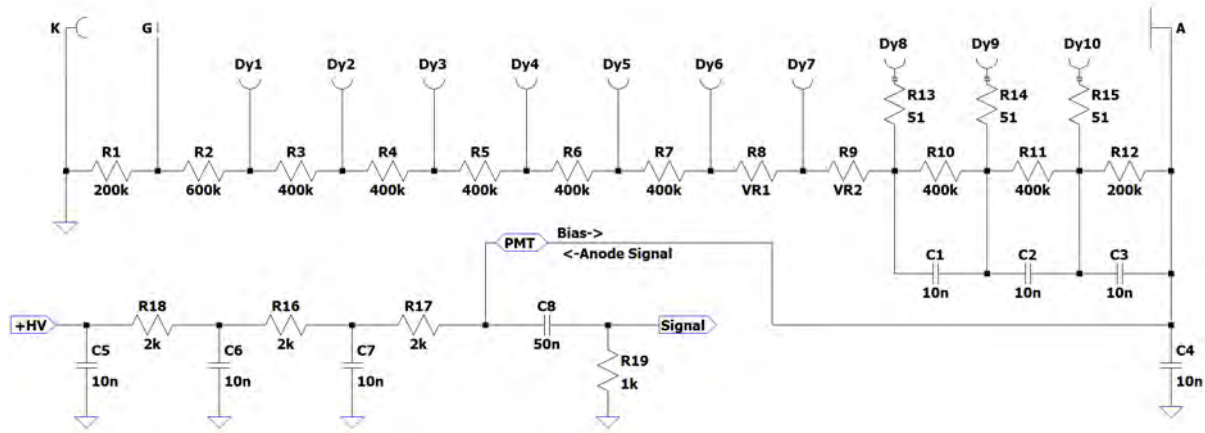


Figure 4.3: Voltage-divider and anode signal readout circuit.

The PMTs for each side of a sector are mounted on one printed circuit board (PCB). An example of a long PCB and close up view of the individual PMT voltage-divider are illustrated in Figure 4.4 using the Altium Designer view. An extra feature of the PMT array PCBs is the addition of LEDs placed between each PMT. These are intended for online monitoring of the optical readout without requiring Xenon and an ion beam.

The PMT array is positioned with an offset with respect to one end of the PCB. With this design, neighboring PMT arrays could be oriented 180 degrees to each other to create a staggering of the PMT arrays on each side creating the chessboard-like pattern discussed in Chapter 3. Figure 4.5 illustrates an updated version of Figure 3.2, but includes the PMT array staggering that creates the chessboard-like pattern.

4.1.2 Reflector foils

The polypropylene foils that separate the sectors of ELOSS are stretched to a uniform thickness of $0.75 \mu\text{m}$. These foils are temporarily glued to a metal frame to maintain their stretched state, allowing them to be metalized. In the FRIB Detector Lab's evaporation chamber, an electron beam vaporizes an aluminum sample, uniformly coating the foil with

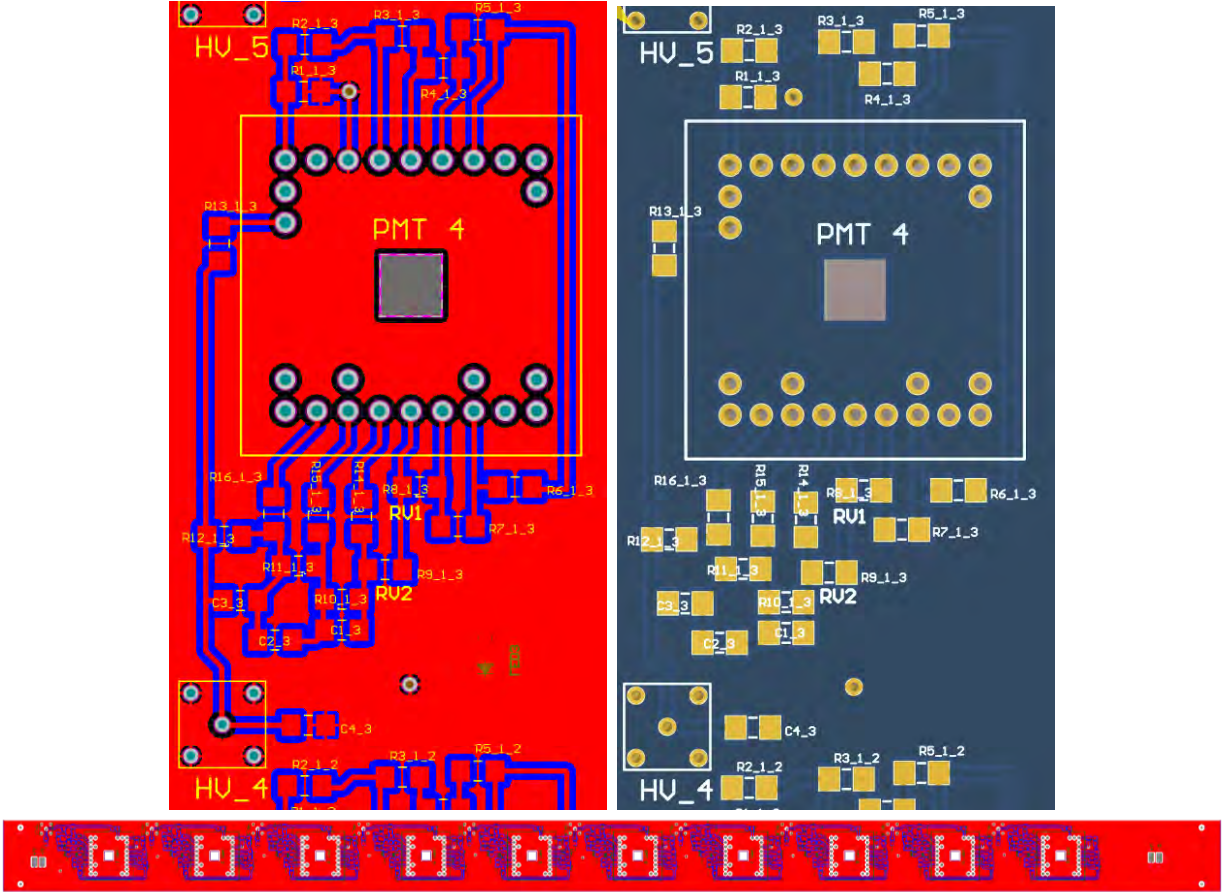


Figure 4.4: Top left: close up view of one PMT voltage-divider in Altium 2D viewer. Top right: close up view of one PMT voltage-divider in Altium 3D viewer. Bottom: entire vertical-side PCB in Altium 2D viewer.

150 nm of aluminum. The resulting aluminized polypropylene foils are then sandwiched between large PCB frames. The PCB frames not only hold each foil in place, but also make the electrical contact for delivering the bias to the foil electrodes. A metal coating on the foil side of the PCB frame creates the electrical contact and is traced to a metal tab on the outside edge of the frame. A HV-rated wire is soldered to the metal tab for supplying voltage to the PCB frame. The estimated reflectivity of these aluminized foils is greater than 80% [?], while metal coating of the PCB frame provides a more reflective surface, also estimated about 80%.

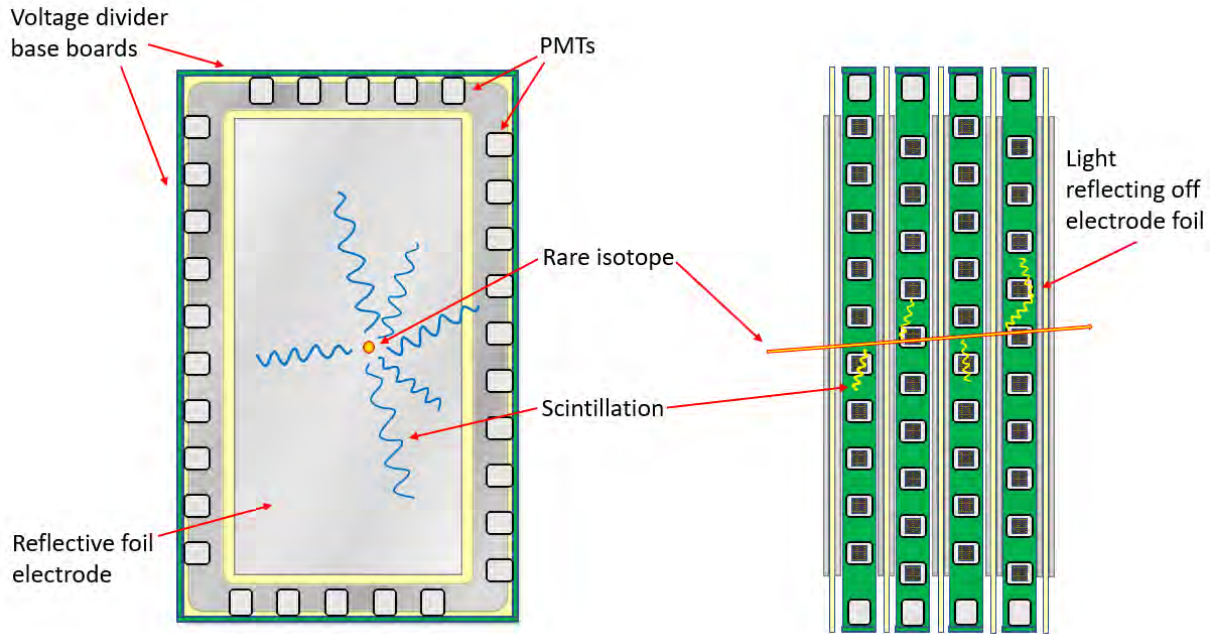


Figure 4.5: Updated 2D ELOSS concept schematic including the chessboard-like PMT placement pattern. The side profile is from the viewpoint of looking in from the right side of the detector if the right side was taken away.

4.2 Mechanical Structure

4.2.1 ELOSS vessel

The ELOSS vessel is a large rectangular stainless-steel chamber, with dimensions of $48 \times 80 \times 32.2$ cm³. The vessel features a 30×60 cm² opening at both the front and back, encircled by a pattern of tapped bolt holes, which are designated for the pressure windows. A comprehensive 3D model of the ELOSS vessel is illustrated in Figure 4.6. The left side of the vessel is open, featuring a slim, lipped edge with bolt holes intended for securing the lid. The lid and pressure window frames are equipped with thick O-rings, which form a seal, creating a vacuum-tight chamber.

The ELOSS detector, complete with pressure windows and lid, weighs just under 300

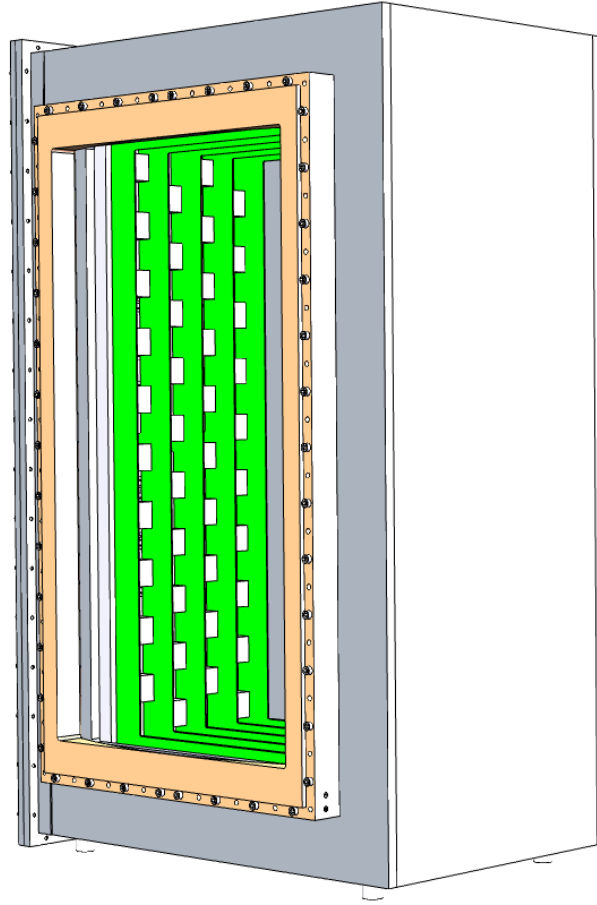


Figure 4.6: 3D CAD drawing of the ELOSS vessel with the optical readout support and PMTs installed inside. No pressure windows or reflector foils.

lbs. To ensure the safety of personnel and protect the PMTs inside the vessel, the detector is always lifted using a crane. Anchor points are welded at the four corners of the lid to provide lifting points for the crane. These anchor points also serve as legs, allowing the detector to rest on them during tabletop maintenance. Additionally, a fifth anchor point is welded on top of the detector vessel to provide a second lift point for flipping ELOSS upright, as illustrated in Figure 4.7.



Figure 4.7: Left side: ELOSS optical readout (attached to lid) being lowered into the detector vessel. The crane connects to the four anchor points on the lid. Right side: one crane attaches to the top anchor point and another holds the legs of ELOSS (legs are for installation on a moving table discussed later). Lifting the top rotates the detector smoothly.

4.2.2 Optical readout mechanical support

All 120 PMTs are contained in a single support structure secured to the inside surface of the ELOSS lid. With this configuration, the optical readout can be removed as one piece from the vessel, simplifying maintenance. The optical readout, comprised of the PMTs, voltage-divider PCBs, and reflector foils, are sandwiched between two thick aluminum frames anchored to the lid and spaced X cm apart. Figure 4.8 illustrates the separate components of the optical readout, and its support structure, as it is attached to the ELOSS lid. Threaded rods made of PEEK are used to align the aluminum frames, electrode foil PCBs, and PMT array PCBs. PEEK spacers enforce the 4.75 cm gap distance between foils and also act as support bases for the PMT array PCBs to screw to.

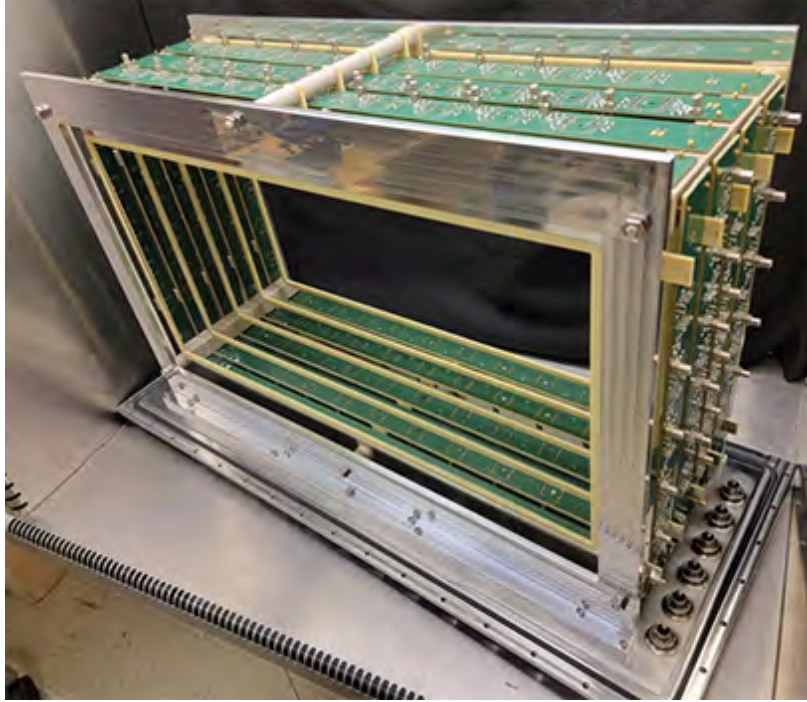


Figure 4.8: Optical readout support assembled without PMTs or reflector foils.

4.2.3 Pressure windows

The ELOSS pressure windows, one depicted in Figure 4.9, are fabricated and formed before being glued onto aluminum frames, which are subsequently fastened to the front and back of the ELOSS vessel. These windows are constructed from kevlar-reinforced dyneema in house laminated with epoxy (manufacture and model), with thicknesses varying between 14 mg/cm^2 to 24 mg/cm^2 , primarily influenced by the bonding glue's thickness between the kevlar and dyneema layers. Operating within a pressure range of 400 to 850 Torr, while the S800 focal plane maintains vacuum, the ELOSS pressure windows must endure a pressure differential of 1000 Torr, ensuring a safety factor of approximately 18%. Additionally, these windows must sustain this pressure without permitting Xenon leakage.

Extensive testing was conducted to develop a window fabrication procedure that meets these stringent requirements. The success of the pressure windows hinges significantly on the

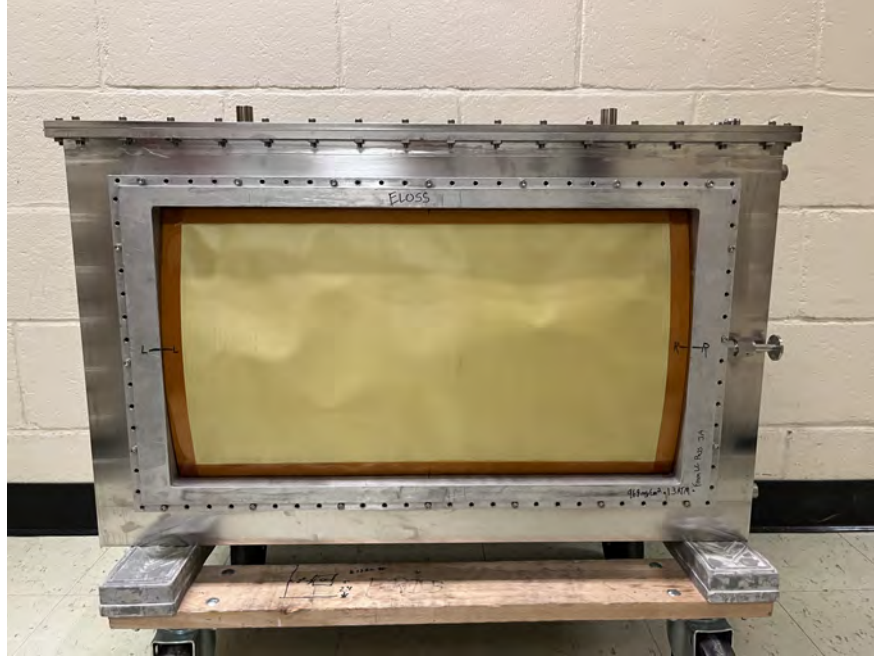


Figure 4.9: Front pressure window made of kevlar reinforced dyneema is installed on the ELOSS vessel.

precise application of glue throughout the fabrication process. It is imperative to begin with a smooth dyneema sheet on a perfectly flat surface, followed by an equally smooth Kevlar sheet atop the dyneema layer. 18.3 g of hardener (EZ 83B) and 41.7 g of epoxy resin (EZ 10A) are mixed well and evenly distributed across the window's effective area using a paint roller and squeegee, ensuring thorough penetration into the kevlar fibers and robust bonding with the dyneema. Optionally, kapton tape can be taped along the edge of the effective area on the kevlar to reinforce the boundary between the window and frame.

The window frames are designed to support a curved shape, optimizing pressure distribution. During fabrication, the window material is shaped on a heated element and simultaneously glued to the aluminum frame. Care is taken to apply the glue without allowing it to encroach upon the inner edge of the window frame. Excess glue squeezed out during frame pressing can cure along the frame edge, forming a sharp edge that may compromise the kevlar and dyneema integrity under pressure. Conversely, insufficient glue application

can lead to detachment of the kevlar/dyneema from the aluminum frame.

4.3 Gas Handling System

The ELOSS Gas Handling System (GHS) is designed to fill, regulate, and empty the detector volume. The main components of the GHS include a supply gas bottle with a pressure regulator for the injection of Xenon gas into the system, a purification system for the online removal of impurities, a control system for the regulation of gas flow and a Xenon gas recovery/storage system (XRS). A schematic of the GHS can be found in Figure 4.10.

The supply gas bottle provides the initial infusion of Xenon and small supplementary injections over time. At first, the XRS is isolated from the detector and the rest of the GHS. Consequently, only about 132 L of Xenon are required from the 400 L supply bottle. After recovering the Xenon and refilling the GHS using the recovered Xenon from the XRS storage, the detector should reach about 590 Torr (P_{refill}) when the entire system is opened and allowed to reach equilibrium, assuming an initial fill of 800 Torr and a vapor pressure of approximately 2 mTorr.

$$P_{refill} = 760 \text{ Torr} \cdot \frac{V_{ELOSS}(800 \text{ Torr}) - V_{ELOSS}(3 \text{ mTorr})}{V_{XRS} + V_{ELOSS}} \quad (4.1)$$

The volumes in Equation 4.1 are at standard temperature and pressure (STP) unless otherwise noted. V_{XRS} and V_{ELOSS} encompass the remaining GHS volume, which constitutes only a small fraction of the total, including components such as hoses and tubes. The P_{refill} measured in the first operation with Xenon was 608.8 Torr. This indicates that the total volume of the GHS might be smaller than initially modeled (~ 167 L at STP) or the starting pressure exceeded 800 Torr. Additionally, the uncertainty of the capacitance manometer

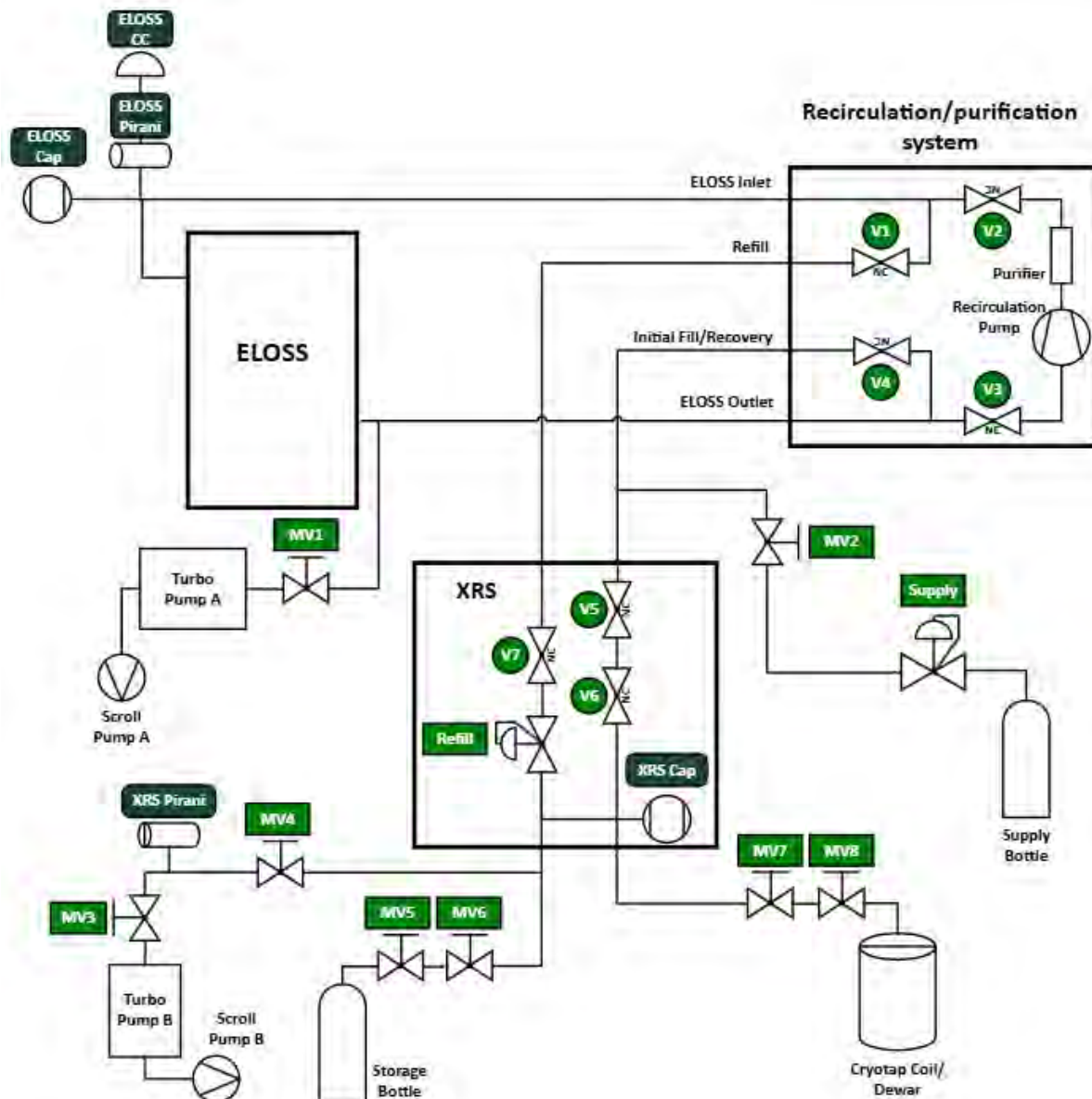


Figure 4.10: Schematic for the ELOSS Gas Handling System (GHS) used as a reference during operation. Labels each pressure gauge, valve, vacuum pumps and components in the same format as the procedure documents.

(MKS 722C,[41]), about 0.5% of reading, must be considered. Ultimately, a second injection from the supply bottle is required to refill ELOSS to 800 Torr. After this, the amount of Xenon in the entire GHS is sufficient to refill solely from the XRS storage.

The XRS uses liquid nitrogen (77 K) to cool a 1" OD copper coil (cryotrap), thereby establishing a low-pressure system within the cryotrap that allow to recover the Xenon gas by condensation/liquefaction. Below the liquid nitrogen (LN2) level, indicated in Figure 4.12, Xenon drawn into the bottom of the coil rapidly crystallizes upon transitioning from gas to solid, owing to the region being more than 80 K below Xenon's boiling and melting points—refer to Figure 4.11. At the LN2 level, Xenon boils off, transitioning into a gaseous state at the vapor pressure of solid Xenon around 77 K. To prevent crystal accumulation that could obstruct Xenon from filling the cryotrap coil completely, heat tape is wrapped around the small coil inlet.

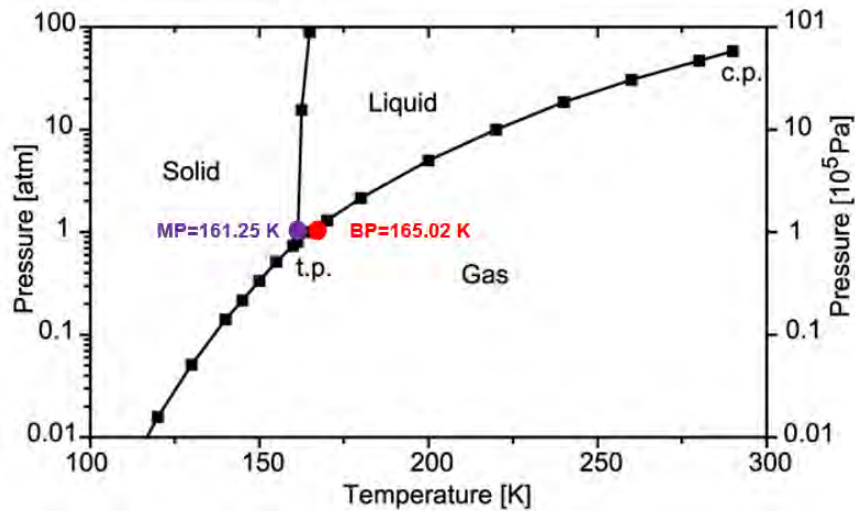


Figure 4.11: Phase diagram for Xenon [42] with the melting point (MP) [43] and boiling point (BP) [44] indicated on the graph.

There is a scarcity of experimental data regarding the vapor pressure of Xenon at 77 K. However, according to Podgurski and Davis [45], it is possible to estimate the vapor pressure

within the range of 70-90 K with Equation 4.2.

$$\log_{10} p = 8.044 - \frac{833.33}{T}. \quad (4.2)$$

In a literature review comparing vapor pressure curves to reported vapor pressure data, Grutter and Shorrock propose a correction to Podgurski and Davis' vapor pressure curve [46]. At 70 K, they recommend $\log_{10}(p) + 0.0028$, while at 80 K, they suggest no correction. From here, a correction of $\log_{10}(p) + 0.00084$ is derived for 77 K, resulting in a calculated vapor pressure of 1.67 mTorr. The recovery system ceases to pump Xenon out of ELOSS once the GHS reaches 1.67 mTorr. As a result, the XRS is capable of recovering over 99% of Xenon within the entire ELOSS GHS.

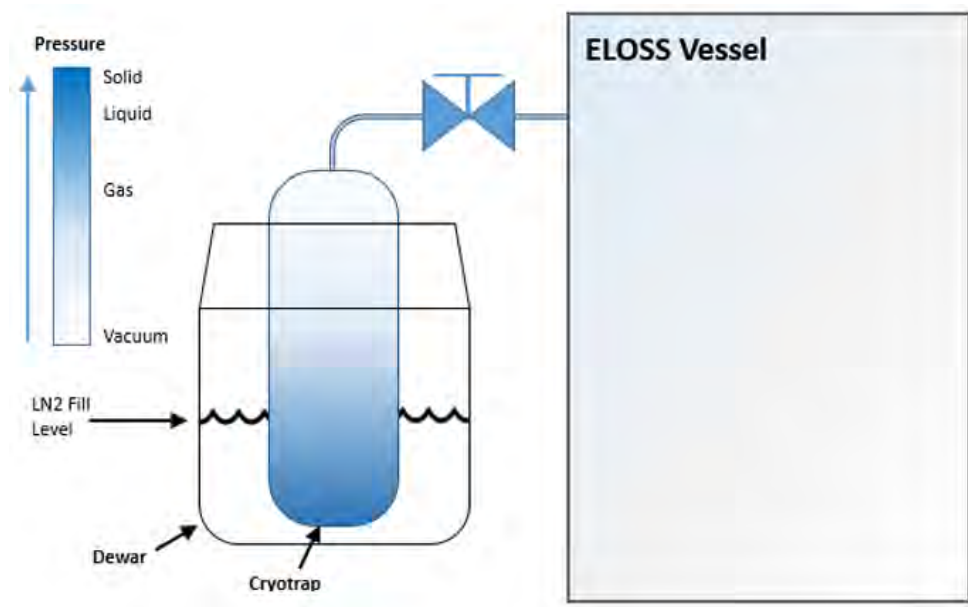


Figure 4.12: Drawing of Xenon Recovery System operational principle. As the cryotrap is submerged in liquid nitrogen, Xenon is drawn into the low-pressure cryotrap where it freezes.

Removing the cold trap coil from the LN2 dewar reheats the Xenon to room temperature and pressurizes the XRS. A 40 L storage bottle is connected to store the majority of the Xenon, maintaining the pressure in the XRS below 20 psi. The storage bottle can be opened

to the rest of the GHS to refill ELOSS as previously described.

Electronegative impurities, such as water or oxygen, absorb scintillation light and reduce the number of ionization electrons through capture [9]. Impurities are constantly outgassing into the Xenon from all components of the detector and the gas handling system. The purity of the Xenon in the detector mainly depends on two variables: the outgassing rate of impurities (O₂, N₂, CO₂, CO, H₂O, etc.) from the surfaces of the detector components in contact with the Xenon, and the efficiency of the purification system, which is related to its recirculation rate and the efficiency of the gas purifier. If the recirculation rate is sufficiently high and materials used for the various mechanical support of the detector components have low outgassing, the amount of impurities is sufficiently reduced to attain a high scintillation yield.

The purification system flows gas in a continuous recirculation loop through a GateKeeper purifier (model GPU 15). A miniature dry floating scroll vacuum pump (Scroll Labs, model SVF-5) drives the gas recirculation at a flow rate in the range of 30-50 SCCM, which is regulated by means of a fine adjustment valve. The rate is measured in real time using a digital flowmeter (Alicat, model MW-5SLPM-D). Reduction of the impurities to a sub-ppb level is achieved after a few hours of closed-loop recirculation. The continuous flow of gas across the effective volume of the detector will also ensure good radiation hardness through the replenishment of the detector medium.

Pressure gauges are stationed throughout the GHS and come in three different forms that sample different pressure ranges with high accuracy. The three gauges are a Pirani convection gauge [47], a capacitance manometer [41] and a cold cathode gauge [48]. The Pirani gauge and capacitance manometer work in a wide range of pressures that make them appropriate for monitoring the pressure during filling, operation and emptying. The pirani gauge is

calibrated to N₂, so its reading for Xenon is very inaccurate. However, it is exceptionally accurate in the mTorr regime for N₂, which makes it necessary for monitoring the pressure during air evacuation when the pressure goes below 1 Torr but hasn't reached below 1 mTorr. The capacitance manometer is useful in every stage of the GHS operation because it does not depend on the gas identity. Therefore, an accurate reading of Xenon is obtained with the capacitance manometer during filling and recovery of Xenon. The cold cathode is the only gauge of the three that measures below 1 mTorr, so it is critical during pump down. It ensures a sufficient vacuum has been reached before introducing Xenon into the system, effectively reducing the amount of impurities left over from the residual gas.

4.4 Interfaces

4.4.1 The Lid

The stainless steel lid of the ELOSS gas vessel, shown in Figure 4.13, serves not only as a support for the optical readout but also accommodates all necessary electrical feedthroughs. These feedthroughs, welded into the lid, enable the required electrical connections between the interior of the gas vessel and the external power and the electronics. There are six 25 pin DSUB Allectra vacuum feedthroughs, six high power rated SHV connections and six BNC connections. The DSUB connections take 120 biases in and 120 signals out of the detector. The SHV and BNC serve as utility feedthroughs used for pulsing internal test LEDs, biasing electrode foils and reading out electrode foils.

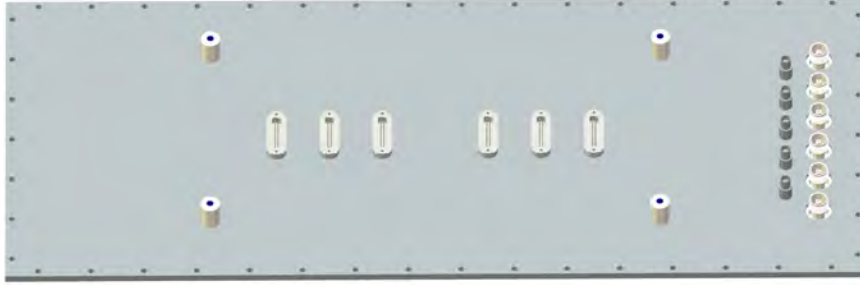


Figure 4.13: 3D model of the ELOSS vessel lid. It contains six 25-pin DSUB feedthroughs spaced down the middle, five BNC feedthroughs, and six SHV feedthroughs at the bottom of the lid.

4.4.2 Decoupler Crate

Conventionally, a PMT base will have an input for HV bias and an output for the anode signal. In an effort to minimize the number of cables/feedthroughs necessary for ELOSS within the S800 focal plane, an external decoupling circuit is employed to decouple the high voltage (HV) bias and fast signal pulses on each PMT anode. This approach, inspired by the PandaX experiment [?], effectively reduces the number of cables entering and exiting the detector from 240 to 120.

The decoupler crate serves as the interface between the HV power supply, data acquisition (DAQ) readout electronics, and PMTs. An overview of the optical readout is schematically represented in Figure 4.14.

PMTs are individually biased by an ISEG HV system using a Mpod EC main frame and three EHS 305 modules (48 HV channels up to 3 kV and 1 mA). Three 48 channel multi-pin cables with REDEL (R51.46) connectors equipped at both ends connect the ISEG HV modules to the front panel of the decoupler crate.

Eight HV adapter boards are mounted on the back of the front panel within the decoupler crate, as illustrated in Figure 4.15. Each custom PCB, designed using Altium Designer, is

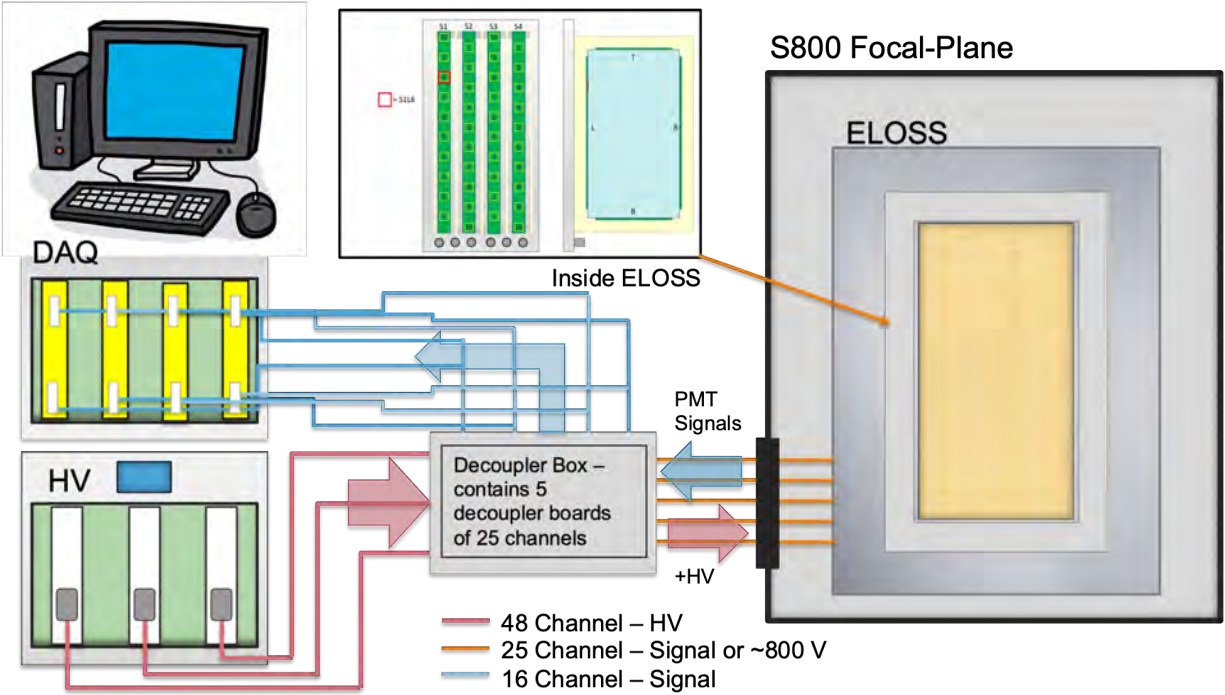


Figure 4.14: Optical readout connections schematic.

comprised of two 9-pin terminal blocks and an Amphenol ICC power edge card connector (10046972-001LF). The 128 HV wires are distributed among these eight adapter boards, with each terminal block receiving 8 HV wires. The three ground wires from each HV module's safety loop are routed to the three nearest HV adapter boards. These adapter boards are grounded to the front panel, ensuring that each safety loop is closed by the front panel, thereby avoiding noisy ground loops. Additionally, a foam backing is attached to each HV adapter board to insulate the boards from the conductive front panel, minimizing chances of a HV discharge.

The decoupler crate contains 128 decoupling circuits, distributed across eight custom decoupler PCBs, with each board housing 16 circuits. The schematic representation of these circuits and the Altium Designer view of the decoupler PCB is depicted in Figure 4.16 and 4.17. Each circuit comprised of a high voltage branch, a signal branch, and a PMT

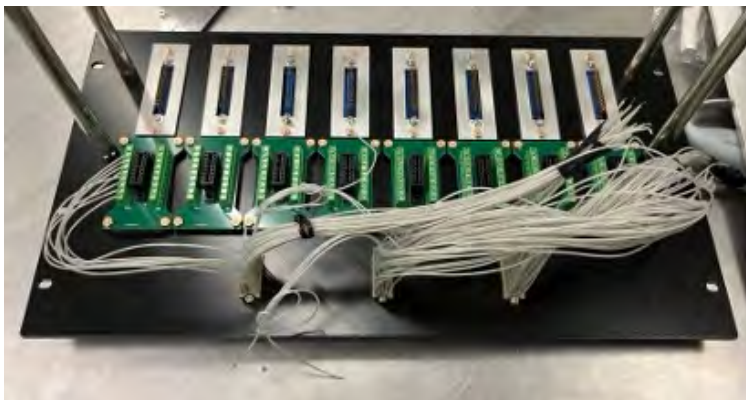


Figure 4.15: Decoupler Crate front panel under construction

input/output (IO). The HV branch incorporates three low-pass filters to eliminate noise introduced by the HV power supply and prevent the fast signal pulse from reaching the power supply. The signal branch includes a decoupling capacitor/high-pass filter, which blocks the HV bias and transmits the fast signal pulse to the readout electronics.

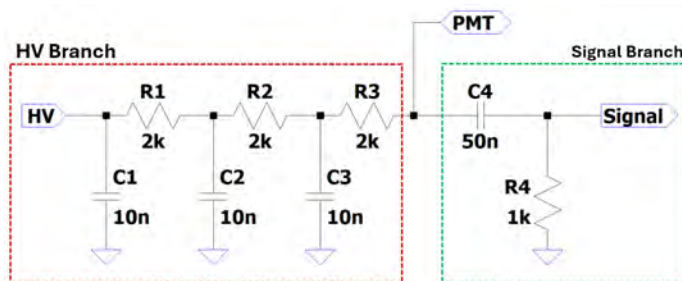


Figure 4.16: Decoupler circuit that delivers the HV bias to the PMT feedthrough and decouples the bias and anode signal pulse ahead of the MDPP input.

The decoupler PCBs, depicted in Figures 4.17 and 4.18, span the length of the decoupler crate. On the right side of the PCB, there are two board edge cutouts. The top is designed to be the key to the power edge connector on the HV adapter board. The bottom cutout is populated with 34 long solder pads (17 on each side) for soldering the long pins of a 34 pin rectangular header to. The board cutout fits between the two rows of pins so that each row gets soldered to a side of the PCB. The 34-pin header is fastened to a custom aluminum frame that attaches to the front panel (see Figure 4.15). This design was chosen

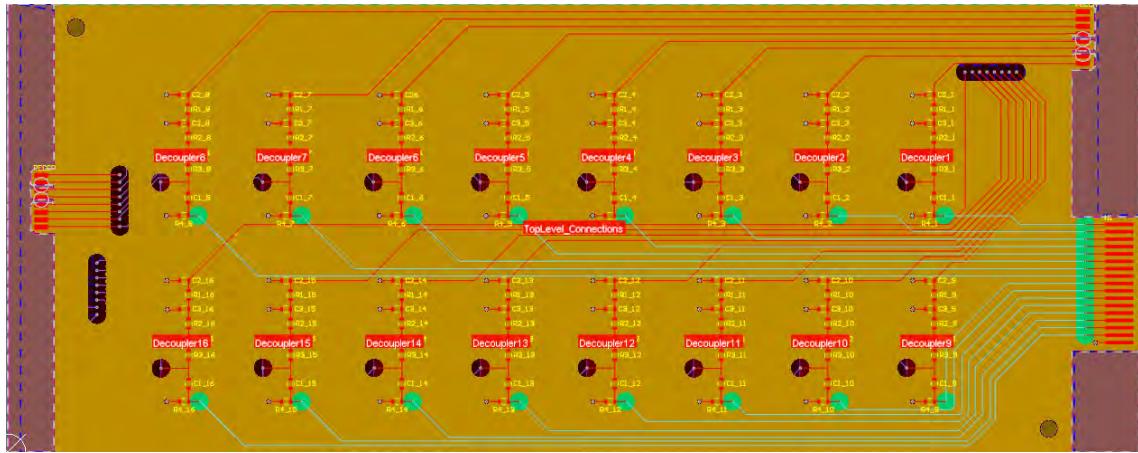


Figure 4.17: Altium 2D view of decoupler PCB. Contains 16 decoupler circuits shown in Figure 4.16 and three board edge connectors.

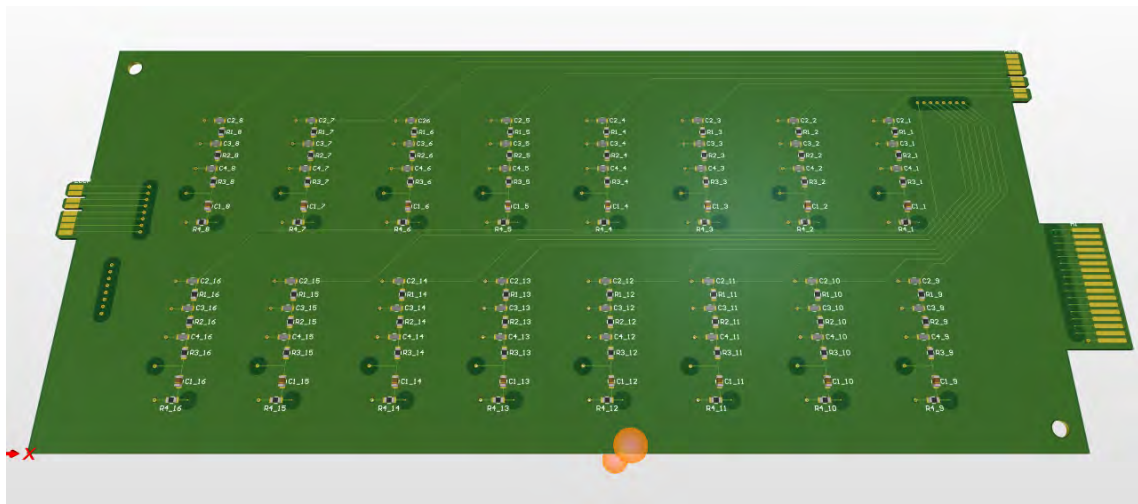


Figure 4.18: Altium 3D view of decoupler PCB.

to increase the decoupler crate's sturdiness without compromising its ease of disassembly. Each decoupler PCB is grounded to the front panel by a small wire. On the left side of the PCB is another power edge connector key, oriented for interfacing with the PMT adapter board that closes the decoupler crate.

An adapter board was developed to transition the eight decoupler PCBs into five 25-pin DSUB cables - see Figure 4.19. The board contains eight power edge card connectors to receive the PMT IO keys. On the opposite face of the adapter PCB are five 25-pin DSUB

connectors. The adapter PCB is fastened to a steel back panel with cut outs for the DSUB cables to pass through. The back panel grounds the adapter board and DSUB connectors. A common ground for the entire decoupler crate is achieved through metal rods that connect the front panel to the back panel. The metal rods also function as the main mechanical support for the decoupler crate. The 25-pin DSUB cables connect the decoupler crate to the ELOSS lid feedthrough for the delivery of the 120 PMT biases and readout of the fast signal pulses.

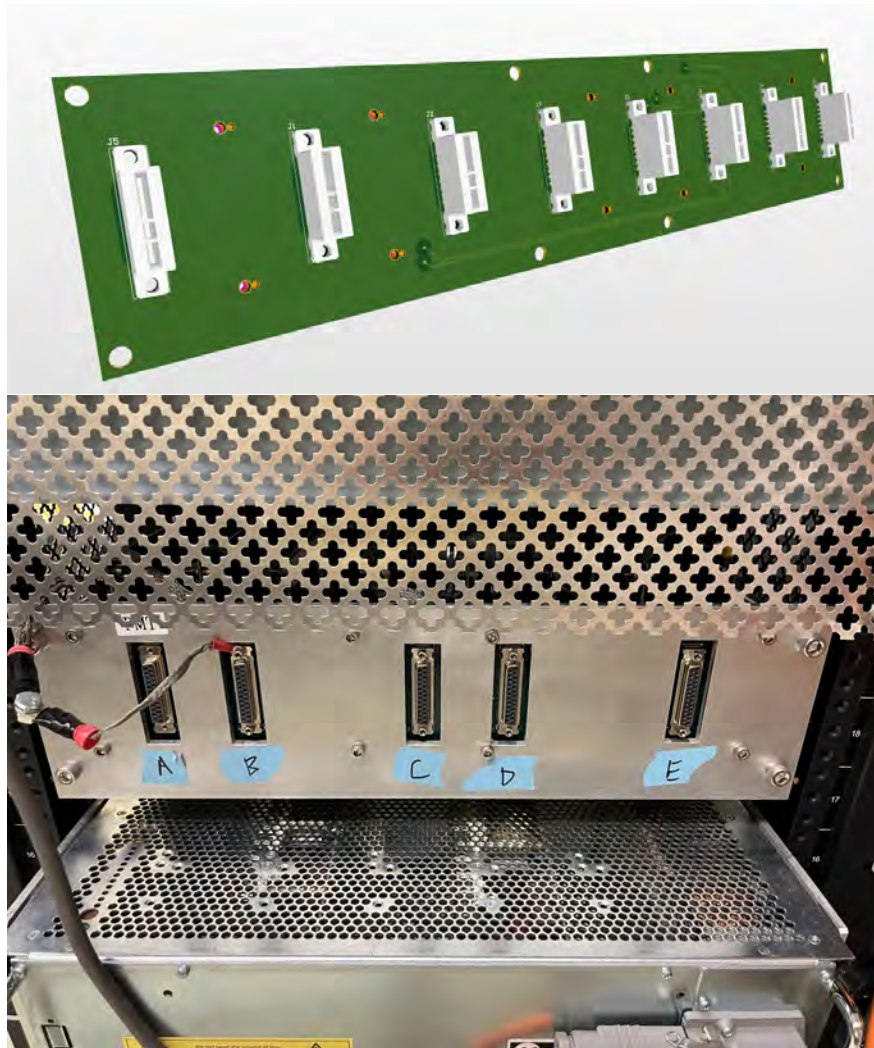


Figure 4.19: Top: 3D model of PMT IO adapter. Bottom: back panel view of the decoupler crate installed in the ELOSS electronics rack.

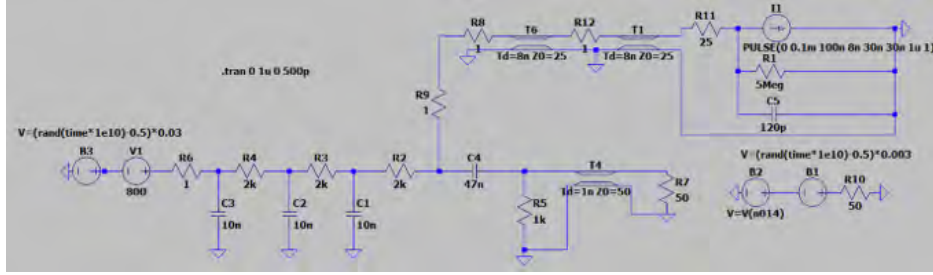


Figure 4.20: Circuit used to simulate the performance of the decoupler circuit and connections to the crate, namely the mismatched impedances over long cable lengths.

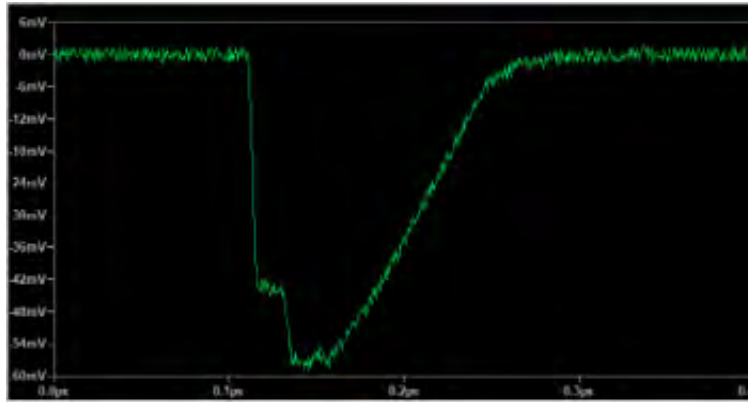


Figure 4.21: Signal measured across the 50Ω resistor resembling the readout electronics' input showing a compromise between reflections due to impedance mismatches and an acceptable signal-to-noise ratio.

The decoupler circuit and cable characteristics (impedance, length) were optimized using LTspice. Figure 4.20 shows the simulation circuit used to test the affect of impedance mismatches over variable cable lengths and choose resistor values to minimize reflections, while also extracting the largest signal possible. Current source $I1$ was set to a pulse shape and amplitude representative of the expected anode current from Xenon scintillation. Figure 4.21 is the pulse measured at the digitizer input, equivalent to about 100 photons incident on the PMT window.

4.4.3 ELOSS Channel Mapping

Interfacing 120 PMTs with specific voltage-divider circuits, multiple feedthroughs, a high-voltage (HV) power supply, a data acquisition system, and a decoupler crate requires a complex channel mapping procedure to ensure the proper operation of ELOSS. As detailed in Chapter 5, each PMT requires a unique voltage-divider circuit to achieve proper gain matching. Additionally, each PMT is calibrated with its own supply voltage adjustment to ensure uniform sensitivity across the entire detector. As a consequence, the voltage-divider and HV channel must remain fixed for each PMT. Going further, all connections to a PMT should remain unchanged to prevent discrepancies arising from variations in cables and passive components within the voltage-divider and signal readout circuitry.

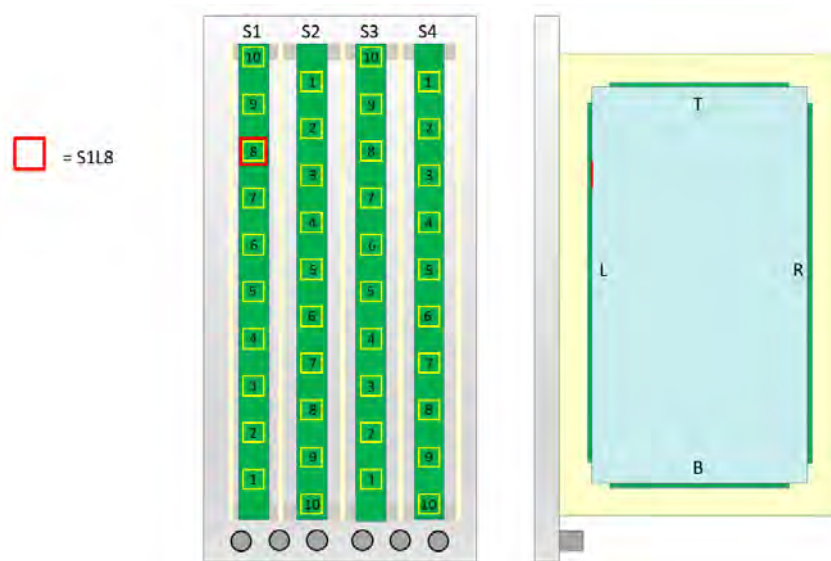


Figure 4.22: Schematic of PMT locations for the used naming convention.

Each PMT is characterized by a unique serial number engraved on the PMT body. Every PMT is assigned to a location within ELOSS that is equipped with its specific voltage-divider. These locations are labeled congruent to the schematic in Figure 4.22. Voltage-divider bases are identified by their location inside the detector and are always connected to the same

cable going to the detector feedthrough. Each cable exiting the detector is connected to a designated decoupler circuit number, which in turn is always connected to the same HV channel and QDC channel. Figure 4.23 represents the mapping of Sector 1 in ELOSS with each PMT installed in a specific location that has its own cable connecting it to the decoupler crate.

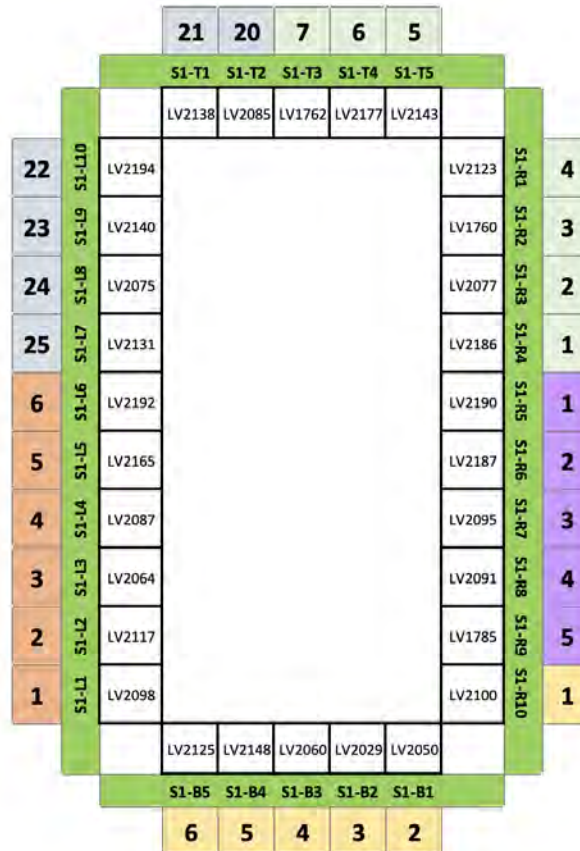


Figure 4.23: More detailed PMT location schematic with full naming convention. Includes PMT serial numbers and cables/channel numbers. Each color on the outer perimeter boxes corresponds to a cable assembly.

There are five cable assemblies, labeled A through E, consisting of 25 cables each. The cable assemblies connect to the 25 pin DSUB connector with the matching letter and are distributed to the eight decoupler PCBs inside the crate by the 8-to-5 adapter board. Each decoupler circuit is identified by the PCB it resides on and its circuit number (1-16). Decou-

pler circuits are connected to specific HV channels in the pattern shown in Figure 4.24 and likewise for the signal readout digitizer in Figure 4.25. The full channel mapping of ELOSS is provided in Appendix A.

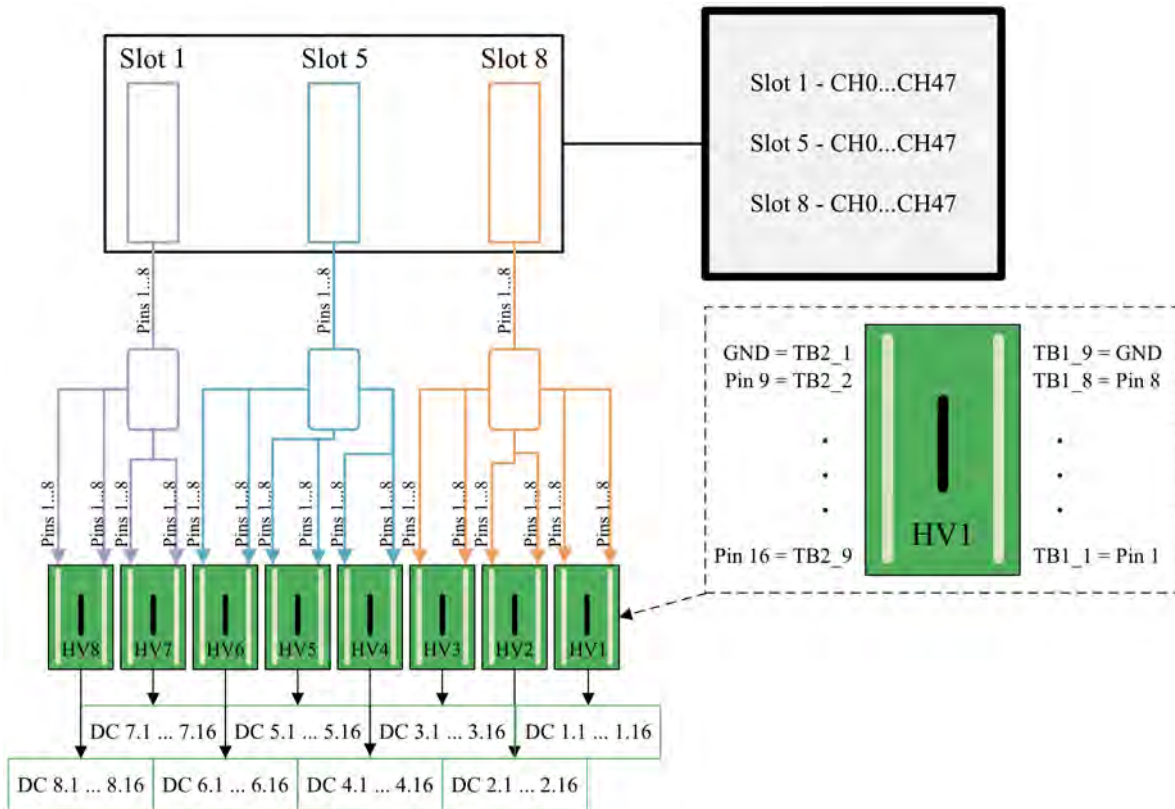


Figure 4.24: HV channel mapping showing three Iseg modules of 48 channels is connected to the decoupler crate and distributed to eight decoupler PCBs with the HV adapter board.

4.5 Data Acquisition System

The ELOSS data acquisition system (DAQ) is based on the Mesytec MDPP32-QDC [49] that processes the AC signals received from the decoupling capacitor of the decoupler circuit. The MDPP32-QDC combines the functionality of a fast charge-integrating analog-to-digital converter (ADC), a zero-crossing detector, a time-to-digital converter (TDC), and pulse shape discrimination into a single unit. A schematic representation of the hardware and

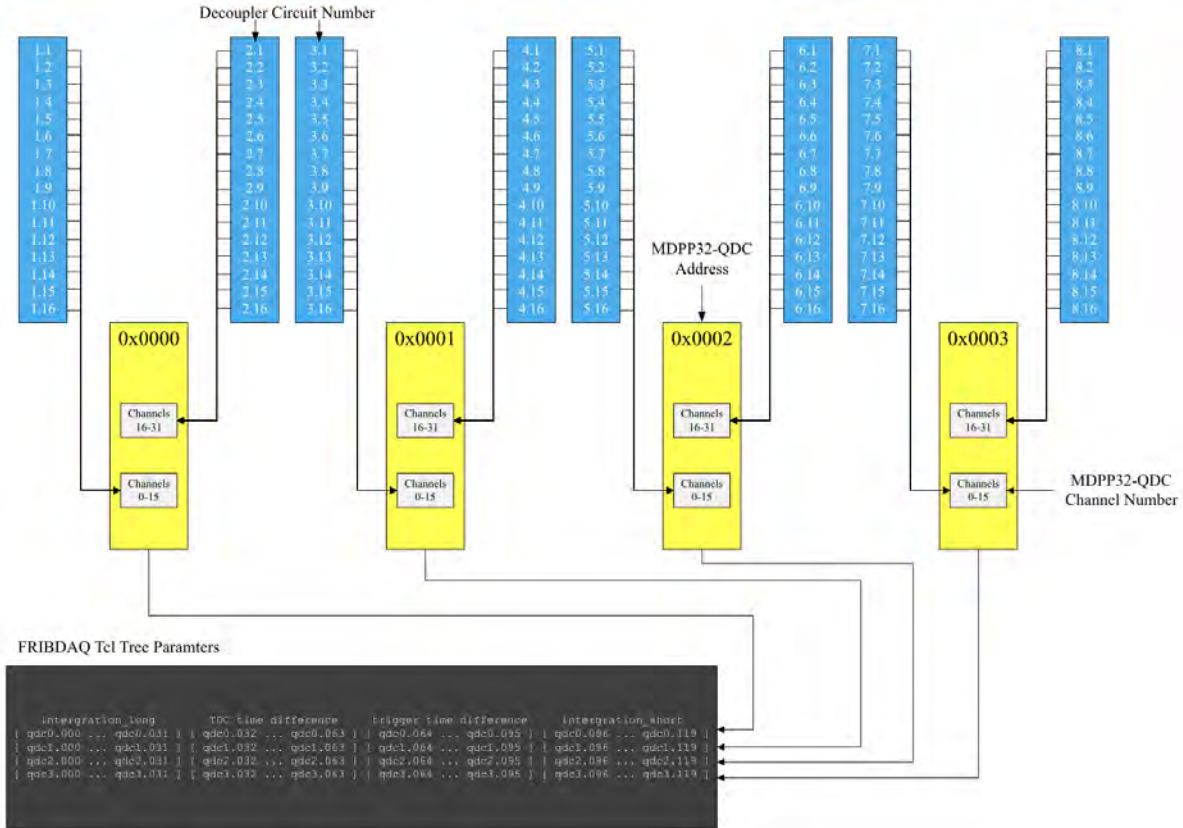


Figure 4.25: Signal readout mapping taking 16 signals per decoupler PCB to a input of one of the four MDPP32-QDC modules. Modules are named after their software address and the outputs of the modules are imported in the FRIBDAQ as Tcl tree parameters following the same naming as the QDC channels.

software within a MDPP32-QDC unit is provided in Figure 4.26.

The general pulse processing follows two branches, the charge-integrating digitizer branch numbered 1 to 12 in Figure 4.26 (red and blue) and the timing branch numbered 1 to 3 (green). Pulse processing begins with the signal input (1) from the 34-pin header, directed into a gain jumper chip that establishes the input impedance of the module, typically configured at 50 Ω . This setup can lead to impedance mismatches, as the ribbon cable's characteristic impedance is around 100 Ω , causing about a third of the signal amplitude to be reflected back. To minimize this issue, the ribbon cable should be as short as possible to reduce the return time of the reflected pulse, assuming total reflection at the other end.

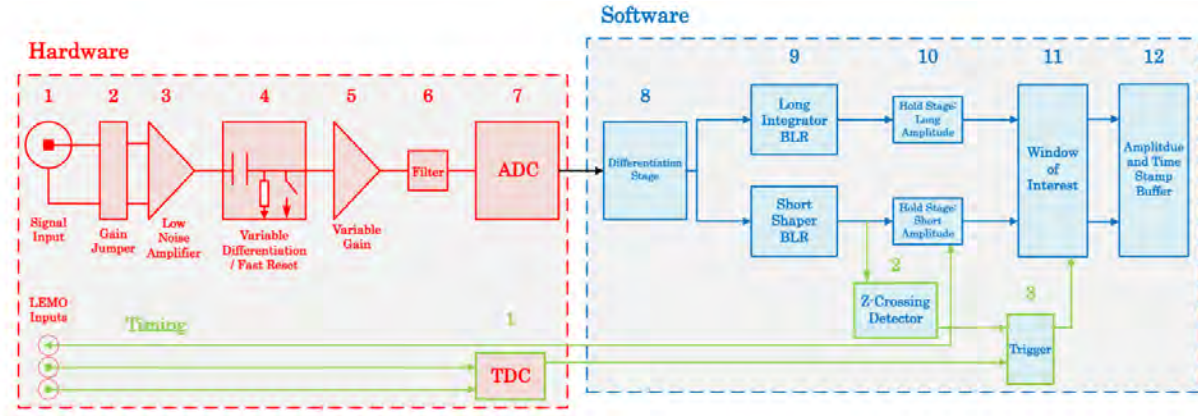


Figure 4.26: MDPF schematic of hardware and software components.

The selection of a gain jumper is fundamentally dependent on the signal's polarity and maximum amplitude. Two types of chip configurations are available: unipolar, which can toggle between positive and negative polarities by repositioning the jumper, and bipolar. In the context of the DAQ for ELOSS, the negative unipolar jumper chips are utilized, consistent with the negative polarity of the PMT pulses.

The signal amplitude expected from an ELOSS PMT is estimated to be about 1.35 V, determined using the typical maximum photon counts for a single PMT according to Geant4 simulations: 5000 photoelectrons (28% photon detection efficiency). For particles near the edge of the detector, close to the PMTs, a higher signal can be expected due to the greater solid angle coverage and subsequent detection of more photons. Therefore, it is appropriate to use a QDC gain jumper with a 2 to 3 V input amplitude.

The gain jumper that processes the PMT signal includes a low-noise preamplifier (3) and a variable differentiation stage equipped with a fast reset circuit (4) to quickly recover from large overflow and underflow signals. This stage eliminates the offset caused by the accumulation of pulses stacked on one another typical of charge-integrating preamplifier. A controllable gain stage (5) follows, offering a gain range of 1 to 24. The analog pulse is then

refined by a timing filter (6) before reaching the ADC (7). The digitized output pulse makes the transition from the hardware to the software side, the latter of which, in the form of a Field Programmable Gate Array (FPGA).

Within the FPGA, the digitized pulse goes through a differentiation stage (8) and is divided into two processing branches. The upper branch, the "long integration" QDC, typically set to integrate the entire pulse. The lower branch, the "short integration" QDC, first differentiates the digitized signal to produce a short pulse for pulse shape discrimination and timing. This short pulse is then analyzed by a zero-crossing detector (Green 2) to extract timing information, which is sent to the holding stage (10) and the trigger (Green 3). Optionally, the time computed from the zero-crossing detector can be output via the MDPP's front panel LEMO connector. Additionally, the front panel features two more LEMO connectors for external triggers, digitized by a TDC (Green 1) before reaching the trigger stage. The trigger establishes the start of the window of interest (11) and computes the time stamp for each pulse. This data is buffered (12) before being read out by the VME.

Achieving the best energy and time resolution with ELOSS necessitates the fine-tuning of several parameters within the MDPP software. These parameters, along with their typical values and permissible ranges, are detailed in Table 4.1.

Table 4.1: MDPP parameters

Parameter	Range	Units	ELOSS
Signal_width	1600	ns	50 ns
Input_Amplitude	3000	mV	3000 mV
Jumper_range	3000	mV	3000 mV
Integration_long	25 – 1600	ns	1000 ns
Integration_short	12.5 – 387	ns	84 ns
threshold	65535	N/A	500
win_start	± 25.56	μs	500 ns
win_width	25.56	μs	2 μs

Through Mesytec’s provided user interface, mvme, histograms of integration_long, integration_short and the time stamps can be generated. Details of the plots can easily be extracted such as the mean and RMS for any histogram with or without a Gaussian fit applied. However, for ELOSS to be added to the S800 focal plane detector system, its DAQ must be fully integrated into the existing FRIBDAQ. This would allow the S800 spectrograph to perform event-by-event data analysis and PID through the synchronization and merging of individual detector data streams into a single data stream.

The visualization of data streams from FRIBDAQ is performed using SpecTcl, a program that extends the Tcl/Tk scripting language, enabling users to write scripts and create graphical user interfaces. It focuses on creating histograms, defining conditions, and applying them to spectra, distinguishing it from a general-purpose analysis framework like Root. SpecTcl can process data from files and UNIX pipes, allowing real-time analysis during data

acquisition.

Chapter 5. PMT anode sensitivity calibration

5.1 Introduction

In large-area gaseous scintillation detectors like ELOSS, light recorded by the optical readout varies with the position of charged particles as they pass through the scintillating gas. As a result of this variation, the energy loss resolution is degraded. This can be mitigated by applying an energy loss correction factor to compensate for the differences in light collection efficiency on an event-by-event basis. However, this is only effective if the PMTs have uniform sensitivity. It is estimated an anode sensitivity variation of about 1% is tolerable for preserving the excellent energy resolution potential of ELOSS, according to simulation studies detailed in Chapter 6. This chapter will explore methods for obtaining uniform PMT sensitivity and then describe the anode sensitivity calibration procedure ultimately used for ELOSS.

5.2 Defining the anode sensitivity

Each PMT employed in ELOSS, under the same environmental conditions, is characterized by its anode sensitivity, generally defined as the anode current output per lumen of light. The anode sensitivity is the product of the photon detection efficiency (i.e. the quantum efficiency times the photoelectron collection efficiency) and the gain (i.e. the electron multiplication factor) expressed as

$$S_p = e\mu\text{PDE} \tag{5.1}$$

where

$$\text{PDE} = \text{QE} * \text{PCE}. \quad (5.2)$$

Typically, it is easier to measure the anode current produced in response to an incident light source rather than count photoelectrons [23]. Thus, the PMT response is frequently described by the anode sensitivity, measured in “current mode”, and expressed in mA/lm. In ELOSS, prompt scintillation from the excited Xenon gas arrives at the PMT arrays in bursts of light. Therefore, to maintain consistency with real experimental conditions, the ELOSS PMTs are described by their anode sensitivity measured in “pulse mode” where the charge collected on the anode is proportional to the number of photons incident on the photocathode. The total charge collected on the PMT anode is calculated by integrating the PMT’s output signal over a selectable time window using the MDPP32-QDC. For a known number of photons striking the light-sensitive area of a PMT, the anode sensitivity can be determined by measuring the charge at the anode.

The rest of this chapter considers the charge collected on a PMT’s anode per event, its response to an event, and its anode sensitivity as synonymous. All are presented in arbitrary units (a.u.) within a range of 0 to 65535; the number of channels in a MDPP32-QDC spectrum [49]. Each event’s `integration_long`, representing the integral of the digitized pulse (charge collected on the anode), is assigned a channel number and passed to a `SpecTel` spectrum window if its timestamp is within the trigger’s event window. The `integration_long` is histogrammed in a `SpecTel` spectrum with the number of bins equaling the number of QDC spectrum channels. Anode sensitivities measured in “pulse mode” for this thesis are obtained by applying a Gaussian fit to the `SpecTel` histogram of `integration_long` and recording the mean.

5.3 Anode sensitivity calibration methodology

Commercially available PMTs may vary by several orders of magnitude in anode sensitivity from tube to tube. To achieve optimal ELOSS performance, in terms of light measurement resolution, each PMT must have the same anode sensitivity. This ensures variations in photon counts are due solely to differences in light collection rather than discrepancies in PMT detection efficiency. It may be possible to identify 120 PMTs out of a large pool of PMTs that have similar or the same anode sensitivity, but this would be a very small fraction of the PMT pool. This is neither economical nor time-efficient; therefore, an anode sensitivity calibration that standardizes each PMT's sensitivity to a common value is necessary.

A PMT anode sensitivity calibration can be divided into two general approaches. The most common way is to adjust the physical operating conditions of each PMT that manipulate the anode sensitivity (hardware-driven method). The achievement of this goal must be accomplished without compromising the device's performance capability, particularly in terms of photoelectron collection efficiency, time response, and linearity. In the second approach (software-driven method), all PMTs have the same physical operating conditions (i.e. same supply voltage), but their output is multiplied by a correction factor during data processing. The downside of this approach includes the large dynamic range required by the QDC and the complex calibration procedure needed for correcting the accumulated data. Each correction factor is inherently tied to the anode sensitivity of the PMT it corrects. Thus, a precise anode sensitivity measurement would be needed for each PMT. While this is not a significant issue in and of itself, integrating it into the data acquisition process is challenging, particularly in regards to online monitoring of PID. Therefore, a hardware-driven approach has been adopted for calibrating the anode sensitivities of the ELOSS PMTs.

The total charge collected on the anode of a PMT is proportional to the number of photons incident on the photocathode based on equation 5.3.

$$Q_p = ne\mu\text{PDE} = ne\mu(\text{QE} * \text{PCE}) \quad (5.3)$$

In equation 5.3, Q_p is the charge collected on the anode, n is the number of photons that hit the photocathode, e is the charge of an electron, μ is the gain, PDE is the photodetection efficiency, QE is the quantum efficiency and PCE is the photoelectron collection efficiency.

Equation 5.3 can alternatively be expressed in terms of the anode sensitivity:

$$Q_p = \int_{t_{start}}^{t_{window}} n(t)S_p dt \quad (5.4)$$

where t_{start} is the starting time of the integration window, t_{window} is the window width, $n(t)$ is the number of photons hitting the photocathode as a function of time, and S_p is the anode sensitivity.

Identifying parameters to manipulate for an anode sensitivity calibration comes down to a choice between the variables in equation 5.1. The quantum efficiency is a function of the incident light's wavelength as shown in Section 4.1.1. Leveraging this relationship poses significant challenges. For instance, one potential approach involves covering each PMT window with a meticulously calculated wavelength shifter. This shifter would alter the incident light to a wavelength that matches the quantum efficiency required to offset the anode sensitivity correction. Achieving a tenfold correction in anode sensitivity necessitates shifting the wavelength from 175 nm to 600 nm with a precision better than 30 nm for the desired 1% anode sensitivity deviation. This assumes no quantum efficiency variation between PMTs exposed to the same incident light wavelength and a flawless calibration

setup, particularly regarding the accuracy and bandwidth of the light source. Therefore, calibrating the anode sensitivity by way of wavelength shifters that take advantage of the quantum efficiency spectrum of a PMT is impractical.

Photoelectron collection efficiency is primarily determined by the accuracy with which the photoelectrons are focused towards the first dynode, which in turn depends on the electric field established between the photocathode and the first dynode [23]. Generally it is not recommended to change the voltage distribution ratio between the photocathode, focusing electrode and first dynode because it is optimized for near 100% efficiency already, while preserving cathode linearity and limiting thermionic noise. In addition, PCE does not vary significantly for voltages within linearity, timing and noise constraints shown in Figure 5.1. On the other hand, the gain can be altered easily by the voltage applied to the dynodes. Thus, a PMT anode sensitivity calibration is accomplished by systematic gain corrections to individual PMTs utilizing a common light source with a consistent solid angle to normalize the light flux, i.e. fix n , the number of incident photons.

Generally, PMT gain adjustments are made by changing the voltage bias supplied to PMTs [23]. As stated earlier, this adjustment should be made without compromising the PMT's performance, therefore, the PMT supply voltage should deviate only slightly from the nominal operational voltage suggested by Hamamatsu (800 V), typically within ± 50 . For PMTs with a wide range of anode sensitivities, such as in ELOSS, a more aggressive gain adjustment is necessary before calibrating by supply voltage adjustments.

Adjusting the potential ratio of two center-stage dynodes has been demonstrated as an effective method for coarse gain adjustment in anode-biased voltage-divider circuits [23]. This results in a decrease in gain due to fewer secondary electrons being emitted and collected at those stages. While this method can be as precise as adjusting the supply voltage, it

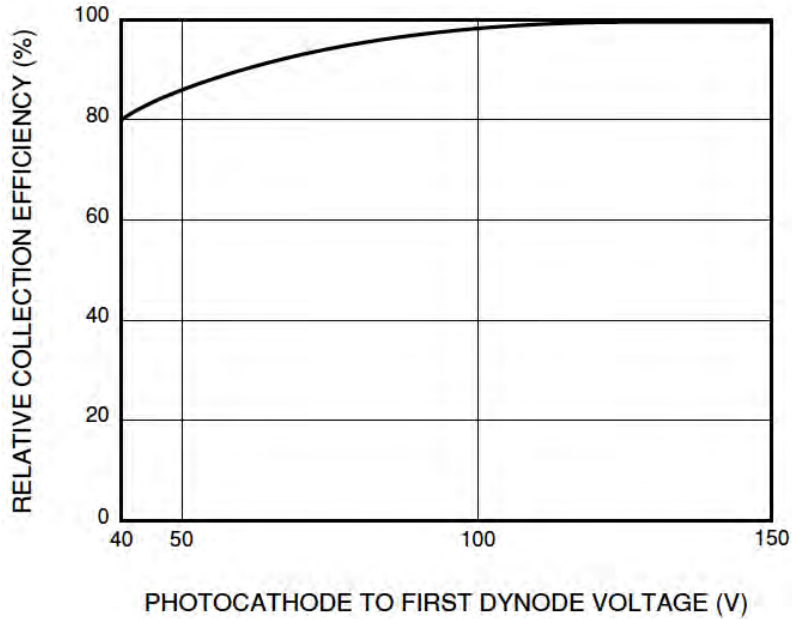


Figure 5.1: Photoelectron collection efficiency as a function of the potential difference between the photocathode and first dynode.

is constrained by time and resistor availability. For the ELOSS PMTs, the potential ratio between Dy6 and Dy7 is determined by the resistors R8 and R9 - see Figure 4.3 or Figure 5.5. Altering this potential ratio necessitates physically removing these resistors from the PMT base PCB, which is impractical for small gain adjustments that may vary over time. Consequently, this approach is reserved for coarse gain adjustments.

After the voltage-dividers for each PMT are modified to include their updated R8 and R9 resistances, a fine-tuned gain correction can be performed. Measurements of anode sensitivity are recorded for PMT biases 700 V to 850 V in steps of 25 V, skipping 725 V to avoid redundancy. The range accepted for voltage adjustment is larger than the ± 50 discussed earlier with the expectation that timing resolution will degrade for PMTs outside this range.

The whole calibration procedure for the ELOSS optical readout PMTs is divided into three stages. The first stage involves characterizing each PMT by measuring its relative

anode sensitivity as a function of the supply voltage, comparing it to the values reported by Hamamatsu in the datasheet provided with each PMT. This validates the “pulse mode” measurement technique before proceeding to the second stage. In the second stage, a coarse gain correction is performed by measuring the anode sensitivity with varying center stage potential ratios. A resistance ratio of R8:R9 (potential ratio of Dy6:Dy7) needed for lowering the gain is determined and resistors close to the calculated resistances are mounted on each voltage-divider PCB. The third stage completes the calibration by measuring the anode sensitivity as a function of the voltage supplied to each PMT, fitting it to an exponential relationship to extract a calibrated supply voltage. Deviations from exponential behavior above 800 V are corrected with minor adjustments to the calculated supply voltages, ensuring accurate gain adjustments, responsible for a consistent anode sensitivity across the whole optical readout.

5.4 Description of the Calibration Setup

5.4.1 Initial Characterization

The initial characterization of the R8520-406 PMTs was performed using the setup shown in Figure 5.2. The main support structure was designed and 3D-printed with the intent of each PMT receiving the same level of illumination by keeping solid angle coverage constant. One PCB base, responsible for biasing and reading out a PMT, was used for every PMT characterization to eliminate discrepancies in the measured anode sensitivities that arise from artificial sources such as variations in the passive components of the voltage-divider. The PCB base in the initial characterization setup, pictured in Figure 5.3, is identical to the

Hamamatsu-suggested circuit except the total resistance was reduced to $10\text{ M}\Omega$, while still maintaining the same voltage distribution. This PCB design served as the prototype for the PMT array PCBs later used inside ELOSS.

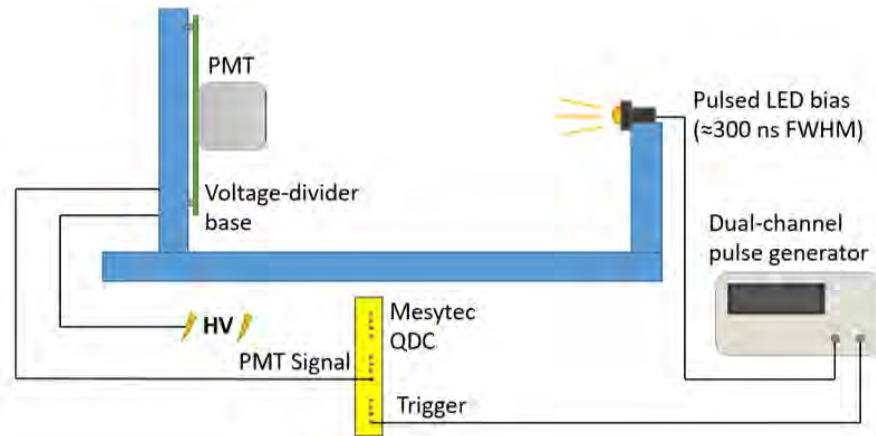


Figure 5.2: Initial characterization setup for the anode sensitivity calibration.

Facing the PMT is a low-intensity LED with a spectral range spanning the visible spectrum, peaking around 585 nm [?]. The LED illuminates each PMT installed in the support stand at an equal distance and angle, ensuring equivalent light collection efficiency (equal n) for each characterization. It is important to note that the value of n is unknown, but the differences in n for each characterization are approximately zero, so n drops out of equations 5.3 and 5.4. This to say that the anode sensitivities reported are technically “relative” anode sensitivities.

A dual-channel function generator (Tektronix AFG3102C [50]) provided simultaneously a short triangular pulse for biasing the LED (Figure 5.4 - left hand side, yellow line) and a NIM-like pulse for triggering the data acquisition (DAQ) (Figure 5.4 - left hand side, blue line). The LED pulse mimics the triplet state exponential decay of Xenon scintillation with a 5 ns rise time (smallest possible with the function generator), 30 ns pulse width, and 48 ns fall time. An example PMT output signal, corresponding to a single LED light pulse, is



Figure 5.3: PMT base PCB used for the initial characterization of each PMT. PCB is fastened to calibration stand support structure and its components are painted with insulating varnish to prevent discharges.

shown in Figure 5.4 (right hand side). The PMT is biased at 800 V using the voltage-divider circuit depicted in Figure 5.5, ignoring the custom potentiometer also pictured.

5.4.2 Course gain correction

The course gain correction stage replicated the setup in Figure 5.2 with one modification: replacing resistors R8 and R9 in Figure 5.5 with a custom potentiometer. This potentiometer, a standard breadboard with sixteen $100\text{ k}\Omega$ resistors in series, created a total resistance of $1.6\text{ M}\Omega$, matching the sum of the original R8 and R9. The left side of the resistor chain was connected to Dy6, and the right side to Dy8. A wire connected to Dy7 controlled the resistance ratio by moving along the resistor chain. The tested R8:R9 ratios ranged from $100\text{ k}\Omega:1500\text{ k}\Omega$ to $1500\text{ k}\Omega:100\text{ k}\Omega$ in steps of $100\text{ k}\Omega$.

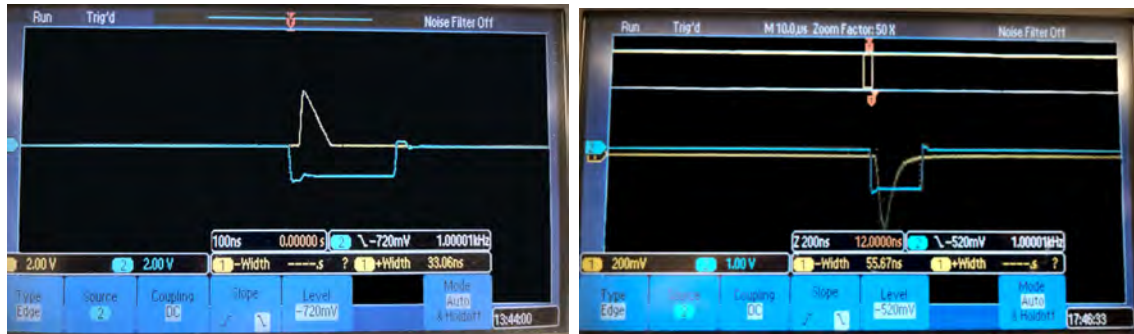


Figure 5.4: Left-hand side: LED-bias pulse in blue with shape loosely representative of Xenon’s triplet decay scintillation and the NIM-like DAQ trigger pulse in yellow. Right-hand side:

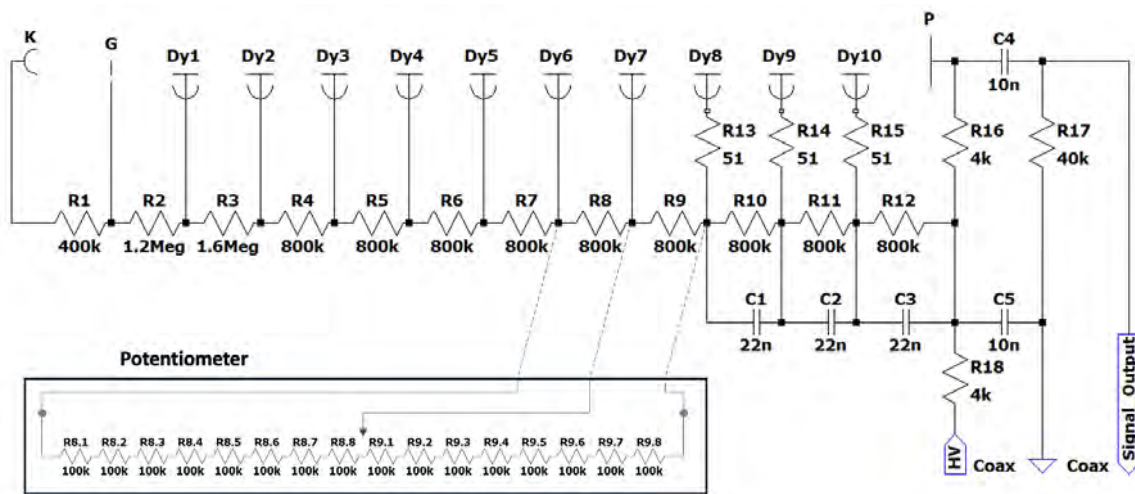


Figure 5.5: Voltage-divider schematic for the first two stages of the calibration. The custom potentiometer was utilized in the second stage only in place of R8 and R9.

5.4.3 Fine-tune gain correction

During the fine-tune gain correction stage, the focus shifted from calibrating 120 PMTs to calibrating the entire optical readout system. Achieving a uniform ELOSS response involves more than just collecting the same amount of charge on every PMT anode for the same light levels. Factors such as cables, variations in the passive elements of the voltage-divider and decoupling circuitry, and QDC gain jumper chips contribute to the overall ELOSS response as well. These variances can accumulate throughout the full readout scheme, potentially

resulting in more than a 1% response variation, even if the anode sensitivity is perfectly matched for every PMT. Consequently, the fine-tuned gain correction must include the unique voltage-divider base for each PMT updated with the course gain correction resistor configuration. In addition, each PMT and voltage-divider base was evaluated with the cables, feedthroughs, decoupling circuit, HV channel, and QDC channel that they will use in an experiment, following the optical readout mapping presented in section 4.4.3.

The initial characterization and course gain correction were conducted in a light-tight vacuum chamber approximately $45\text{ cm} \times 45\text{ cm} \times 45\text{ cm}$. However, this chamber could not accommodate the 60 cm long vertical PCBs, necessitating the use of the PMT Gain Correction Stand in Figure 5.6.

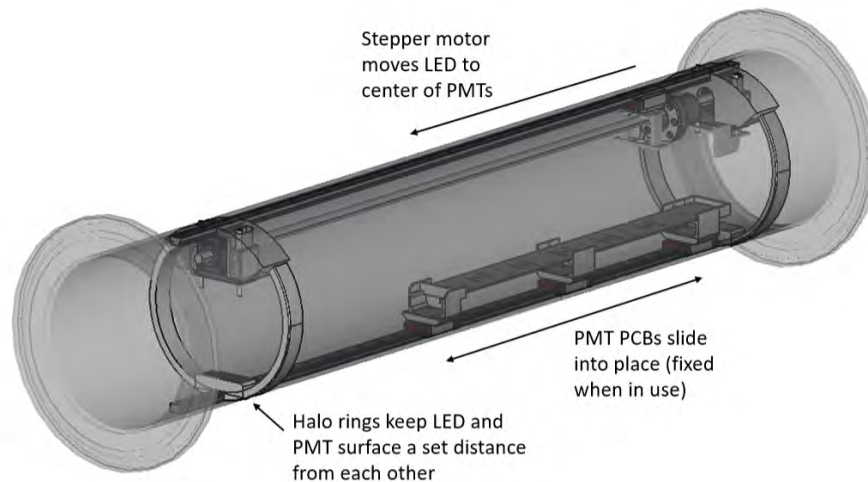


Figure 5.6: 3D model of the PMT Gain Correction Stand used for the fine-tuned gain corrections with a UV-C LED.

The LED used in the initial stages of the calibration was replaced with a Far UV-C LED manufactured by Silanna (SF1-3T9B5L1, [51]), which is characterized by its 235 nm peak wavelength and 9 nm bandwidth. This change from a visible LED to a UV-C LED was intentional, as it allows the PMTs to be tested closer to Xenon's 175 nm spectral peak [25]. By aligning the testing conditions closer to the expected spectrum, the calibration process

can more accurately account for the PMTs' response to Xenon's emission wavelength. This adjustment helps to mitigate uncertainties in the anode sensitivity calibration that arise from quantum efficiency fluctuations, which can vary from tube to tube and are dependent on the wavelength of light.

It is well-documented that oxygen and other contaminants, such as water vapor (H₂O), are highly effective at absorbing UV light below 200 nm [52]. Despite the LED emitting above 200 nm, an alternative medium to air was chosen to avoid any potential light attenuation. Therefore, the gain correction stand was filled with atmospheric Argon (Ar), which is transparent to 235 nm light. This precaution was taken because even slight variable attenuation could affect the anode sensitivity from one measurement to the next.

A steel tube, about 1 m long and 16.8 cm in diameter, was used as the main capsule for the custom vacuum chamber. It included two VCR fittings, one at each end of the tube, facing opposite directions and perpendicular to the tube's length. They were installed to fill, evacuate and optionally flow Argon through the correction stand. Gas flow reduces the concentration of light-attenuating contaminants over time [?]. Stainless steel ISO200 flanges were counter-bored to the tube's outer diameter and welded at each end. The left end of the tube in Figure 5.6 was closed with a stainless steel ISO200 flange. The flange features an Allectra 25-pin DSub feedthrough welded in the center, along with a standard 14-pin male-to-male rectangular header vacuum sealed with epoxy inside a cutout just above the 25-pin DSub. The opposite end was closed off with a blank ISO200 flange made of aluminum.

In an effort to minimize the time spent filling and evacuating the correction stand with Argon between moving the LED, a motorized ball screw assembly was designed and installed. The ball screw assembly consists of a 65 cm long RM1605 ballscrew, 80 cm long linear rail guide with a MGN12H slider block, and 3D-printed LED holder designed to mount to the

slider block and nut of the ball screw. An enlarged view of the interconnection between the ballscrew, linear rail/slider block and LED holder is depicted in Figure 5.7.



Figure 5.7: Up close view of LED holder assembly. It fastens to the nut of the ball screw and top of the slider block to group the separate components together.

The end supports for the ballscrew (a BK12/BF12 kit) were mounted to the tube wall using custom 3D printed holders. These holders matched the tube radius, ensuring they remained parallel to the tube wall's tangent. Stud bolts at each end of the tube secured the ball screw assembly, enabling consistent ballscrew assembly/LED placement. A small slot at the bottom of the holders allowed the linear rail to fit through, holding it in place without additional studs.

A Nema17 stepper motor was mounted to the left end of the ball screw using a flexible coupler that allowed for smooth turning regardless of the alignment precision between the motor axis and ball screw axis. The motor was controlled by an Arduino UnoR3 and driven by a L298N motor driver, all together, capable of 25 μm steps at 5% accuracy [?]. The motor leads were connected to the driver through the 14-pin feedthrough. The motor was held in

place by a 3D-printed ring (same diameter as the inside of the tube) with bracket arms to hold the motor and keep it from turning.

Opposite the motorized ball screw assembly with the LED was a second linear rail system with three slider blocks on it. This was used to slide the PCBs containing a full PMT array into the gain correction stand without compromising the safety of the PMTs. Unique 3D-printed carriers were designed for each end of the short and long PCBs, as well as a middle support carrier. The carriers were fastened to the three slider blocks to securely connect the PCB to the linear rail. The PMT array, placed in the carrier blocks, slides into the calibration stand until reaching a rubber stopper inserted into the rail. A second rubber stopper is inserted into the rail behind the last carrier block, so that the PMT array can't move. 3D-printed halo support rings completed the circle of the inside tube surface started by the end support holders as shown in Figure 5.6. Similar to the end support holders, a small slot for the PMT array rail was left in the rings that when correctly installed, kept the rail from moving. They were also designed to ensure to position the rail perfectly across the the LED rail, so the PMTs and LEDs lined up center to center.

The PMTs were biased and readout using the same cables that would operate them inside ELOSS according to the channel mapping detailed in Appendix A. Only five cables were needed at a time. Thus, they were separated from the 20 other cables and bundled in the motor region of the PMT Gain Correction Stand. Care had to be taken to ensure cables would not be in the path of the LED mover or disrupting the light path to a given PMT. The LED was biased with a dual channel function generator () through a coaxial cable split into two pins for the 14-pin header feedthrough and continued as a coaxial cable inside the tube terminated by an SMA connector at the LED. The coax cable inside the tube was looped in such a way that the movement of the LED would not stress the cable.

A limit switch was installed at the far end (right side in Figure 5.6) ball screw support holder. Activation of this switch indicates that the LED has reached the “HOME” position. The position of each PMT was defined within the LED movement control system in reference to this “HOME” position. A custom Arduino shield-type PCB was designed to interface the Arduino UnoR3 with the “HOME” limit switch and the motor controls. Additionally, it includes a second, optional limit switch circuit, four push buttons, a +12 V power input, an LED power input and break-off PCB, and a L298N motor driver module. The button functions are detailed in Table 5.1 and the Arduino shield PCB is depicted in Figure 5.8 and the full schematic is in Appendix ???. A 14-pin ribbon cable connects the LED movement controls from the Arduino shield PCB to the gain correction stand.

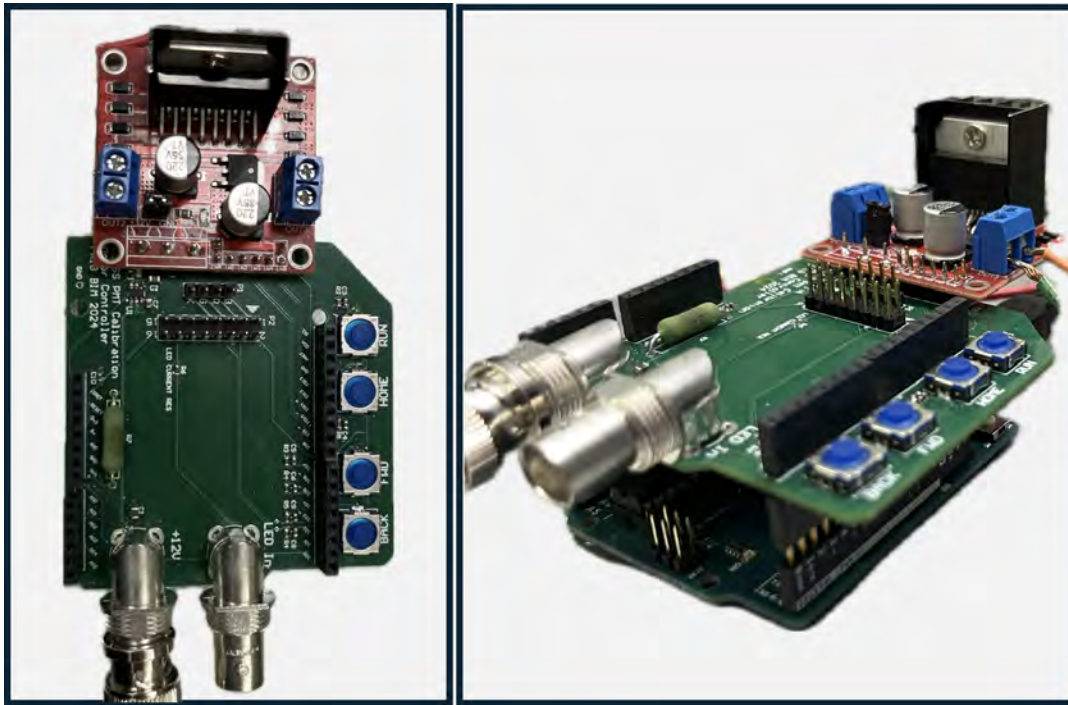


Figure 5.8: Arduino shield PCB containing the interface between the operator, Arduino, motor driver, motor and limit switches.

Table 5.1: MDPP parameters

Button	Function
HOME	Checks to see if LED is at HOME position. If it isn't, moves the LED toward home until the HOME limit switch is activated. Calls the FWD function.
FWD	Checks to see if LED is at HOME position. If it isn't, moves LED d distance towards the HOME position, where d is the distance between PMTs (set to 60.0 mm).
BACK	Same as FWD, except it moves the LED away from HOME position.
RUN	Moves LED from HOME position to the first PMT position.

Each component chosen or designed for the PMT Gain Correction Stand serves the same overarching purpose: to reduce the uncertainty in LED positioning to less than 1 mm and ensure every PMT is illuminated with the same number of photons.

5.5 Results

The initial characterization of an example PMT, illustrated in Figure 5.9, involved measuring anode sensitivity as a function of PMT supply voltage, using the setup shown in Figure 5.2. The graph reveals an exponential relationship between anode sensitivity and bias voltage, which can be utilized to determine the supply voltage required for calibrating the anode sensitivity. However, the initial anode sensitivity variation for the set of PMTs is too large to calibrate by this method solely without impacting performance characteristics such as timing and linearity. This reinforces the idea presented earlier that a coarse gain correction must precede a gain correction/anode sensitivity calibration by supply voltage adjustments.

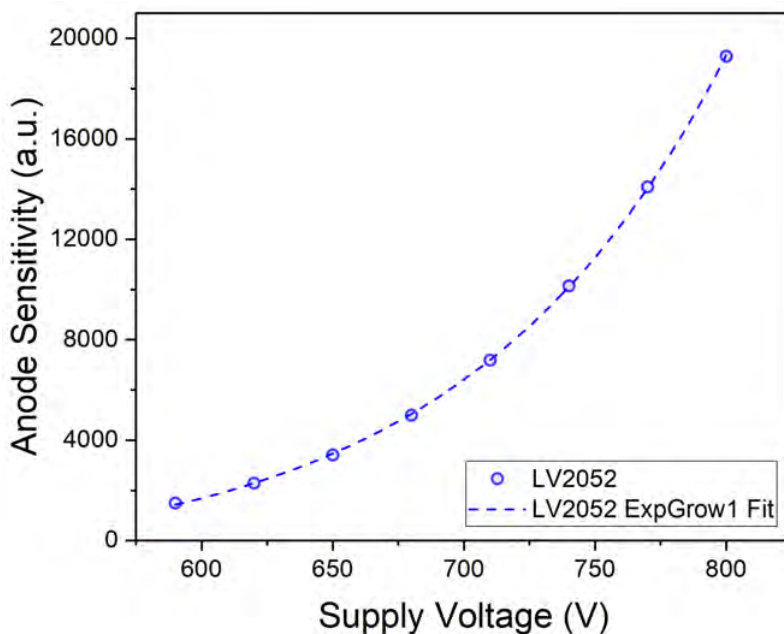


Figure 5.9: Example of a PMT’s initial characterization, measuring the anode sensitivity as a function of the voltage supplied.

Figure 5.10 shows a reasonable agreement between the anode sensitivity measured in “pulse mode” at FRIB and the anode sensitivity measured in “current mode” at Hamamatsu with constant illumination from a 2856 K Tungsten lamp [23]. The calibration setup and

procedure were considered valid at this point and the relative anode sensitivities serve as a reference point for the future measurements in the calibration.

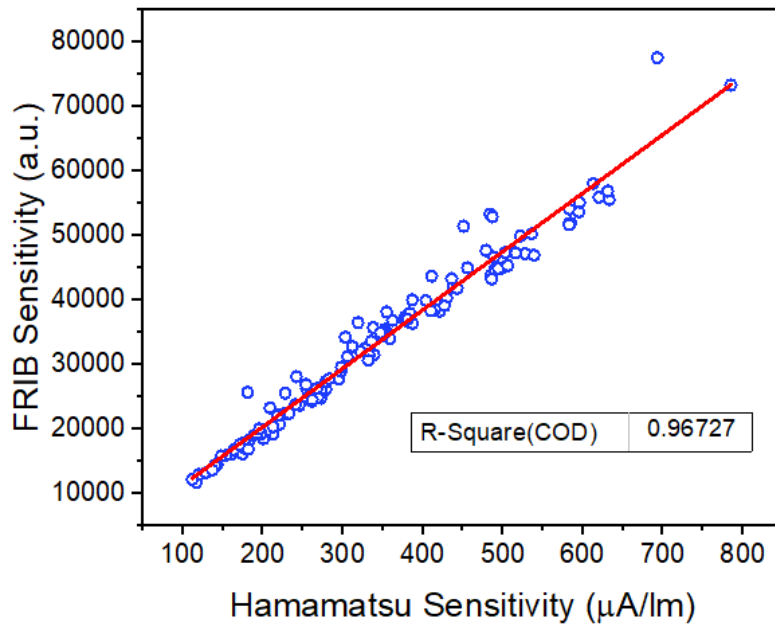


Figure 5.10: Comparison of the anode sensitivities measured by Hamamatsu in “current mode” and anode sensitivities measured in “pulse mode” for this study.

The anode sensitivity as a function of the ratio of resistances for R8 and R9 was measured for six PMTs. Each PMT picked for this measurement had a significantly different anode sensitivity measured at 800 V in the initial characterization. This was intended to capture a range of different performing PMTs to make sure the relationship between anode sensitivity and potential ratio is the true for all PMTs, not dependent on anode sensitivity. Figure 5.11 (left-hand side) shows the anode sensitivity vs. resistor ratio for the six PMTs and Figure 5.11 (right-hand side) shows those PMT sensitivity curves normalized by their anode sensitivity measured at 800 V for the original 800 kΩ:800 kΩ resistance ratio. The overlap of all of the normalized PMT sensitivities indicate that this relationship should be expected for every PMT. Taking the average of the six PMT sensitivities at each resistor ratio produces a universal relationship. Fitting this plot with a 5th degree Polynomial yielded an equation

that could be exploited for finding the resistor ratio needed to course gain correct each PMT.

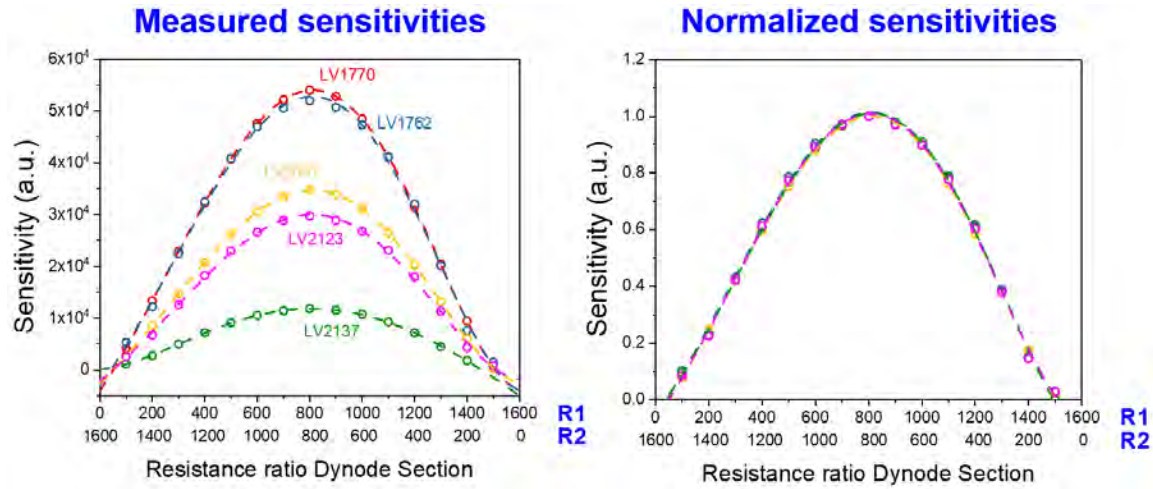


Figure 5.11: Left hand side: example of a few PMT sensitivity curves with respect to the center-stage resistor ratio. Right hand side: same plots of left hand side normalized by their maximum.

The resistance ratio for each PMT was calculated via

$$S_p = c_0 + c_1x + c_2x^2 + c_3x^3 + c_4x^4 + c_5x^5, \quad (5.5)$$

where

$$\begin{aligned} c_0 &= -0.07194, \\ c_1 &= 0.14067, \\ c_2 &= 0.01286, \\ c_3 &= -8.6065e-4, \\ c_4 &= -1.75868e-4, \\ c_5 &= 9.06807e-6, \end{aligned} \quad (5.6)$$

and is divided by 2 because the calibration stand R_8+R_9 is $1.6 \text{ M}\Omega$, while the ELOSS R_8 and R_9 sum to $800 \text{ k}\Omega$. A batch of resistors were purchased that cover the resistance

range 0 k Ω to 800 k Ω , stepping in resistances of about 15 k Ω . Each calculated resistor ratio was substituted with the nearest resistors out of the available batch. After populating the individual PMT bases on each ELOSS PCB with the corresponding resistor configurations, the variation in anode sensitivities measured at 800 V, using the PMT Gain Correction Stand, is depicted in Figure 5.12. The anode sensitivity for each PMT was measured at three different light intensities corresponding to the lower limit (LED1), average (LED2) and upper limit (LED3) of expected light yield for a typical experiment using Xenon inside ELOSS. The anode sensitivity variation is reduced from the roughly 40% σ measured in the initial characterization stage (before course gain corrections) to 20% σ (LED1), 17% σ (LED2) and 15% σ (LED3) after the course gain correction.

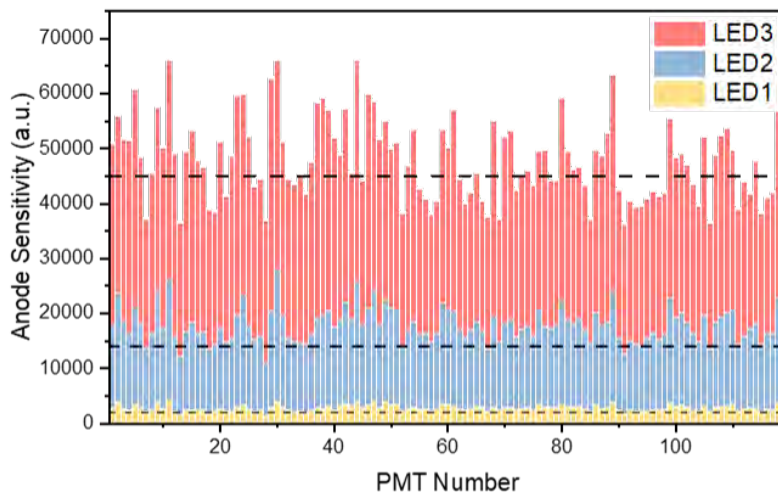


Figure 5.12: Anode sensitivities measured for all 120 PMTs after the course gain correction for 3 different light intensities. Dashed lines represent the target sensitivity for each light intensity.

Each PMT was re-characterized with their new resistor configuration and the new light source (UV-C LED). The anode sensitivity was measured for different supply voltages going from 700 to 850 V in steps of 25 V (skipping 725 V), which is a restricted range compared to the initial characterization because the maximum voltage excursion was imposed to keep

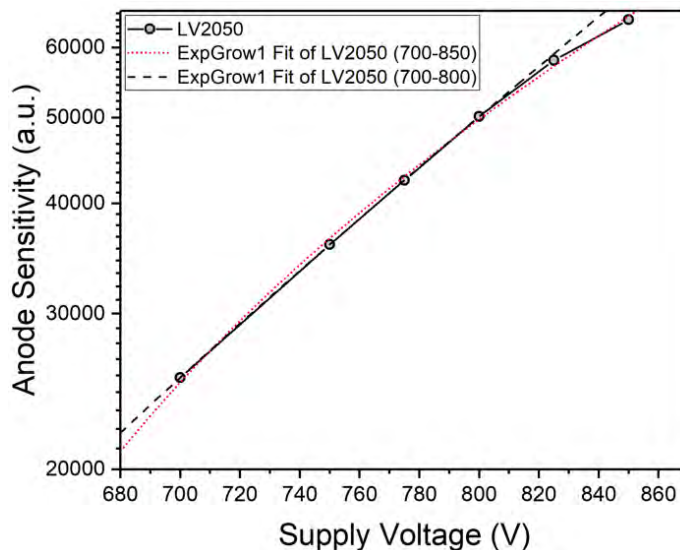


Figure 5.13: Example of anode sensitivity measured as a function of the PMT bias after the course calibration. The red dotted line represents the exponential fit using the sensitivities measured from 700 V to 850 V and the black dashed line represents the exponential fit using sensitivities only from 700 V to 800 V.

the PMTs from varying voltage too much and affecting the performance parameters. An example of one such re-characterization is graphed in Figure 5.13. By fitting the anode sensitivity data with an exponential growth function, a benchmark sensitivity can be interpolated and the voltage corresponding to that sensitivity can be obtained for calibration. After measuring the anode sensitivity of every PMT after setting the supply voltages to the calculated calibration voltage, Figure 5.12 is updated with these sensitivities to get Figure 5.14. The anode sensitivity variation is reduced to 1.42% σ (LED1), 1.29% σ (LED2), and 1.00% σ (LED3).

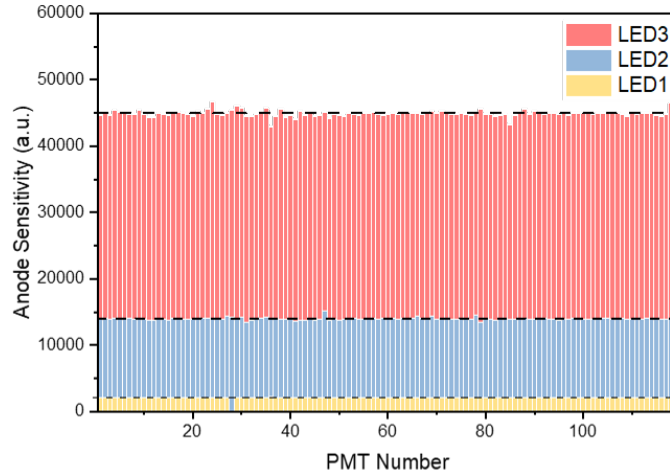


Figure 5.14: Same as Figure 5.12, but after supplying the PMTs with the calculated calibrated voltages.

As shown in Figure 5.13, the PMT response deviates from its exponential behavior above 800 V causing a skewed fit, indicated by the difference in the black dashed line and red dotted line. The black dashed line represents the exponential fit using only the data points measured at 800 v and below, while the red dotted line is the fit that was used in the calculation of the calibration voltage. This relatively small error was corrected by small voltage adjustments to match the benchmark anode sensitivity for each light intensity, resulting in a final anode sensitivity variation of 1.05% σ (LED1), 0.69% σ (LED2), and 0.38% σ (LED3) shown in Figure 5.15.

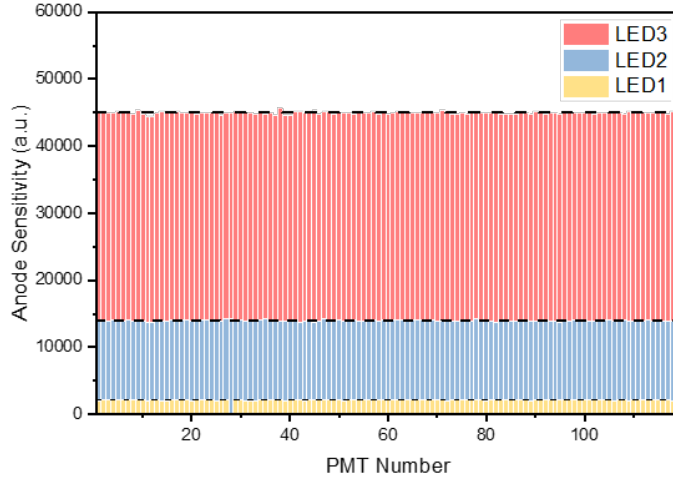


Figure 5.15: Same as Figure 5.14, but after the final calibration process.

Overall, the anode sensitivity variation was reduced by a factor of 40-80 times, ultimately reaching 1% and lower variation, successfully calibrating the anode sensitivities of the ELOSS PMTs.

5.6 Discussion

Two primary questions arise when evaluating the results of this PMT calibration. Firstly, what is the impact on the ELOSS energy loss resolution? Secondly, does the final anode sensitivity variation truly fall below 1% σ ? In other words, to what extent can one be confident in the efficacy of the PMT calibration as demonstrated? The first question will be answered in Section 6.4. The second will be investigated in this section.

The PMT anode sensitivity calibration presented in this chapter demonstrates a high-quality and proven method for matching PMT anode sensitivities in a detector with a large number of PMTs, evidenced by a 40-80 times reduction in anode sensitivity variation. However, the question of repeatability arises. To address this, an additional measurement was conducted for each PMT. After calibrating all PMTs in an array, the LED was repositioned

at the start of the array, and the anode sensitivity was remeasured at 800 V. This process, repeated for every PMT, allows for the comparison of anode sensitivity behavior over time, highlighting uncertainties due to variations in humidity, temperature, PMT warm-up periods, or LED positioning. The uncertainty derived from these comparisons is currently an estimate, as further trials are necessary for precise quantification. Moreover, this study does not identify specific sources of error but is crucial for quickly evaluating repeatability within a limited timeframe. A comparison of the original 800 V anode sensitivity and the repeated measurement is shown in Figure 5.16, which suggests good agreement. However, there are outliers in this data that raise concerns for the repeatability extended to a longer time period. The following will address potential sources of error and how they could impact the validity of the repeat measurement and calibration as a whole.

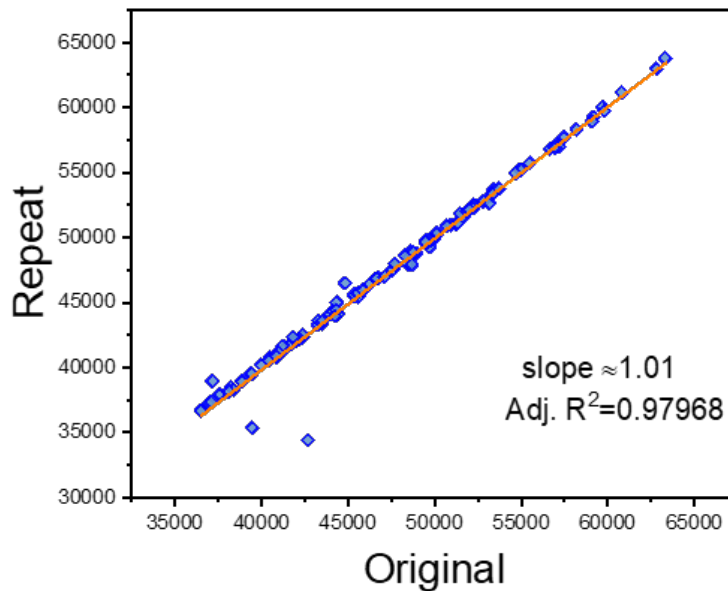


Figure 5.16: Comparison between the original anode sensitivities recorded for each PMT at 800 V in the PMT Gain Correction Stand and the repeat of that measurement after calibration.

A significant leak in the Argon supply line was discovered after completing the calibration and 800 V repeat measurement for seven out of eight short (non-dispersive coordinate) PMT

arrays. Consequently, for 35 PMTs, the gas between the LED and PMT window was an unknown mixture of Argon and air at approximately 720 Torr. After fixing the leak, the PMT Gain Correction Stand was filled with approximately 720 Torr of Argon. As a result, all of the PMTs discharged during the subsequent ramp-up. According to the Paschen curves in Figure 5.17, the pressure times breakdown distance pd is about twice as large for Argon compared to air at a breakdown voltage of 800 V, making discharges twice as likely for Argon in this pressure and voltage range.

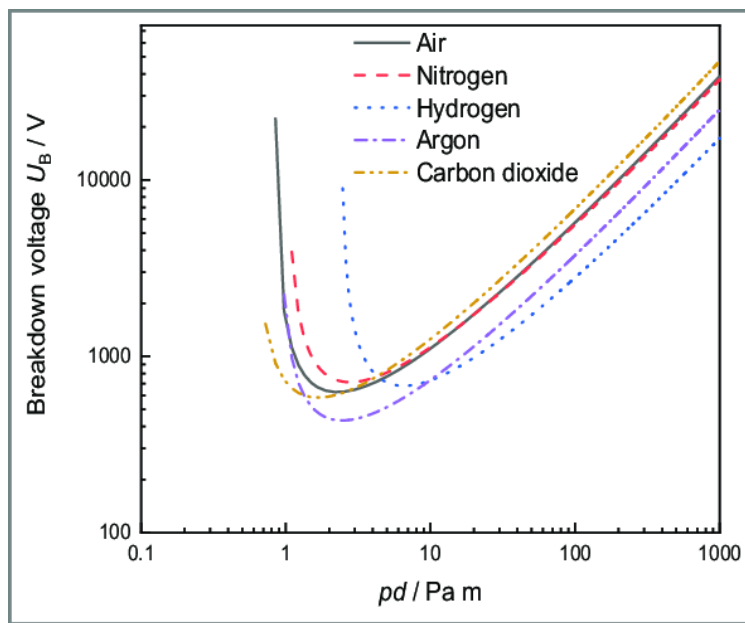


Figure 5.17: Paschen curves for common gases [?].

Nonetheless, the gain correction stand was able to operate in air at atmospheric pressure and deliver the same results, as evidenced by Figure 5.18. Applying a substantial amount of insulating varnish to the voltage-divider PCB increased the discharge threshold such that two PMTs could be biased to their calibration voltage in 800 Torr of Argon. They were compared in four different environments: the Ar/air mixture from the initial setup with leaking Argon, 800 Torr Argon, and atmospheric air. The PMTs were tested in air twice, once with the original LED connection and then with an improved LED connection. The

anode sensitivity was not significantly influenced by the gas it was measured in, so it was decided that the calibration could be continued in atmospheric air without recalibrating the first 35 PMTs. To account for the difference in LED intensity, the amplitude of the LED power was lowered appropriately to match the anode sensitivity measured previously.

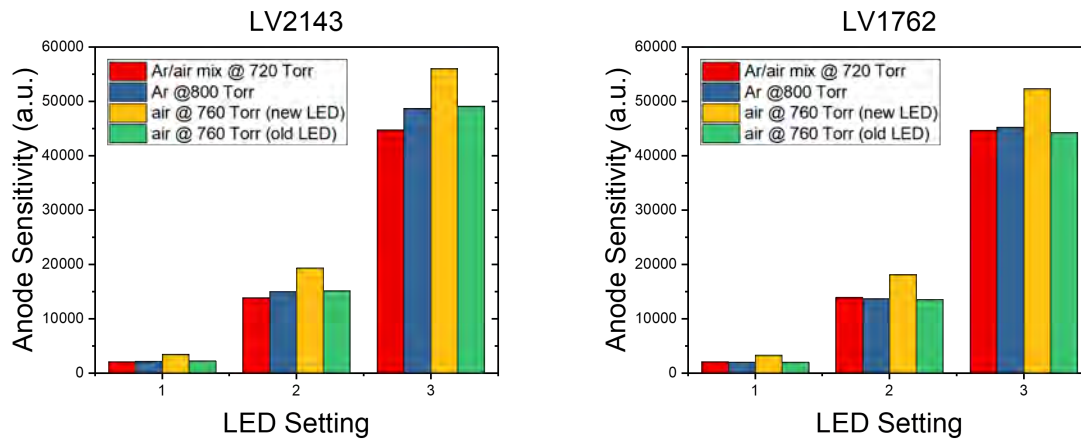


Figure 5.18: Anode sensitivity for two PMTs at each LED intensity setting. Measured in four different environments (listed in order left to right): initial Ar/air mixture at 720 Torr, Ar at 800 Torr, and air at atmosphere with two different LED connections.

Unfortunately, discharges on the voltage-divider PCBs have lasting effects. For the PMT bases that sparked, the QDC channel connected to them was destroyed. Additionally, testing the breakdown voltage in Argon put stress on surrounding decoupling capacitors in the decoupler crate. These capacitors became prone to breaking down and allowing large fluxes of current through to the QDC input, effectively burning up the input stage for that channel. This posed problems for continuing the calibration with the ELOSS channel mapping. Going forward, each PMT was characterized and calibrated using one of five QDC channels instead of the designated channel laid out in the ELOSS channel mapping. Therefore, for a majority of the PMTs, the anode sensitivity calibration does not include fluctuations due to their connected readouts, which is a definite source of error. However, the fluctuations from the passive elements in readout circuits are likely to only make up a minuscule amount of the

overall signal.

Replacing Argon with air might not have had an effect in terms of light attenuation due to O₂ absorption, but other environmental factors do arise. Displacing the air originally inside the calibration stand and filling it with pure Argon is a convenient method for controlling the temperature and humidity, which typically impacts PMT performance. Without this control, the uncertainty associated with temperature and humidity-dependent PMT performance is reintroduced.

The last major source of uncertainty is the LED positioning with respect to the center of each PMT. A study was conducted to quantify this uncertainty and is partially summarized in Figure 5.19. The goal was to identify any discrepancies in the LED positioning with respect to the center of the PMT's photocathode. Assuming a uniform photocathode in terms of quantum efficiency, the peak PMT response should occur when the LED is directly above the photocathode center point, corresponding to the largest solid angle coverage. The idea was to scan the LED across the PMT surface to find the actual PMT center and determine the offset from the PMT center coded into the Arduino-controlled motor driver logic. For each PMT, the LED was moved to the PMT position configured in the Arduino code and then moved back -6 mm. Starting from this point, measurements were taken every 2 mm until reaching 6 mm. Fitting the data for each PMT scan with a quadratic function, the peak can be extracted, as indicated in Figure 5.19. A puzzling trend appears from this figure. The distance the LED moves to go from PMT to PMT is supposed to be constant (6 cm), meaning any offset should be consistent for all five PMTs, but this is not the case. This inconsistency suggests that the LED position is actually only accurate within ± 1 mm. The average offset of the PMTs was -1.84 mm, so by increasing the LED positioning by 1.84 mm, the peak PMT response should be centered at the new LED position. A second test

indicated that the new offset was -0.44 ± 0.79 mm. Comparing the percent difference between the PMT responses measured at 0 mm offset and the peak PMT response offsets showed less than 2.5% deviation for all PMTs and nearly 0% for two out of the five. As a result, there is likely anode sensitivity variation not being accounted for, especially when considering PMTs in different locations on the PCB.

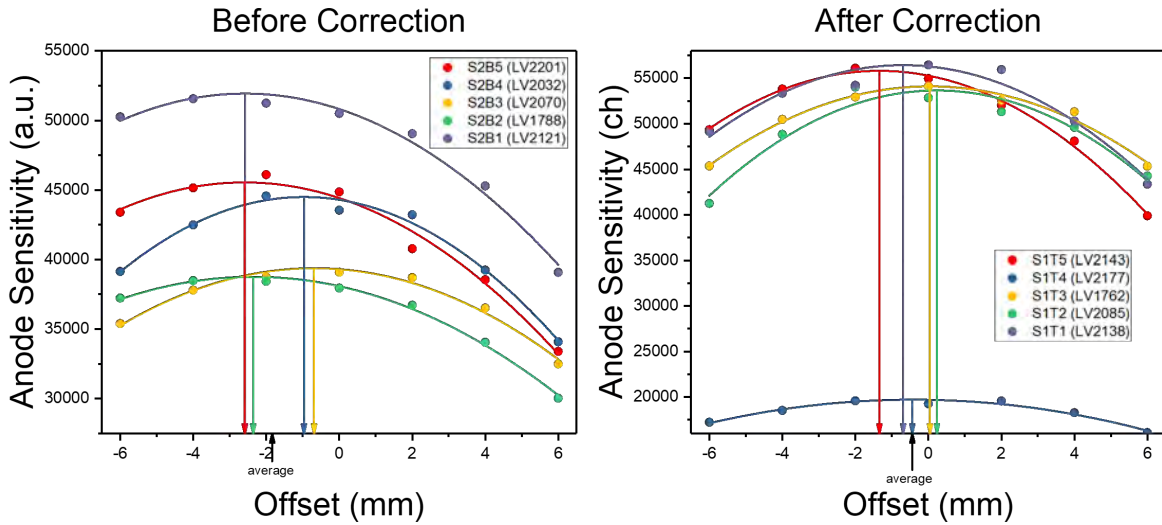


Figure 5.19: Left: Anode sensitivity as a function of the positional offset from the targeted position detailed in the Arduino code. Right: anode sensitivity as a function of offset after adjusting the starting position of the LED to account for offset in the left figure.

Chapter 6. Optimization and Further Studies with a Deep Neural Network

6.1 Introduction

The previous chapter briefly introduced the notion of position-dependent light collection efficiency in large-area gaseous scintillation detectors, noting its adverse effect on energy resolution. It was established that an energy loss correction factor, which considers light collection efficiency as a function of particle position, can mitigate this position dependence and substantially enhance energy loss resolution, provided the optical readout sensitivity is homogeneous. From the results of the PMT anode sensitivity calibration detailed in Chapter 5, the ELOSS optical readout sensitivity can be considered homogeneous to within approximately 1%.

This chapter will now examine the correlation between light collection efficiency and the position of charged particles within the ELOSS sensitive volume, utilizing data from GEANT4 simulations. The primary data recorded in these studies is the number of photons detected by each PMT per event. The GEANT4 output structure used in these studies quantifies light levels in photons. Therefore, the term “light collection efficiency” can be more accurately referred to as “photon collection efficiency”.

6.2 Photon collection efficiency and photon-counting resolution

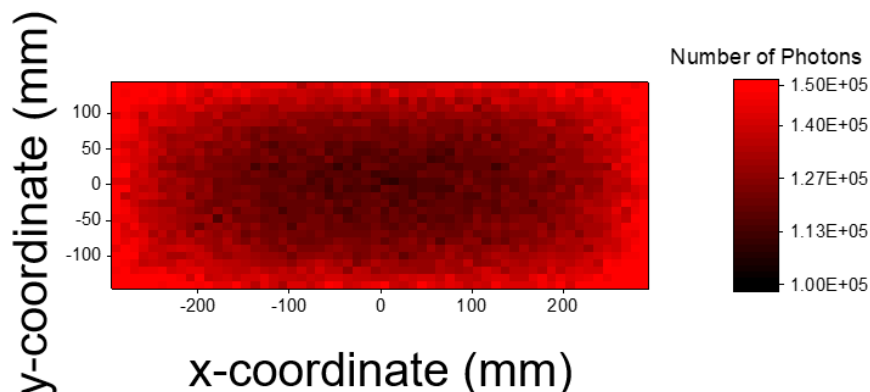


Figure 6.1: GEANT4 generated map of the average number of photons recorded by the ELOSS optical readout as a function of the position (X,Y) of $^{80}\text{Se}^{34+}$ particle impinging on the detector area.

To illustrate the variation in photon collection efficiency with the incident particle position, Figure 6.1 was generated using data obtained from a GEANT4 simulation of about 4000 $^{80}\text{Se}^{34+}$ particles with an initial energy of 140 MeV/u. In this simulation, a homogeneous irradiation of the entire active area of ELOSS was implemented by randomizing the origin of each particle within the detector area. That is

$$-150 \text{ mm} < x_0 < 150 \text{ mm}$$

$$-300 \text{ mm} < y_0 < 300 \text{ mm}.$$

The 300 mm \times 600 mm area is segmented into 10 mm \times 10 mm pixels to plot the average number of photons recorded by the ELOSS optical readout as a function of (x,y) position. The average number of photons collected per event per pixel is calculated using data from $^{80}\text{Se}^{34+}$ particles entering only through that pixel. By dividing the average number of photons in a pixel by the total number of scintillation photons produced, which is approximately

constant for every event, a two-dimensional map of photon collection efficiency as a function of a particle's impinging position.

As evidenced by Figure 6.1, the total number of photons collected by the optical readout increases as particles enter the detector closer to the perimeter of the effective area, despite the total scintillation being consistent for each event (13 ph/keV for approximately 100 MeV per sector). Scintillation originating near the perimeter of the effective area experiences a larger solid angle coverage by the PMT windows/photocathodes. PMTs in proximity to the scintillation source dominate the overall coverage due to the $1/r^2$ solid angle dependence. Conversely, the reduced collection efficiency of PMTs farther away has a minimal impact on the total photon collection efficiency.

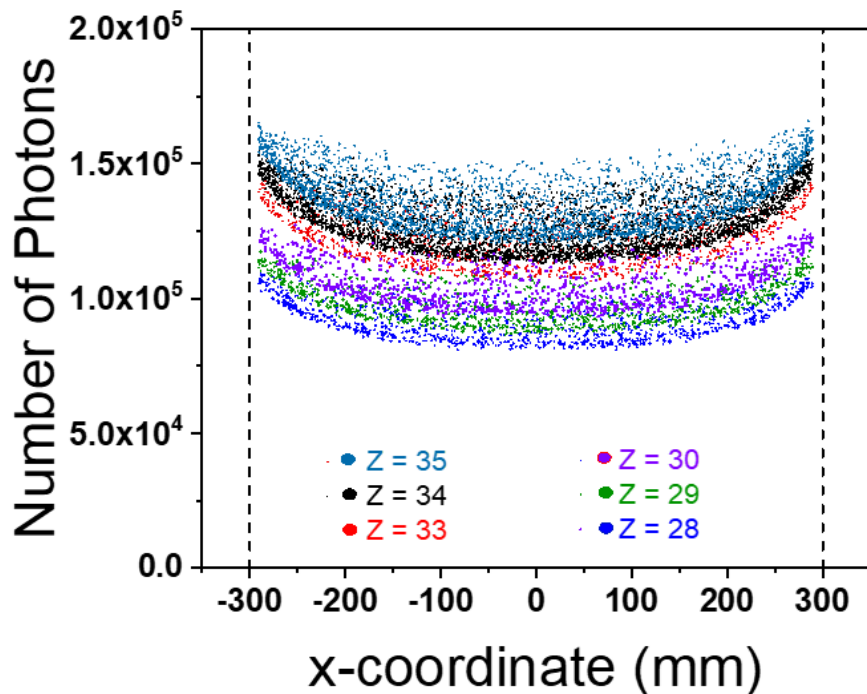


Figure 6.2: Number of photons detected by the ELOSS optical readout as a function of the position of the beam particles (with an energy of 140 MeV/u) along the x-coordinate (600 mm wide). A simulation was conducted for isotopes with atomic numbers of 28 to 35.

Figure 6.2 illustrates the number of photons collected by ELOSS as a function of the x-coordinate of the impinging particle for nine different isotopes. The isotopes simulated

range from $Z=28$ to $Z=35$, with three different masses (81, 82, and 83) selected for $Z=34$ and $Z=35$. Each simulation consisted of 1000 particles of the same isotope. A significant variation in the number of photons is observed as x reaches the outer limits of the detector area, consistent with Figure 6.1. When projected into a histogram of the y -axis, the different isotopes are indistinguishable, as shown in Figure 6.3.

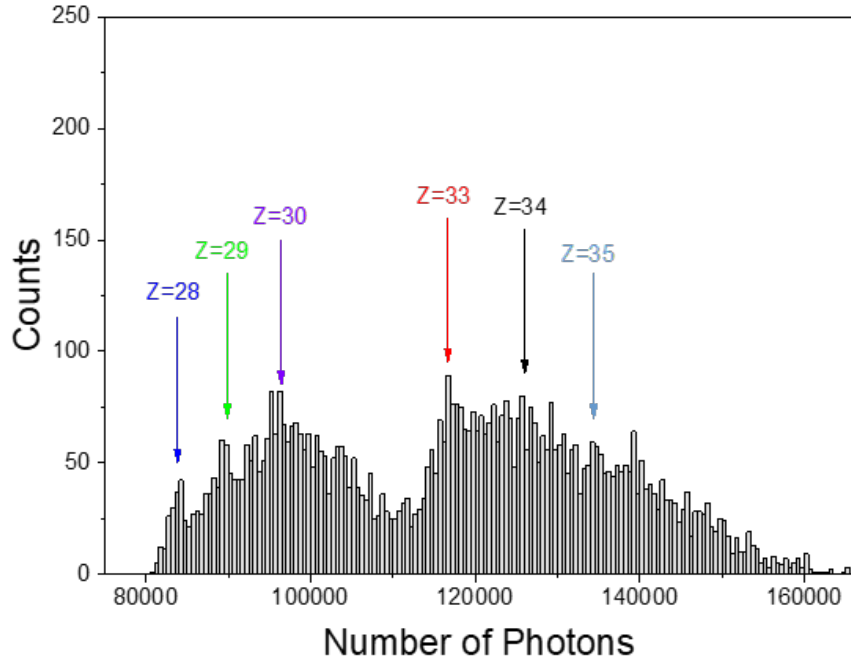


Figure 6.3: Number of photons detected by the ELOSS optical readout for beam particles with atomic numbers 28 to 35 and 140 MeV/u. The photon count peaks representing each Z are indistinguishable.

Correcting the variation in photon collection efficiency requires the computation of a multiplicative factor $C(x, y)$. This factor is essentially the inverse of the two-dimensional photon collection efficiency, taking into account the (x, y) position of the incident charged particle and the geometry of the optical readout. By multiplying $C(x, y)$ by the measured number of scintillation photons $L_M(x, y, Z)$, a light collection consistent with a uniform detector response is achieved, given by $L(Z)$.

$$L(Z) = L_M(x, y, Z) \cdot C(x, y) \quad (6.1)$$

To determine $C(x, y)$, the photon collection map $M(x, y, Z)$ corresponding to a single isotope needs to be normalized to its lowest value (measured at the center of the effective area). This results in a photon collection map independent of the incident particles' Z , yielding the photon collection efficiency map $\tilde{M}(x, y)$. The two-dimensional map $\tilde{M}(x, y)$ is fitted with an analytical function that accurately describes the photon collection efficiency variation as a function of position. After a series of trials testing different functions (mostly polynomial), a 9th degree polynomial was chosen for its superior adjusted R-square of 0.998. The fitting function is presented below

$$\tilde{M}(x, y) = \sum_{i=0}^9 \sum_{j=0}^9 A_{i,j} x^i y^j \quad (6.2)$$

where the matrix $A_{i,j}$ contains all of the coefficients for the 9th degree polynomial equation in the two variables (x, y) . The correction factor $C(x, y)$ is the just the multiplicative inverse of $\tilde{M}(x, y)$ expressed as:

$$C(x, y) = \left(\sum_{i=0}^9 \sum_{j=0}^9 A_{i,j} x^i y^j \right)^{-1} \quad (6.3)$$

The magnitude of $C(x, y)$ is less than or equal to unity, decreasing as the distance between particle position and the detector center increase.

The accuracy of the energy loss correction is contingent upon two main factors: the quality of data used to map the photon collection efficiency $\tilde{M}(x, y)$ and the uncertainty in the x and y position inputs. By using detailed detector geometry, accurate physics models,

and a large number of data points, high-quality data can be obtained from GEANT4. However, mapping the photon collection efficiency of ELOSS through a real beam experiment introduces various uncertainties, such as beam spot size, beam position accuracy, and the resolution of the optical readout. The last of these uncertainties can be included in the analysis of GEANT output data to minimize the discrepancy between simulated performance and actual results.

The second component, x and y uncertainty, motivates the rest of this chapter. The S800 focal plane drift chambers can provide position arguments for $C(x, y)$ to correct the energy loss measured in ELOSS. Despite being capable of about 0.5 mm σ resolution in x and y , extrapolating the position across the large distance between the drift chambers and ELOSS may introduce significant variation, thereby increasing the uncertainty in $C(x, y)$. In response, a self-contained method for extracting particle position from the light distribution measured in ELOSS is proposed in the next section.

6.3 Deep Neural Network

Data collected by the ELOSS optical readout is processed through a machine learning algorithm to determine the impinging particle position. With this position, the method described in the previous section can be applied to adjust the total number of detected photons (GEANT4) or energy loss (real experiment). Light distributions generated for each event are fed into an algorithm developed and implemented using Keras [53, 54]. The Keras package is a high-level open-source abstraction library that works on top of the low-level TensorFlow [55] computation engine.

The machine learning model developed for ELOSS position reconstruction is a fully con-

nected Deep Neural Network (DNN) with 9 total layers. The neuron architecture follows a 30-64-128-64-32-16-8-4-2 distribution, with 30 neurons filling the input layer and 2 neurons in the output layer. The NN algorithm processes one sector at a time, using the 30 PMT signals of a sector as inputs to predict the x and y position outputs. Normalizing the 30 inputs to their sum ensures consistent position reconstruction for each sector, independent of the total amount of light generated in individual sectors. The network has 21,350 trainable parameters, including weights and biases, with each hidden layer node using a rectified linear unit (ReLU) as its activation function.

Numerous trials were performed with the intent of reaching the best possible spatial resolution in x and y by optimizing the architecture of the hidden layers where most of the data processing and modeling takes place. The model uses a momentum-based gradient descent (Adam for "Adaptive Moment Estimation") [56], which incorporates adaptive learning rates and momentum, with the mean squared error serving as the loss function. The optimization of the neural network started with a model consisting of 4-5 layers and about 5000-7000 trainable parameters, which yielded a spatial resolution around 1.5 mm. Adding more layers, and consequently more trainable parameters, further improved the position resolution. A deeper neural network with 5-6 layers and about 18,000-20,000 trainable parameters resulted in a 1 mm localization capability. Increasing the number of layers to 9 and trainable parameters to 21,350 resulted in the best position resolution (about 0.7 mm σ). Increasing the number of layers or neurons past this did not significantly enhance the efficiency or performance of the model.

Training the chosen neural network took approximately 12,000 data points from GEANT4 simulations of isotopes with Z ranging from 28 to 35. This set of data points was randomly sampled in batches of 200 during the training cycle. A small set of about 1500 data points

was set aside for validating and optimizing the training. The validation procedure avoids over-fitting through the implementation of an early stop monitor. Another 1500 data points were also set aside, and never seen by the model during training, as they were reserved exclusively for testing the model. By normalizing the PMT photon count inputs into the DNN, any Z dependence is removed. The position reconstruction is therefore valid for any Z and supports a wide range of events energy depositions in the effective volume.

The DNN algorithm is applied to each sector separately to generate four (x, y) position predictions. For straight particle tracks, combining the predictions from all four sectors yields a single point representative of where the particle impacted the entrance pressure window. For particles entering at an angle, a trajectory can be reconstructed.

6.4 Results

6.4.1 Position reconstruction

The data generated by GEANT4 simulations and used in Figure 6.2, was also used to evaluate the DNN algorithm's performance in computing particle positions (x, y) and tracks (angle) based on the light distribution captured by the ELOSS optical readout.

A correlation analysis between the GEANT4 simulation's input particle position and the DNN algorithm's predicted position is illustrated in Figure 6.4 panel a). The graph plots the DNN's y -coordinate prediction on the Y-axis and the simulation's y -coordinate input on the X-axis. The same correlation is produced when comparing the x -coordinate as well. The input position coordinates are integers that range from -300 mm to 300 mm and the values estimated by the DNN are computed as the average of all four sector predictions. The input

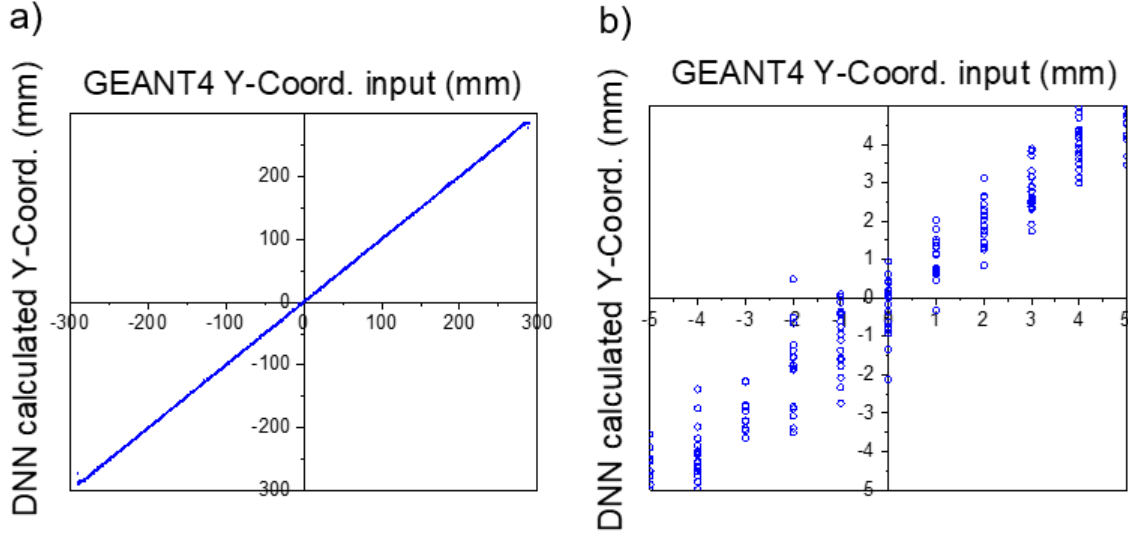


Figure 6.4: Panel a) An analysis of the correlation between the y-coordinate position of the beam particles used as input for GEANT4 and the values estimated by the DNN algorithm processing the simulation data outputs. Panel b) show a close up section of the correlation graph at the center of the detector.

and estimated positions show superb agreement within ± 290 mm in y .

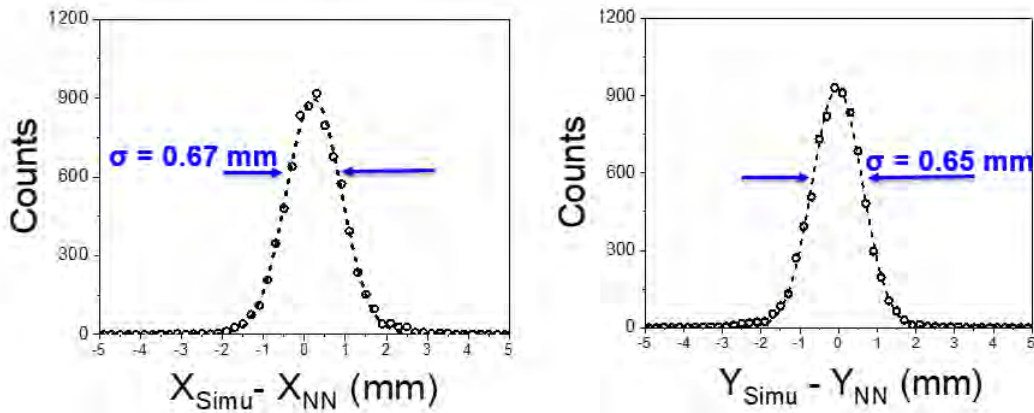


Figure 6.5: Position resolution (calculated for the X axis on the left graph and the Y axis on the right one) provided by the DNN by processing the light distribution recorded by the PMTs.

Figure 6.4 panel b) is a close-up view (5 mm x 5 mm window) of the plot origin in panel a). With this perspective, the non-zero spatial resolution for predicted positions can be observed. The reconstructed position resolution provided by the DNN algorithm is calculated by the difference between the GEANT4 input position (X_{Simu}, Y_{Simu}) and the algorithm's

prediction (X_{NN}, Y_{NN}) . The resulting position resolution is shown in Figure 6.5.

Spatial resolution remains constant at about 0.7 mm σ across the entire ELOSS effective area. In addition, this position reconstruction approach proves to be consistent in the atomic number range 28 to 35, with no dependence on the total number of photons generated in ELOSS.

6.4.2 Energy loss after correction from position reconstruction

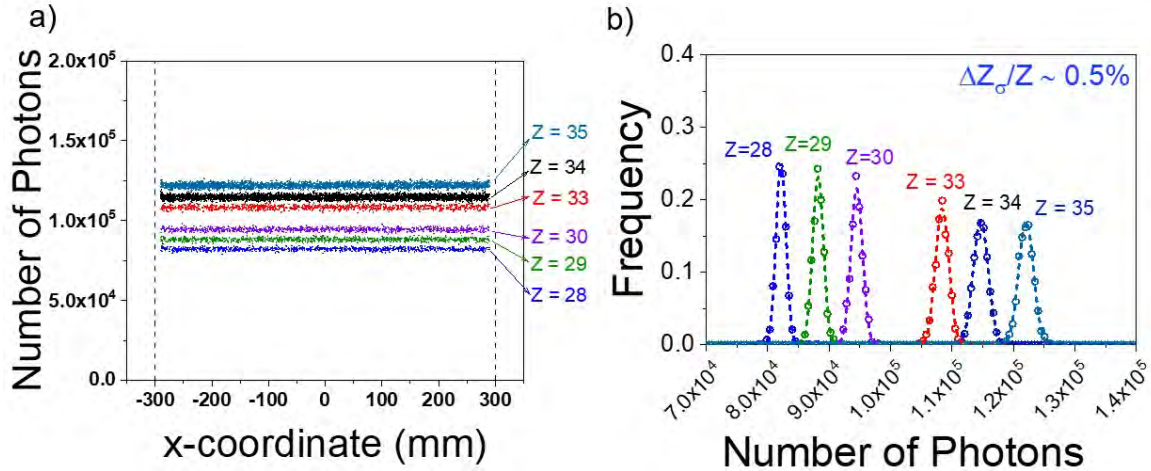


Figure 6.6: Panel a) shows same data as Figure ?? corrected for the variation of the photon collection efficiency. Panel b) PID plot obtained from the projection of panel a) along the y-axis. All the simulated isotope are well separated - $\Delta Z_{\sigma}/Z = 0.5\%$.

Ultimately, the position estimated by the DNN algorithm is used to determine the correction factor needed to compensate for the position-dependent photon collection efficiency. Figure 6.6 shows the same graph as Figure 6.3, but with the correction factor applied to each isotope, such that the number of photons detected by the ELOSS optical readout is consistent regardless of position. Figure 6.6 panel b) is the projection of panel a)'s Y-axis, effectively creating a PID plot for the isotopes given. The X-axis in panel b) is given in number of photons, but is directly proportional to energy loss ΔE . Thus, an energy resolution

can be extracted from here: $\Delta E/E = 1\% \sigma$. As detailed in Chapter 1, the Z -resolution is about half $\Delta E/E$, resulting in $\Delta Z/Z \sim 0.5\% \sigma$

6.4.3 Tracking capabilities (angular)

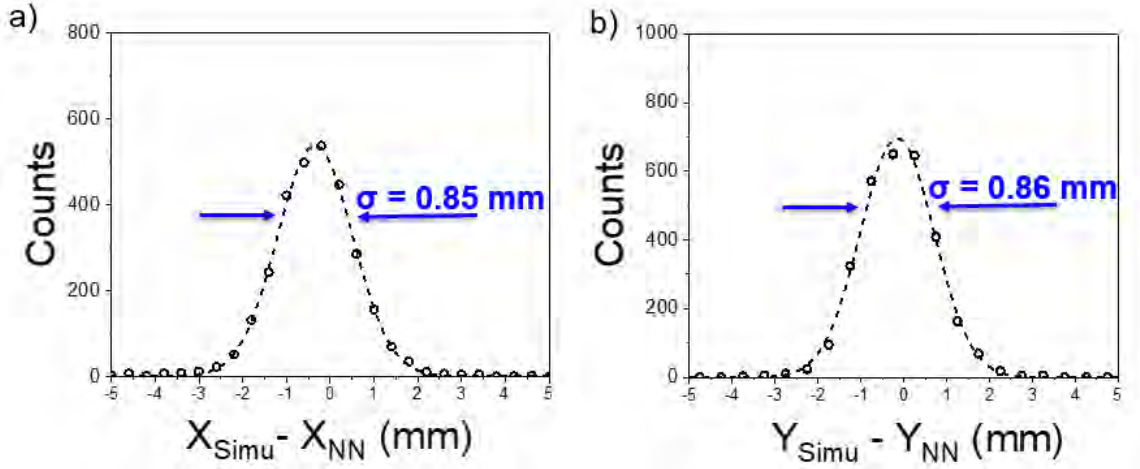


Figure 6.7: Same as Figure 6.5 but for particle tracks with a non-normal angle of impact with respect to the ELOSS entrance windows.

In the case the particles' tracks are not perpendicular to the ELOSS entrance window, the DNN algorithm can be used to calculate the position as an average estimate within each ELOSS sector, and thus also the trajectory of the particle across the full ELOSS volume (tracking). In this latter case, a linear fitting can be performed on the positions extracted from the four sectors of the ELOSS optical readout to calculate the incident angle of the particle on the entrance window. The position from a sector is a mean estimate over the entire sector, and it is subject to a greater amount of uncertainty compared to tracks that normally impinge on the ELOSS effective area, causing a slight degradation of the position resolution to approximately $0.85 \text{ mm } \sigma$ (see Figures 6.7), compared to the $0.7 \text{ mm } \sigma$ for normally impinging tracks. The intrinsic angular resolution provided by the DNN-based tracking method is of the order of 12 mrad (Figure 6.8), approaching the intrinsic resolution

of the more conventional drift chamber (of about a few mrad). The angular resolution is measured as the spread (σ) of the distribution computed from the difference between the angles of the particle trajectory generated in the Geant4 simulation (θ_{Simu}) and the one estimated by the DNN algorithm (θ_{NN}) after processing the ELOSS data.

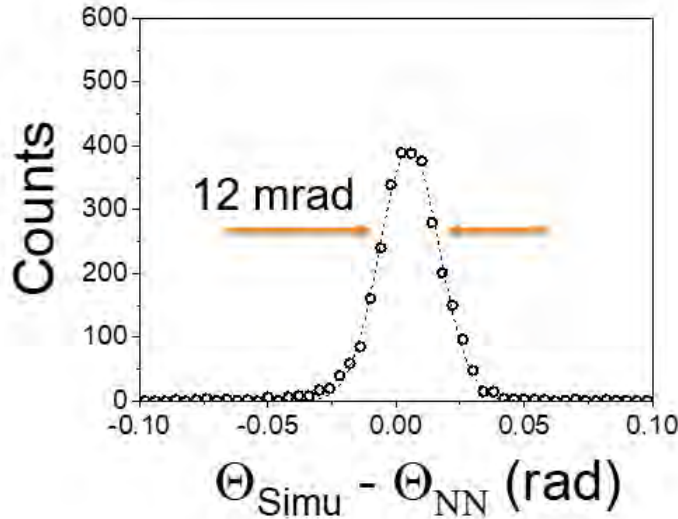


Figure 6.8: Intrinsic angular resolution obtained by tracking the trajectory of the particle in the ELOSS volume using the DNN algorithm applied to the data (light distributions) recorded in each sector of the ELOSS optical readout.

In spite of a slight degradation of localization capability, a similar PID capability was also obtained for trajectories impacting on the entrance windows at some angles ($\Delta Z_\sigma/Z \cong 0.5\%$).

6.4.4 Adding noise

There are several sources of noise that affect number of detected photons by the ELOSS PMTs, including individual PMTs and their high-voltage biases, interfaces like cables that serve as antennas, and intrinsic electronic noise within DAQ modules. The presence of noise can adversely affect the accuracy of localization capability, which in turn impacts

the resolution of PIDs. Simulated PMT light signals were supplemented with white noise generated by a Gaussian distribution whose amplitude and spread was proportional to the number of detected photons and progressively increased (up to 20%).

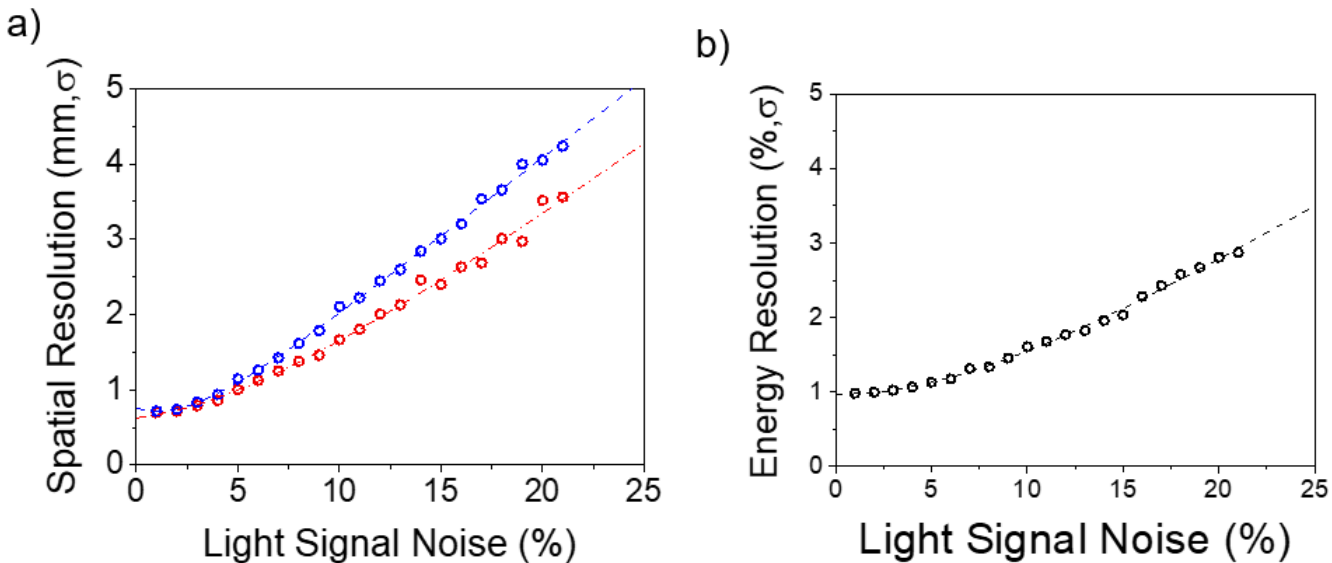


Figure 6.9: Degradation effects on localization capability (left graph) and on energy resolution (right graph) by a progressively increased noise level on the simulated light signals.

Figures 6.9 illustrate the variation in the performance of the localization capability (right graph) provided by the DNN algorithm, and the associated loss of energy resolution (left graph), as the noise is successively increased. Since the variation in photon collection efficiency is a smooth function of particle position (the map is approximated by a polynomial function), the propagated error in extracted energy resolution after position correction is less severe. Energy resolution below 1.5% (σ) can still be obtained at extremely high noise level of about 10% added to the light signal. As the Z resolution is half of the energy resolution provided by the detector system ($\Delta Z = \Delta E/2$, since $E=Z^2$), a good PID capability of about $\Delta Z/Z$ equal to 0.75 is still possible despite such high noise level. Notice that the data in Figures 6.9 are extracted from a DNN that was trained on a dataset with no noise added to it. By training on large datasets that include noisy signals (for example, recorded by an

actual detector and DAQ), the robustness and localization accuracy of DNN algorithms can be significantly improved.

Taking the light signal noise's impact on the energy resolution as reference, the PMT anode sensitivity variation can be considered acceptable within 2%. This coincides with the negligible energy resolution change with this level of light signal noise.

6.4.5 Adding PMT anode sensitivity

Adjusting the simulated PMT signals to account for differences in anode sensitivities is crucial for evaluating the DNN position reconstruction algorithm, the PMT anode sensitivity calibration, and assessing the overall performance of a more realistic detector. This process involves normalizing the anode sensitivities measured at various calibration stages to the average anode sensitivity at each stage, resulting in a multiplicative sensitivity variation factor for each PMT. The sensitivity-adjusted photon count for each PMT is then determined by multiplying this factor by the number of photons detected. This approach allows for the localization of specific sensitivity variations within the optical readout geometry, enabling certain regions of the effective area to contribute more or fewer detected photons, independent of the variable light collection efficiency previously discussed.

A sensitivity variation factor was calculated for each PMT based on anode sensitivities measured after the coarse gain correction, where all PMTs were supplied with 800 V, and after the fine-tuned gain correction, where all PMTs were supplied with their calibrated voltages. The photon counts, adjusted for the fine-tuned correction stage sensitivity, were fed into the NN to predict the particle position and compute $C(x, y)$ for each event. The total number of photons detected after applying $C(x, y)$ is shown in Figure 6.10. The original data comes from a simulation consisting of 3000 ^{59}Ni particles uniformly irradiating the effective

area of ELOSS with an energy of 140 MeV/u. “Not Corrected”, in Figure 6.10, corresponds to the total number of photons detected after applying $C(x, y)$, computed from an unaltered NN input. Comparing the performance between “Not Corrected” and “Fine-Tune Corrected” shows that the effect of including measured anode sensitivities at calibrated voltages is nearly unnoticeable. In contrast, ELOSS achieves almost 1.7 times worse energy loss resolution if stopping the anode sensitivity calibration after the coarse gain correction. Since the $\sigma_{\Delta E}$ needed for 3σ separation for Ni is about 2.36%, the coarse gain-corrected optical readout would be sufficient, but that is assuming otherwise simulation-like conditions. For example, the tolerable noise level is considerably reduced due to a higher anode sensitivity variation.

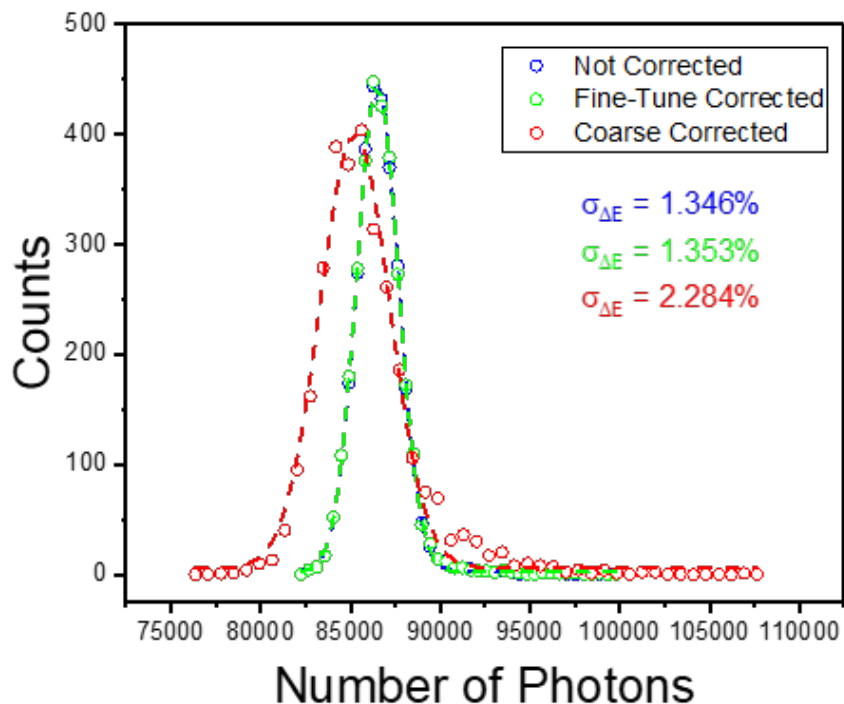


Figure 6.10: Total number of photons detected by ELOSS from a GEANT4 simulation of 3000 ^{59}Ni particles uniformly irradiating the effective area with an energy of 140 MeV/u. The photon counts for each PMT were adjusted based on the anode sensitivity of that PMT measured after coarse gain correction and after fine-tune gain correction.

Ultimately, adjusting the input photon counts to reflect the anode sensitivity across the entire PMT array shows the robustness of the this neural network-based position re-

construction and energy loss correction when using more realistic PMT signal variations. Additionally, the impact of the PMT anode sensitivity calibration is quantified. Calibrating by coarse gain corrections only, results in an energy loss resolution ($\frac{\delta(\Delta E)}{\Delta E}=2.284\% \sigma$) barely capable of 3σ separation in the $Z = 28$ atomic number range, while a fully calibrated readout is within $0.01\% \sigma$ of a perfectly uniform optical readout sensitivity.

6.4.6 Missing PMTs

In any multi-sampling optical readout system, it is essential to have a contingency plan for when photosensors malfunction, whether due to high noise, no signal, or signal saturation. With an effective plan, the detector can continue to operate normally or near-normally without requiring physical maintenance. Understanding the impact of these undesirable scenarios on detector performance is crucial before proposing a solution.

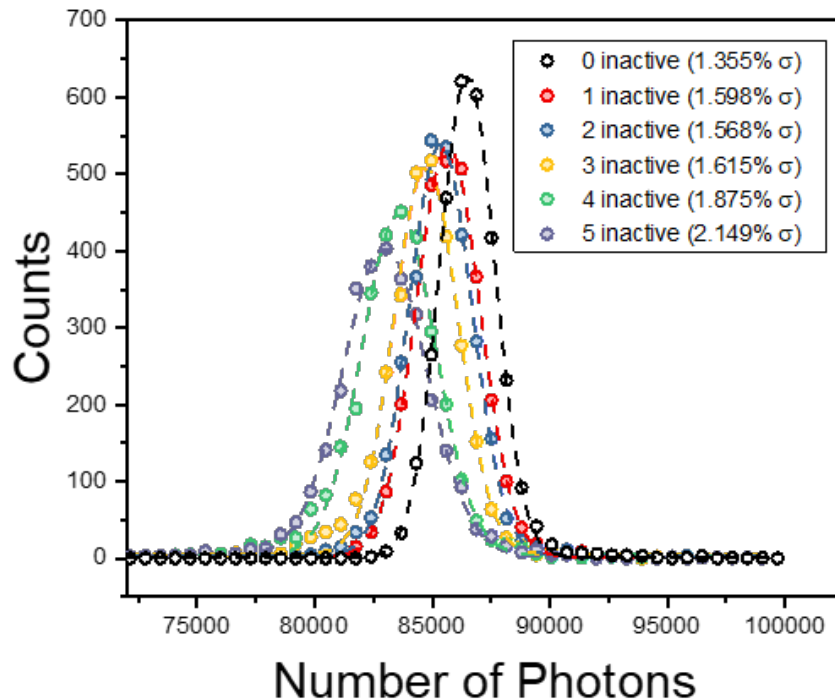


Figure 6.11: Total number of photons detected by ELOSS (same simulation as Figure 6.10). Photon counts were set to zero for a number of PMTs to simulate “inactive” PMTs.

Figure 6.11 illustrates the total number of photons detected with ELOSS when 0, 1, 2, 3, 4, or 5 PMTs fail to record any photons. For each scenario, the selected PMTs were randomly chosen from the full pool of 120 PMTs, regardless of their location. The PMTs were discarded for the entire 3000-event dataset in each test case. With only a few PMT signals removed, it becomes evident that the number of photons detected, and consequently the energy loss, depends on the number of active PMTs. This dependency can be detrimental to energy resolution, particularly if the number of functioning PMTs fluctuates during an experiment. Additionally, the energy resolution worsens as the number of inactive PMTs increases, but the change in resolution for each additional inactive PMT does not follow a clear pattern. This underscores the impact of the location of malfunctioning PMTs on energy resolution. The decrease in the number of photons for fewer functioning PMTs varies depending on whether the malfunctioning PMTs are located closer to the center of the effective area (larger impact) or in the corners (lesser impact).

There are several methods to mitigate this effect, most of which involve generating a replacement PMT signal through computational methods. Specifically, PMTs with no photon counts are identified, and their recorded number of photons (zero) is replaced with an estimated photon count to recover some of the position reconstruction accuracy and overall energy loss signal. The number of detected photons can be estimated at any location in the optical readout by taking the average of photon counts in neighboring PMTs. This approach will always underestimate signals for PMTs located at a maximum with respect to the light spectrum and overestimate the number of photons at minimums of the light distribution. However, computational signal recovery enables performance comparable to that of a fully functional optical readout in some cases, as shown in Figure 6.12.

With further studies, it is possible to develop a computational signal recovery method

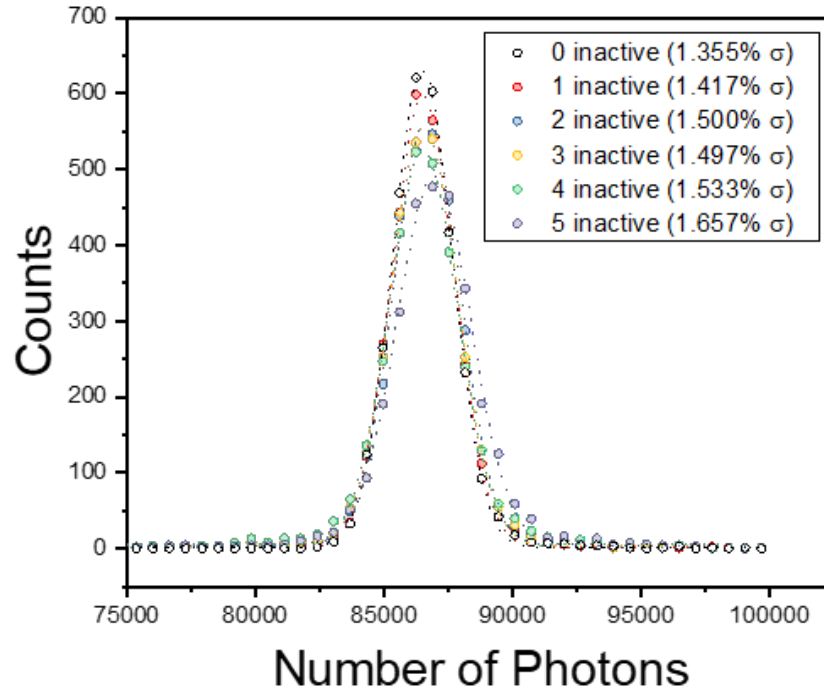


Figure 6.12: Same as Figure 6.11, but the inactive PMT signals were replaced with the average of its neighbors before being input to the neural network algorithm.

that can achieve nearly the same performance as a fully functional ELOSS, even with several PMTs inactive. These alternative methods could use a projection of the light distribution collected by the opposite side's PMT array or a curve fitting routine combined with interpolation/extrapolation, for example.

Chapter 7. Experimental Results

7.1 Experiment 1

Achieving high light collection efficiency in large-area gaseous scintillation detectors is challenging and costly. Consequently, testing a detector like ELOSS requires more energy deposition within the effective volume to generate sufficient scintillation. This is compared to detectors that collect drifted charges rather than light. The development of this entirely novel detector demands testing practices beyond conventional check source verification, which typically only deposit a few MeV. While the LEDs mounted inside the detector between each PMT can verify PMT functionality in a binary sense (signal/no signal), it cannot accurately assess the detector's performance characteristics. Therefore, an ion beam comparable to those used in the S800 is the only viable option for evaluating the overall performance and functionality of the ELOSS detector.

The FRIB Experiment 22507 intended to test ELOSS with a fast ion beam for the first time. The fully constructed detector had only been tested using the internal LEDs to this point, offering minimal information about its performance. It is important to note that this test was performed in July of 2023, several months before the neural network position reconstruction was introduced and the fine tune gain correction was implemented.

A ^{36}Ar beam at about 140 MeV/u was delivered to ELOSS, stationed inside the FRIB Transfer Hall, with a controllable intensity ranging from 10^3 to 10^7 pps available. ELOSS was positioned 38" from dipole BTS13:D2169 shown in Figure 7.1, directly in line with the future beamline feeding into the S2 vault. A 36" beam pipe extension left less than 2" (5 cm)

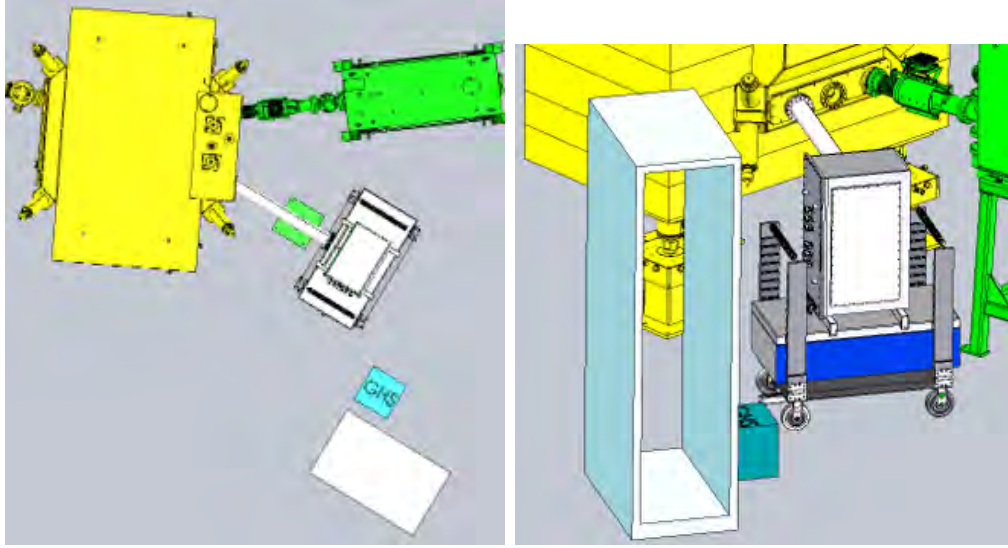


Figure 7.1: Drawings of the E22507 location and setup with the ELOSS detector, movable table, and representations of the electronics rack and GHS. ELOSS is positioned 38" downstream of dipole BTS13:D2169, centered with the future S2 vault beamline.

of air between the beam outlet of the dipole magnet and the ELOSS pressure window. The beam pipe was capped with an ISO100 aluminum blank that has a 1" diameter bore milled out in the center leaving 1 mm of aluminum separating the vacuum of the beam pipe and air. By milling out only a bore 1" in diameter, delivery of a beam with minimal momentum spread, while safely interfacing with the beam line vacuum was achieved. An aluminum blankoff was fabricated to stop the beam exiting ELOSS and took the place of the ELOSS exit window.

ELOSS was continuously flushed with CF₄ for over one week to replace all residual air inside the detector with 808 Torr of CF₄ gas. CF₄ is known for being a good photon emitter due to its broad spectral range from the far UV (peak around 160 nm) to the visible [57]. The total photon yield in the 150-220 nm range is about 242 ± 60 at 0.75 atm. In comparison, this is about 0.93% of Xenon's primary scintillation yield in the same spectral range [25]. CF₄ was chosen over Xenon in this experiment because it is several times cheaper, readily available, and the Xenon Recovery System was still being tested. Simply put, it was too

risky to fill ELOSS with Xenon at this time because the potential for losing a substantial amount of Xenon was too high.

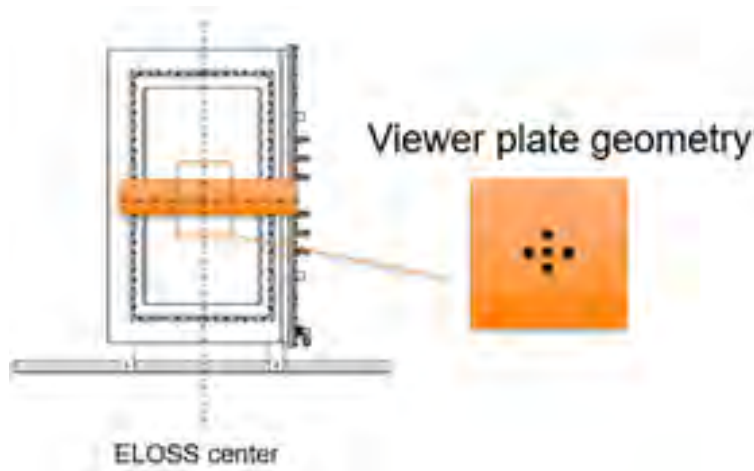


Figure 7.2: Schematic drawing of viewer plate installed on the entrance window of ELOSS. Viewer plate has a cross pattern of fiducials with 1 cm separation center-to-center.

As part of measuring the energy loss as a function of the beam position, a small beam profile (<10 mm) at the entrance window along with a well-defined x and y -position about the effective detector area is desired. A phosphor-coated viewer plate with fiducials marking the center cross of the plate was made to view the beam size and position in the coordinate system of the detector's effective area. Installing the viewer plate so the center fiducial exactly matches the center of the effective area, provides the ability to map the coordinate system of the beam using the Viola software [?] to the detector coordinate system.

The Alignment Group assisted in correcting the angular offset in each coordinate plane of the detector face with respect to the beam path. With minor adjustments to the moving table, the detector was aligned perpendicular to the beam path and centered in the x -direction within ± 1 mm.

The ELOSS Moving Table in Figure 7.3 was designed to move ELOSS in the x and y -axis to effectively scan the beam over the 30 cm (x) x 60 cm (y) active area of the detector.



Figure 7.3: ELOSS Moving Table consisting of a pneumatic cylinder controlled scissor-lift for vertical motion and a motorized linear actuator mounted on the bottom of the truck platform with the wheels controlled the horizontal motion.

Travel in the x -direction is 36 cm while travel in the y -direction is nearly 46 cm, therefore, the full width can be scanned and over 75% of the height can be scanned. The estimated coverage in x and y should be enough to accurately extrapolate the rest of the energy loss in the y -direction.

The ELOSS Moving Table also has the ability to align the center of ELOSSs effective area to the center of the beam spot minimizing the error associated with correcting data offline to the beam offset. Then, by making both the horizontal and vertical motion capable of being controlled remotely, corrections to the position could be made during beam tuning without having to stop and enter the Transfer Hall. The same goes for scanning the active area of ELOSS for position-dependent energy loss measurements, which maximizes the usable beam time.

The horizontal motion of the ELOSS Moving Table is based on a motorized linear actuator mounted on the bottom of the platform truck that is coupled with a bracket bolted to a long

piece of unistrut that is anchored to the Transfer Hall floor. The bracket is stationary with respect to the beamline in every direction, so movement between the actuator and bracket translates into the horizontal motion of the ELOSS Moving Table. The swivel casters of the platform truck are replaced with rigid casters to remove the extra degree of freedom and ensure all of the force provided by the actuator assembly is applied to the x -axis only.

The linear actuator is a Festo drive with a stepper motor. The actuator has a lead screw pitch of 12 mm and is controlled by a Geobrick motor controller capable of generating 6400 micro steps per revolution meaning the theoretical minimum position resolution of the horizontal motion is about $0.0019 \text{ mm}/\mu\text{step}$. It is impossible to achieve this unless the coefficient of friction between the wheels and the floor, wheels and axis, etc. is 0. An unknown fraction of the displacement is lost because of friction, which can be roughly estimated to be $1/12$ from a typical position accuracy within 1 mm for one revolution.

The BIM department assisted in establishing a GUI for controlling the actuator motor from the DataU through an EXP controls network connection given to the Geobrick. The stepsize recommended for moving the table was 1 mm and was accurate to the human eye.

120 psi compressed air fills a pneumatic cylinder to raise the platform ELOSS sits on. Remote controlled valves control the input and exhaust of the cylinder to regulate the vertical position of the detector with the help of a string potentiometer for position read back. Attached to the sides of the platform truck that the scissor lift sits on are custom ratchet arms for precision vertical positioning. With the ratchet arms, ELOSS can be positioned vertically in 7 different heights. Each height has a cleat for which the lift platform sits in to precisely and consistently control the height.

There were several lessons to be learned from this test that directly contributed to the improvement of the detector and the advancement of the ELOSS concept. First, it was clear

that the optical readout was not sensitive enough to detect the little amount of light generated in CF4. Throughout the experiment, the QDC output remained 0 for every PMT except when testing with the internal LEDs. Because of the response due to the LEDs, the PMTs were clearly working. This led to the conclusion that not enough light was generated to get over the noise threshold of the PMTs. The number of photons generated on average in one sector was about 34,485 according to calculations supported by a SRIM simulation after the test. With an estimated photon collection efficiency of 10% and the total number of photons divided equally among the 30 PMTs in a sector, 115 photons can be expected to reach a PMT on average. Taking the quantum efficiency to be 27% for the CF4 spectrum (150-220 nm), 31 photoelectrons are expected, which considering the noise floor was computed to be equivalent to around 100 photoelectrons for this setup, that was not going to cut it.

In an effort to recover scintillation, an attempt at operating ELOSS in stimulated electroluminescence mode was made, but no significant light response was observed before the foils sparked. Ultimately, this led to the realization that much more needed to be learned about the detector. In between this test and the next beam test one year later, a significant effort was put forth to improve PMT and DAQ channel sensitivity, produce/collect more scintillation, observe stimulated electroluminescence, better understand the DAQ triggering system and input parameters, and develop accurate models of the detector in GEANT4 and the optical readout response in LTspice.

7.2 Experiment 2

7.2.1 Description

FRIB Experiment 23508, conducted in July 2024, marked the second fast-beam test of the ELOSS detector, conducted at the same location as Experiment 22507. The objective was to assess the impact of modifications made to the detector over the past year and to evaluate its performance as initially intended during the 2023 beam test. All modifications aimed to increase the signal-to-noise ratio of the ELOSS optical readout. With a significant increase in the signal-to-noise ratio, it was anticipated that the DAQ would trigger on the higher amplitude signals, enabling the detector to function as intended. This improvement aimed to enhance the detection efficiency to a level suitable for PID, i.e. not 0%.

The signal-to-noise ratio can be improved through two primary methods. The first involves increasing the number of photons generated within the detector and collected by PMTs. The second method entails elevating the optical readout's light sensitivity, effectively lowering the minimum detection limit (the number of photons required to surpass the noise threshold).

The first method was achieved through a greater energy transfer between incident beam particles and the scintillating gas. The energy loss per unit length, as described in Equation 2.6, increases with a higher projectile Z (assuming it is fully stripped) and a higher target electron density. The latter is dependent on the Z of the gas and its pressure.

A ^{82}Se beam was delivered to the ELOSS detector at approximately 140 MeV/u, and in the same intensity range as the first fast beam test. The completion of the gas handling system, including the Xenon Recovery System, facilitated the use of Xenon in the detector,

replacing CF4. This change resulted in an increased energy loss per unit length and capitalized on the approximately 100 times higher scintillation yield of Xenon [57][25]. Furthermore, Xenon takes advantage of the maximum quantum efficiency of the R8520-406 PMTs (30% at 175 nm).

The optimization of the optical readout sensitivity involved several modifications, including changes to the cables connecting the optical readout components, the implementation of a new decoupler box, and the adjustment of QDC gain jumpers. A significant aspect of this optimization was the minimization of signal loss, primarily caused by the 8 ft shielded ribbon cable connecting the decoupler box to the QDC modules. The mismatch in impedance between the QDC gain jumper ($50\ \Omega$) and the cable ($100\ \Omega$) introduced reflections, resulting in distorted signals. Although the charge was largely preserved, the amplitude of the distorted pulses was reduced to about two-thirds of the original, complicating signal amplitude-based triggering, particularly for signals near the noise level. This problem was resolved by using a short 1 ft flat ribbon cable, which minimized signal distortion and preserved amplitude.

The new decoupler crate, described in Section 4.4.2, was designed to increase the voltage drop across the drop-down resistor while minimizing reflections and providing flexible packaging for the decoupler circuits. This crate is compatible with conventional electronics racks, allowing the short ribbon cable to be eliminated by placing the two components adjacent to each other. Given that a PMT signal is a brief pulse of current, its amplitude is directly proportional to the resistance (R) in Ohm's law. By increasing the signal readout resistor of the decoupler circuits from $50\ \Omega$ to $1\ \text{k}\Omega$, a larger PMT signal could be obtained. However, the amplitude remained in the range of tens of millivolts, necessitating a change in the gain jumpers from 2 V to 0.3 V to utilize the full range, thereby lowering the minimum detectable number of equivalent photoelectrons.

7.2.2 Results

The experiment represented a significant advancement in the development of the ELOSS detector. For the first time, ELOSS was operated in an ionization chamber mode and successfully measured the ΔE of an FRIB isotope beam. An energy resolution of about 1.4% σ was measured for ^{82}Se at 140 MeV/u, which is comparable to the present S800 ionization chamber. Another notable milestone was achieved as this was the first instance of a Xenon-filled ELOSS being used in a beam test. ELOSS was successfully operated at 850 Torr of Xenon, maintained and purified over an extended period, and subsequently recaptured. Despite these accomplishments, the sensitivity to scintillation light was found to be significantly lower than expected. However, post-processing analysis of the ELOSS DAQ settings in cooperation with Mesytec identified issues in the PMT voltage-divider and signal pickup circuitry, for which a revised design for the optical readout circuitry has been proposed, which is anticipated to enhance light sensitivity by several factors.

In an effort to improve scintillation yield during the beam test, the electrode foils dividing ELOSS sectors were biased to create the electric field needed to stimulate electroluminescence. A bias of up to 3 kV was applied before discharges became dominant. The reduced electric field $\frac{E}{P}$ needed to produce secondary scintillation from elastic collisions with liberated electrons is at least $1 \text{ V cm}^{-1} \text{ Torr}^{-1}$ according to [58]. For 850 Torr Xenon and 4.75 cm gap between foils, a HV supply of 4 kV is necessary to stimulate electroluminescence. Regardless, even if secondary scintillation had occurred, the PMT signals were too weak to trigger the DAQ.

Surprisingly, the most intriguing results came from the charge readout from the foils. Starting at 50 V, a clear signal was observed on the oscilloscope, with signal quality improv-

ing at higher voltages until discharges dominated. Data from the multi-channel analyzer (MCA), presented in Figure 7.4, shows a plot of charge collection versus foil voltage, revealing two distinct charge collection regions dependent on the electric field: the recombination region and the ionization region. This suggests that ELOSS was close to producing secondary scintillation, since the plateau region of this graph was reached. Stimulated electroluminescence becomes noticeable after this plateau, but before the proportional region.

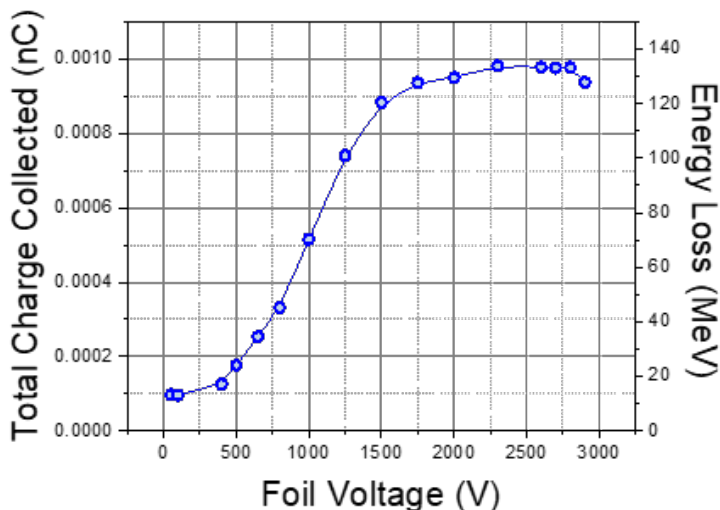


Figure 7.4: The total charge collected on the electrode foils/energy lost as a function of the voltage supplied to the foils.

The preamplifier connected to the charge readout electrode foils was not calibrated during the experiment. However, by replicating the setup in the detector lab, a conversion factor of $9.37\text{e-}7$ nC/ch was determined with an uncertainty of approximately 10%. The detection efficiency for an ion chamber reaches about 100% at the voltage where Figure 7.4 plateaus. It is at this point the absolute ΔE can be measured because the total charge induced on the electrode foils is directly proportional to the energy loss by the ionization potential of Xenon, which is 22 eV per electron-ion pair [9]. Therefore, the total energy lost in the effective volume of ELOSS was determined to be 130 MeV using the 2.7 kV foil bias.

Nevertheless, a quick SRIM calculation of the experimental setup and beam properties suggests that the energy loss in the effective volume of ELOSS should be around 495 MeV, which is about four times larger than the measured value. The Monte Carlo simulation uses the initial beam energy recorded at the fifth diagnostic box of ARIS. It takes into account the energy loss and straggling for the aluminum flange capping the beamline extension pipe, the air between the flange and the ELOSS pressure window, The pressure window (modeled as just kevlar) and the Xenon volume before the first electrode foil that is outside of the effective volume. The geometry of the simulation target material is illustrated in Figure 7.5.

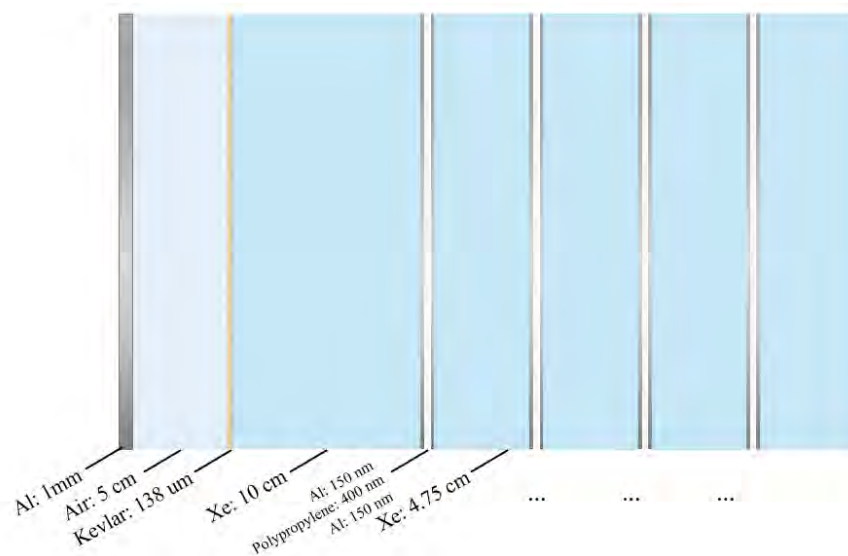


Figure 7.5: Dimensions and composition of SRIM target material based on ELOSS dimensions.

The factor of four difference in ΔE between that measured during E23508 and the SRIM simulation is likely to arise from a combination of different sources.

Below is a list of potential explanations for why the measured energy does not match the simulation:

1. The ion drift velocity is several orders of magnitude slower than the electron drift velocity. As a result, the real induced charge on the electrode foils connected to a

charge-sensitive preamplifier is expected to be about double the measured value.

2. There is a ballistic deficit from the preamplifier due to the short integration time/decay time compared to the electrode foils' pulse width.
3. There is signal loss from the long coax cables that take the preamplifier output to the shaping amplifier outside of the vault, which is over 100 m.
4. The preamplifier calibration is inaccurate because of changes in the environment or differences from channel to channel in the preamplifier. This also includes the RC circuit used to create a known voltage pulse for the calibration, which has a 5-10% tolerance.

The Shockley-Ramo theorem [59] states that current induced on an electrode from a moving point charge is given by

$$I = q\vec{v} \cdot \vec{E}_0(\vec{x}) \quad (7.1)$$

where \vec{v} is the velocity of the point charge q and $\vec{E}_0(\vec{x})$ is the weighting field. $\vec{E}_0(\vec{x})$ is the electric field when the signal electrode is at unit potential, while all other electrodes are at 0 V and there are no other charges. The induced current on the signal electrodes of ELOSS can be represented as

$$I(t) = \frac{q_e(t)v_e}{d} + \frac{q_{ion}(t)v_{ion}}{d} \quad (7.2)$$

where $q_e(t)$ and $q_{ion}(t)$ are the charge from electrons and ions, respectively, at time t . The drift velocities for electrons and ions in 850 Torr Xenon are represented by v_e and v_{ion} , while d is the sector thickness (distance between electrode foils). The charge of either electron

or ion can also be represented by number of electrons or ions times the charge of a single electron/ion, such as $q_e = -n_e e$ and $q_{ion} = n_{ion} e$.

By integrating the induced current $I(t)$ over the integration time of the preamplifier, a scalar can be found that relates the charge measured to the theoretical total charge Q_{theo} .

$$Q_{real} = \left(\frac{v_e}{d} t_{int} - \frac{1}{2} \frac{v_e^2}{d^2} t_{int}^2 + \frac{v_{ion}}{d} t_{int} - \frac{1}{2} \frac{v_{ion}^2}{d^2} t_{int}^2 \right) Q_{theo} \quad (7.3)$$

Since the integration time is longer than the electron pulse width, but shorter than the ion pulse width, i.e.:

$$\frac{d}{v_e} < t_{int} < \frac{d}{v_{ion}} \quad (7.4)$$

then Equation 7.3 can be reduced to

$$Q_{real} = \left(\frac{1}{2} + \frac{v_{ion}}{d} t_{int} - \frac{1}{2} \frac{v_{ion}^2}{d^2} t_{int}^2 \right) Q_{theo} \quad (7.5)$$

which makes Q_{real} just over half of Q_{theo} . Multiplying the ΔE measured with ELOSS by 1.89, the ratio of Q_{theo} to Q_{real} , an energy loss corrected for this effect is computed: 245.7 MeV.

Ballistic deficit can be mitigated by choosing a preamplifier with a long integration time in comparison to the width of input pulse, but pileup is more likely to occur. The time needed to collect all of the electrons is about 31 μs . With an integration between 30 μs and 100 μs , the ballistic deficit from the preamplifier is shown in Figure 7.6. Taking this into account, the corrected energy loss becomes 303-416 MeV depending on the integration time.

The coaxial cables attenuate around 0.13 dB/m for 100 MHz signals [60], which could

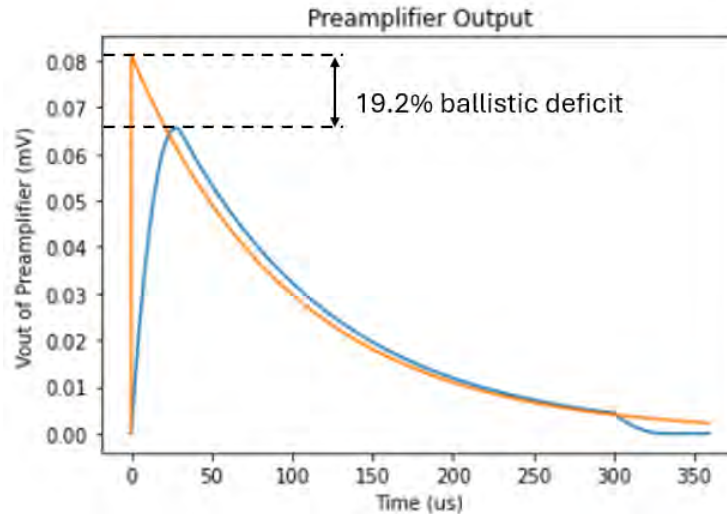


Figure 7.6: Orange plot is the preamplifier output if the input pulse was a delta function/integration time was infinite. Blue plot is an example preamplifier output with 100 μs integration time and input pulse $\sim 31 \mu\text{s}$ long.

significantly impact the signal reaching the shaping amplifier and then MCA outside of the Transfer Hall vault. The frequency of the preamplifier output signals for this experiment, along with the exact distance of the cables and what type of cables is unknown at this moment. Regardless, a 20% signal attenuation is realistic and enough to conclude ELOSS did initially measure 500 MeV of energy deposited, but lost a significant amount of signal during the pulse processing.

Lastly, taking into account the 10% uncertainty for the preamplifier calibration, the energy loss measured by ELOSS in E23508, once corrected, does agree with the energy loss provided by a SRIM simulation of ELOSS.

In the weeks after E23508 ended, much more was learned about ELOSS. One could argue that more was learned from another “unsuccessful” beam test than if ELOSS worked exactly as expected. No scintillation light was recorded, but why? The answer is actually pretty simple: The PMT anode sensitivity was far below expected because of a small bug in the voltage divider!

The external decoupling circuit for a ELOSS PMT has to connect directly to the PMT's anode. Figure 4.3 shows that this is the case for the ELOSS PMTs used in the previous two beam tests, but it also shows a voltage divider chain and a capacitor chain attached to the anode. Clearly the resistor chain needs to be connected to the anode to properly divide the voltage along the multiplication stage's dynodes. The capacitors, C1, C2, and C3, create a low impedance path for the high frequency anode signal. This is problematic because those capacitors are supposed to provide charge to the last few dynodes when they get depleted from high gain signals. The charge they supply to the dynodes, in this case, actually comes from the anode signal itself, meaning only a small fraction of the charge collected on the anode goes to decoupling circuit and rest of the DAQ. The anode charge dump into the voltage-divider instead of the readout can be fixed by disconnecting the C3 capacitor from the anode and grounding it.

In addition to disconnecting C3 from the anode and grounding it, further improvements can be made if C4 is lowered many orders of magnitude, R17 is increased and R18+C7 is removed to make the HV branch resistance 10 k Ω . Additionally, the drop down resistor in the decoupling circuit can be increased to 10 k Ω instead of 1 k Ω . This will reduce signal loss without introducing reflections. That changes the equivalent resistance after the decoupling capacitor C8 from 47 to 50 Ω . A comparison between the current PMT circuit and the newly proposed circuit are shown in Figure 7.7. The results of an LTspice simulation for each of the circuits is also shown in Figure 7.7, providing evidence that the new circuit design would improve PMT sensitivity several orders of magnitude.

Impedance matching and minimizing distortion from reflections was a main priority in the last redesign of the Decoupler Crate, but they might have worsened. 25 Ω coax cables go from the PMTs to the ELOSS Lid feedthrough, unknown impedance 25 pin Dsub cables

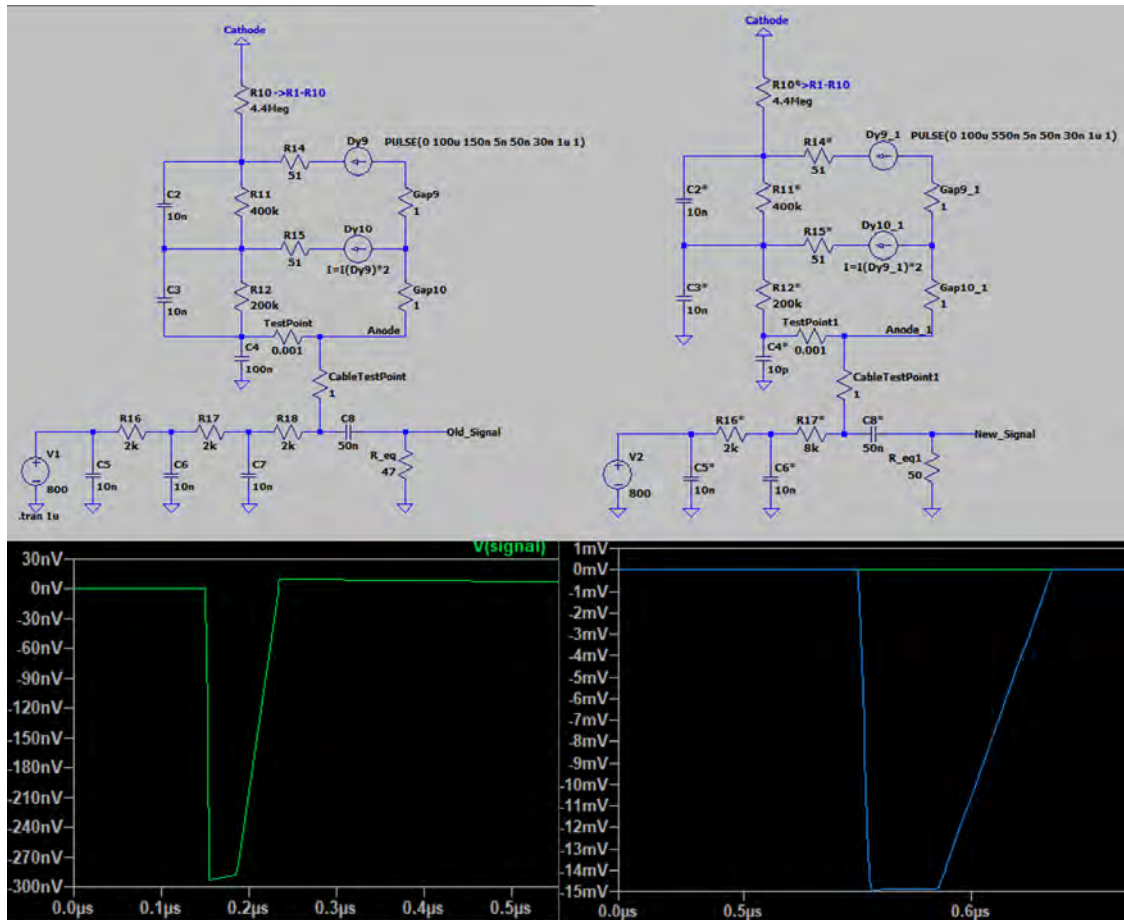


Figure 7.7: Comparison of the voltage-divider and readout circuit currently used in ELOSS (left) and the proposed redesign (right). Circuit model contains the last two multiplication stages, anode, and decoupler circuit. For the same input pulse, the redesigned circuit outputs a signal 50,000 times larger.

go from ELOSS to the Decoupler Crate, the PCBs inside the Decoupler Crate are 50Ω impedances, then a short flat ribbon cable of 100Ω connects the Decoupler Crate to the MDPPs where they get terminated at the 50Ω jumper input.

It is clear after simulating in LTSpice with conservative delay times and starting pulse width that impedance matches distort the PMT pulse before it is integrated by the MDPP32-QDC. More tests about how much signal is lost through this full transmission line need to be performed before a solution can be accepted. However, the first proposal is to use 100Ω impedance everywhere. Ribbon cable is the standard for 100Ω cable and is cheap. If the 25

Ω coax inside ELOSS could be replaced with 100 Ω ribbon cable, the signal could travel the majority of the way to the digitizer before reflecting. The decoupling PCBs could be rebuilt as 100 Ω signal traces instead of 50 Ω , then the terminating resistor on the MDPP gain jumper could be switched to 100 Ω . That would provide a completely impedance matched readout if the 25 pin Dsub cable is 100 Ω .

The problem with this plan is the strenuous requirements needed for the cables inside ELOSS. Ideally, the cables chosen would be 100 Ohm, rated for UHV, rated for 1 kV, and either coaxial or twisted pair that can be terminated with a 25 pin Dsub connector. So far, no such cable has been found that's commercially available. One of the top goals moving forward from this experiment is to understand what level of impedance mismatch can be tolerated and how to get to that point.

Discharges in Argon, during the PMT calibration, permanently damaged components in several channels of the MDPP32-QDCs. Xenon has a higher breakdown voltage than Argon at 750-850 Torr, consequently discharges occurred less often. Covering the PMT base PCBs in an insulating varnish likely contributed to less frequent breakdowns as well. Even though the PMTs were more stable in Xenon, many more channels defected in the days leading up to Experiment 23508. After the experiment, it was discovered that the decoupling capacitor (C8 in Figure 7.7) was only rated to 500 V. Therefore, sparks occurring at voltages around 700 or 800 V, release huge amounts of current and cause the capacitors to breakdown. If a QDC channel wasn't damaged immediately from the discharge, it was at least susceptible to leakage current passing through broken capacitor from then on.

Immediately following the beam test, Mesytec was able to examine the damaged modules and develop a special high protection gain jumper, which has the ability to "absorb" a discharge instead of destroying the components on the passing it on to the sensitive input

stage components. jumper and continue on to destroy components past the QDC input stage. If there are any more sparking PMTs, these gain jumpers will prevent the discharges from causing collateral damage. Additionally, the PCBs containing HV circuits, like the PMT voltage-divider, can be upgraded to include spark deterrent 1206 footprint pads. Extra precautions can be taken in the design of HV PCBs to eliminate sharp corners and provide adequate clearance between large potential differences. The pads going forward will have rounded edges and the solder mask will cover all 4 sides of the pad making the pad smaller as well.

Overall, it is quite clear that the fundamental concepts behind ELOSS work in this detector. With only a few small hardware changes to the PMT readout, what was a non-existent light response can become a new energy loss detector at FRIB with a flourishing optical readout. Moving forward in the development of ELOSS must include verification studies on the solutions presented at the end of this section. The simplest, most cost-effective and least time consuming approach to studying these issues is to use the ELOSS prototype.

7.3 Prototype Verification

The original ELOSS prototype, pictured in Figure 7.8, consisted of a small stainless steel vessel (X x X x X) with two pressure windows, two KF16 gas connections, and two conflat flanges used for electrical feedthroughs. Inside the vessel are four PCBs mounted around the perimeter of the effective area in the same orientation as ELOSS. Each PCB housed three PMTs and contained a voltage-divider circuit equivalent to the Hamamatsu-suggested circuit provided in the datasheet. The PMTs were all biased at the same voltage and the

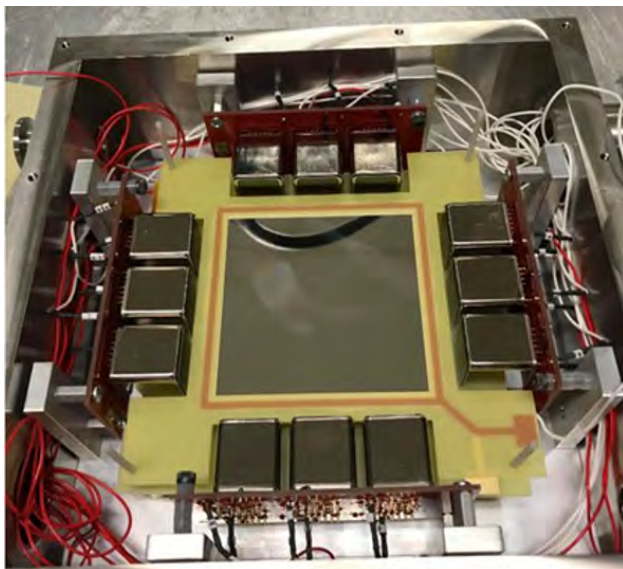


Figure 7.8: Prototype used to test the initial concepts for ELOSS. Consists of 12 PMTs with the decoupler circuit inside the prototype, such that each PMT needed a HV cable and signal cable.

signals readout individually. The PMTs operated at maximum sensitivity in this configuration, achieving output pulses with amplitudes on the order of Volts instead of millivolts. Small metalized polypropylene foils were supported in a sandwich-like configuration to act as the reflective electrode foils that separate the ELOSS sectors. To reduce the voltage needed to obtain a suitable electric field for stimulated electroluminescence a third foil could be added in between the boundary foils. Even without the middle foil, stimulated electroluminescence could be observed with an atmospheric Ar/Xe (95%/5%) mixture at a potential difference between outer foils as low as 100 V. Figure 7.9 shows the only picture of stimulated electroluminescence observed with the ELOSS prototype.

After the second beam test with ELOSS, the prototype was redesigned to investigate the light sensitivity problems uncovered by the first two beam tests. The idea was to restructure parts of the prototype to mirror the settings inside ELOSS as close as possible, but still have the convenience of testing on a much smaller and cheaper scale.

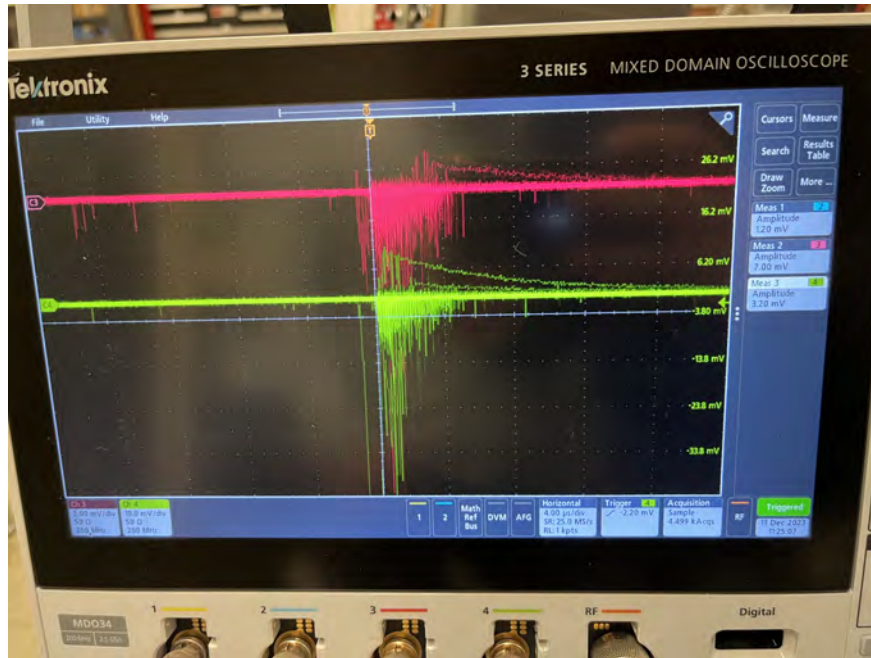


Figure 7.9: Picture of PMT responses to stimulated electroluminescence inside the prototype with an Ar/Xe mixture.

Steel plates with small Kevlar pressure windows closed the entrance and exit of the prototype volume. The conflat flange with 4 SHV feedthroughs was kept in place, only removing the wires that provided voltage to the PMTs. The circular 36-pin connector originally used for the PMT signals was replaced with the same 25-pin DSUB Allectra vacuum feedthrough installed on the ELOSS lid. A small length of Kapton-coated 26 conductor flat ribbon cable terminated with a 25-pin DSUB connector on one end and a custom 25-pin DSUB to solder pads adapter board on the other brought four HV biases in the prototype and transmitted four fast PMT signals out of the vessel. Inside the prototype, four RG13 coaxial cables delivered bias and readout signals for the four PMTs. Two of the PMT bases contained the exact circuit and PCB design used inside ELOSS for the last experiment and the other two consisted of the new design fixing the capacitor issue. The new boards were designed to impedance match, reduce discharges, and increase signal output. An additional PCB was designed for decoupling HV and output signals from the four PMTs. It contained four

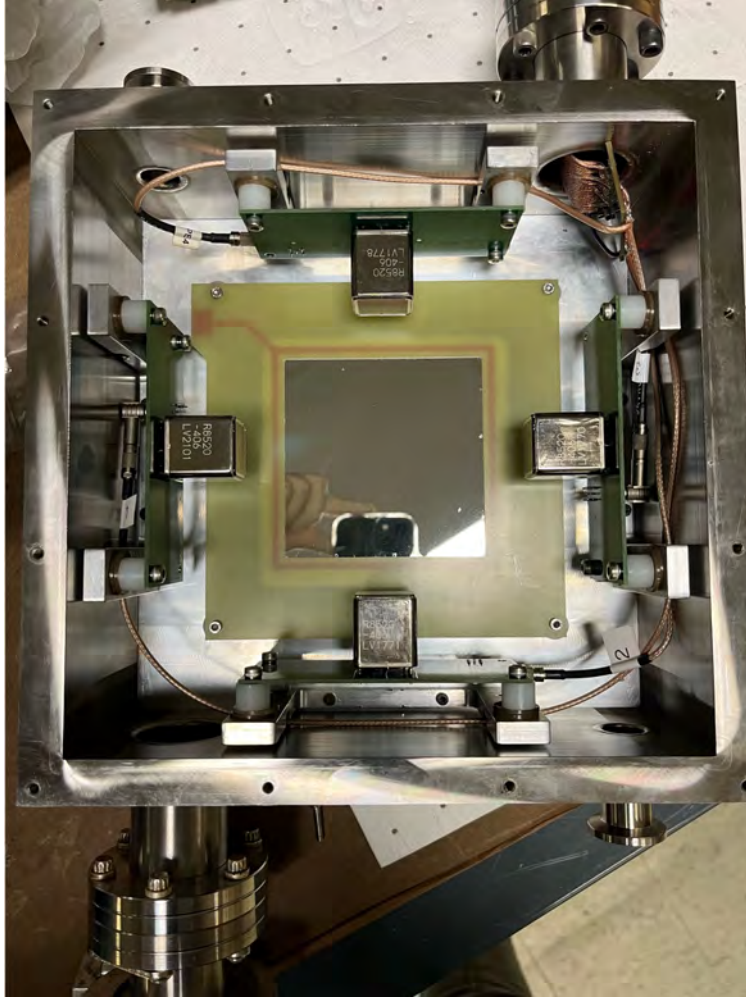


Figure 7.10: The same prototype structure as in Figure 7.8, but more accurate spacing of foils, redesigned PMT voltage-divider PCBs, external decoupling circuit, and coaxial PMT cables.

decoupler circuits, with two of them implementing the suggested changes in the last section and the other two being exact replicas as the current decoupler circuit used in ELOSS. The only difference being that the decoupling capacitor in all of the circuits was rated to 1000 V instead of 500 V.

Immediately upon biasing the PMTs, the differences in sensitivity were clear. PMTs utilizing the newly designed voltage-divider and decoupler circuit achieved single photoelectron sensitivity. The prototype was shielded from any light sources and the prototype was

filled with air and no radiation source inside. This meant the signals observed were from thermionic noise electrons being extracted from the photocathode, which is equivalent to one photoelectron. The pulse amplitudes observed were on the scale of 30-50 mV, compared to 20-40 mV amplitudes for thousands of photoelectrons in the current circuitry.

Next, the prototype was tested with an alpha source (^{241}Am) and CF_4 scintillating gas. Alphas from ^{241}Am have 5.5 MeV of energy, corresponding to a range of ~ 1.6 cm in CF_4 at 1 atm. The number of photons generated is proportional to amount of energy lost in between the reflective electrodes (effective volume). The alpha source was placed inside the prototype on a copper mask that replaced the top foil, so all 5.5 MeV would be deposited in the effective volume, maximizing the number of detectable photons. With a collection efficiency assumed to be around 10% because of only four PMTs, the average number of photons collected by a PMT was about 15 (using the full spectrum, 1100 photons/MeV) [57]. Taking into account the photodetection efficiency (QE of 0.27%), the number of photoelectrons measured on average is about 4. A new peak shows on the QDC spectrum of the long integration values for the two new designs, indicating that the PMTs are recording scintillation from alphas interacting with CF_4 , and it matches the expected energy loss. Meanwhile, the other two PMTs show nothing but cross talk. This is deemed a huge success as it shows there is a solution to the sensitivity issues that have plagued the performance of ELOSS in the last two fast beam tests. The results with the prototype to this point instill a great amount of confidence in the future of the detector and provide a clear path forward trying to assemble a fully functioning detector. Now that the external decoupling circuit has been successfully integrated into a prototype ELOSS optical readout, it can be tested in more realistic conditions such as with Xenon instead of CF_4 or in a low energy ion beam.

Chapter 8. Discussion

The Energy Loss Optical Scintillation System is a novel gaseous scintillation detector being developed for the advancement in atomic number identification at the S800 focal plane. By employing a high- Z , highly-luminescent gas (Xenon), a two-fold energy loss resolution improvement is expected, accompanied by at least a ten-fold counting rate increase. These improvements will enhance the PID capability of the S800 by allowing 3σ separation in Z from $Z = 50$ and predicted up to $Z = 92$, a region of the nuclear chart largely unexplored by the S800 due to currently limiting detector resolutions.

This thesis has introduced the $B\rho - \Delta E - ToF$ PID method utilized by the S800 spectrograph for identifying reaction products by their Z and A/Q on an event-by-event basis. The addition of a TKE measurement disentangles A and Q . The ΔE , currently measured by a multi-sampling Frisch grid-less ionization chamber in a parallel plate configuration, is limited to around $Z = 50$ in terms of Z -identification due to its maximum 1.2% σ energy loss resolution. By filling the ionization chamber with Krypton as opposed to P10, the energy resolution improved to 0.8% σ when tested with a low- Z cocktail beam. A group at the RIBF replaced P10 with Xenon in their ionization chamber to show further resolution improvement, capable of separating Z in the the Uranium range.

By moving to an optical readout-based detector, the signal-to-noise ratio is improved compared to the charge-induced foils of the ionization chamber. In addition, light propagation through Xenon is orders of magnitude faster than electron, and especially ion drift times, drastically decreasing the time it takes to record an event. This will not only increase the maximum event rate, but provide useful timing information due to its time resolution down

to 150 ps (σ) previously not fathomable with the ionization chamber. The advantages and characteristics of Xenon that have been detailed in Chapter 2 outline why the next generation ΔE -detector will include Xenon and how such a detector should be designed. This review is followed by the simulation-based design studies performed to finalize and optimize the design of ELOSS.

Once the design was settled, a description of the physical components of the detector such as the optical readout, mechanical structure, gas handling system and its unique interfaces is presented. It is at this point in the thesis that the bulk of original work starts since the concepts used for ELOSS were established long before and a design, supported by systematic simulation studies, had been proposed and accepted. The most time consuming portion of this graduate research, which unfortunately doesn't get an equivalent slice of the thesis text, is the work with the optical readout. A great effort was put forth to understand the innerworkings of general photomultiplier tubes, circuit and PCB design, and the Mesytec MDPP32-QDC to develop an optical readout capable of working with an external decoupler circuit. Additionally, the extensive knowledge gained led to increased safety measures in regards to the care and handling of the PMTs and associated electronics. It also led to increasingly more efficient, robust, adaptable, well documented circuit and PCB designs, in which the evolution of this proficiency could not be justly added into this thesis.

Chapters 5 and 6 are the subjects of two papers sent for review (neural network paper already accepted). The studies conducted in these chapters are expected to serve not just ELOSS, but other large-area gaseous scintillation detectors with many PMTs too. Chapter 7 is arguably the most important to this thesis, since it specifically details the status of the ELOSS detector at different points in time. Thus, it is the most representative of the development of a novel energy loss detector, which is the subject of this thesis. The rest of

this thesis will focus on the bright future of ELOSS.

The last chapter left off on a promising note indicating that the PMT sensitivity issues plaguing the two fast beam tests could be solved. It is true that the sensitivity has dramatically increased as a result of the redesigned PMT voltage-dividers, but there is still much more work to do before anything is ready to be implemented in ELOSS. First, before the PMT sensitivity can be considered “fixed”, scintillation generated from the excitation of Xenon needs to be measured by the new PMT readouts. Therefore, the ELOSS gas handling system and recovery system need to be connected to the prototype for testing with Xenon gas. Recording a signal pulse from a PMT exposed to Xenon scintillation will help guide redesign efforts going forward. Importantly, the signal amplitude vs number of expected photons needs to be measured along with the signal shape/width. This data will help validate simulation models and optimize parameters for the QDCs. The spark deterrent PCB design can be tested in Xenon as well to ensure discharges will no longer occur and damage electronics.

The prototype and working optical readout can be used to test a new calibration procedure. The test includes positioning an alpha source directly in the center of the effective area of the prototype. All steps must be taken to ensure that the light collection efficiency is identical from each PMTs’ perspective. With this, the PMTs can be gain matched in real time to each other. The procedure would gain match four PMTs at a time until all 120 have been tested in the prototype. That would be the first round. The second round would take one of the four PMTs in each batch (30 batches) and put them in the prototype to gain match. The PMTs in corresponding batches would be gain matched just as the representative PMT was. This tournament style calibration technique would continue until all PMTs are gain matched to the same anode sensitivity. Random samples of PMTs could be tested

afterward to check gain matching.

Along with this would be the design of a new PMT voltage-divider base that replaces the multi-PMT PCBs installed in the detector now (Figure 4.4). The major drawback of the PCB design currently being used is the inconvenience of having 5 to 10 PMTs on one board. Individual PMTs cannot be tested without putting the whole PCB inside a light-tight chamber, introducing many uncertainties associated with location of light source with respect to the PMT. Each PMT is also semi-permanently coupled to its housing on the board and subsequently its location in the detector because the calculated resistor ratio is populated according to that position. The better option is to design PCB bases for each PMT that is specific to each PMT, but can be connected anywhere, such that the base is just an extension of the PMT rather than a place holder for the PMT.

Aside from work with the physical optical readout, the simulation, modeling and DAQ can be improved immensely. The neural network studies in Chapter 6 only scratch the surface of what can be tested. One of the most interesting prospects is training the neural network with more realistic data. For example, training the DNN with real QDC channel outputs instead of photon counts from GEANT4 would inherently include the deviations in anode sensitivity and noise level. In addition, the inputs are now fixed to the range of the QDC (0-65635). The input nodes or input data could also be given a location attribute that would optimize the weights and biases in the first layer sooner making the same amount of training more effective since the DNN essentially has a head start. More studies must also be done on the effects of inactive and saturated PMTs. Specifically, studies need to focus on methods for artificially replacing PMTs that will preserve the neural network and ELOSS performance without having to do physical maintenance on the detector.

ELOSS is a next generation ΔE detector with exciting potential and it should be a focal

point of detector research and development efforts related to heavy-ion PID going forward.

BIBLIOGRAPHY

- [1] M. Cortesi, S. Dziubinski, A. Gade, R. Zegers, J. Pereira, J. Ascitutto, S. Lidia, and D. Bazin, “Design and construction of a novel energy-loss optical scintillation system (ELOSS) for heavyion particle identification,” *Review of Scientific Instruments*, vol. 93, p. 123305, 12 2022.
- [2] J. Wei *et al.*, “Accelerator commissioning and rare isotope identification at the Facility for Rare Isotope Beams,” *Mod. Phys. Lett. A*, vol. 37, no. 09, p. 2230006, 2022.
- [3] M. Cortesi, J. Pereira, S. Dziubinski, S. Lidia, R. Zegers, D. Bazin, G. Cerizza, J. Ascitutto, and A. Gade, “Upgrade to the focal-plane detector system of the s800 spectrograph at frib,” December 2023.
- [4] D. Bazin, J. Caggiano, B. Sherrill, J. Yurkon, and A. Zeller, “The s800 spectrograph,” *Nuclear Instruments and Methods in Physics Research Section B: Beam Interactions with Materials and Atoms*, vol. 204, pp. 629–633, 2003. 14th International Conference on Electromagnetic Isotope Separators and Techniques Related to their Applications.
- [5] J. Wei, C. Alleman, H. Ao, B. Arend, D. Barofsky, S. Beher, G. Bollen, N. Bultman, F. Casagrande, W. Chang, Y. Choi, S. Cogan, P. Cole, C. Compton, M. Cortesi, J. Curtin, K. Davidson, S. Di Carlo, X. Du, K. Elliott, B. Ewert, A. Facco, A. Fila, K. Fukushima, V. Ganni, A. Ganshyn, T. Ginter, T. Glasmacher, A. Gonzalez, Y. Hao, W. Hartung, N. Hasan, M. Hausmann, K. Holland, H. Hseuh, M. Ikegami, D. Jager, S. Jones, N. Joseph, T. Kanemura, S. Kim, C. Knowles, T. Konomi, B. Kortum, N. Kulkarni, E. Kwan, T. Lange, M. Larmann, T. Larter, K. Laturkar, M. LaVere, R. Laxdal, J. LeTourneau, Z.-Y. Li, S. Lidia, G. Machicoane, C. Magsig, P. Manwiller, F. Marti, T. Maruta, E. Metzgar, S. Miller, Y. Momozaki, M. Mugerian, D. Morris, I. Nesterenko, C. Nguyen, P. Ostroumov, M. Patil, A. Plastun, L. Popielarski, M. Portillo, A. Powers, J. Priller, X. Rao, M. Reaume, S. Rodriguez, S. Rogers, K. Saito, B. Sherrill, M. Smith, J. Song, M. Steiner, A. Stolz, O. Tarasov, B. Tousignant, R. Walker, X. Wang, J. Wenstrom, G. West, K. Witgen, M. Wright, T. Xu, Y. Yamazaki, T. Zhang, Q. Zhao, S. Zhao, P. Hurh, S. Prestemon, and T. Shen, “Technological developments and accelerator improvements for the frib beam power ramp-up,” *Journal of Instrumentation*, vol. 19, p. T05011, may 2024.
- [6] FRIB, “Detectors,” n.d. Accessed: 2025-03-03.
- [7] J. Pereira, “Modes of operation,” 2017. Accessed: 2025-04-08.
- [8] M. Portillo, B. Sherrill, Y. Choi, M. Cortesi, K. Fukushima, M. Hausmann, E. Kwan, S. Lidia, P. Ostroumov, R. Ringle, M. Smith, M. Steiner, O. Tarasov, A. Villari, and T. Zhang, “Commissioning of the advanced rare isotope separator aris at frib,” *Nuclear Instruments and Methods in Physics Research Section B: Beam Interactions with Materials and Atoms*, vol. 540, pp. 151–157, 2023.

- [9] F. Sauli, *Gaseous Radiation Detectors : Fundamentals and Applications*, vol. 36. Oxford University Press, 2015.
- [10] U. of Southampton, “Chapter 2: Rutherford scattering,” n.d. Accessed: 2025-04-13.
- [11] J. Swartz, “Detectors,” 2024. Accessed: 2025-04-13.
- [12] K. Meierbachtol, *PARALLEL AND PERPENDICULAR MOMENTUM DISTRIBUTIONS IN PROJECTILE FRAGMENTATION REACTIONS*. PhD thesis, Michigan State University, 2012.
- [13] W. Loveland, D. Morrissey, and G. Seaborg, *Modern Nuclear Chemistry*. John Wiley & Sons Inc., 2006.
- [14] J. Yurkon, D. Bazin, W. Benenson, D. Morrissey, B. Sherrill, D. Swan, and R. Swanson, “Focal plane detector for the s800 high-resolution spectrometer,” *Nuclear Instruments and Methods in Physics Research Section A: Accelerators, Spectrometers, Detectors and Associated Equipment*, vol. 422, no. 1, pp. 291–295, 1999.
- [15] M. Yoshimoto, N. Fukuda, R. Matsumura, D. Nishimura, H. Otsu, Y. Shimizu, T. Sumikama, H. Suzuki, H. Takahashi, H. Takeda, J. Tanaka, and K. Yoshida, “Xenon-gas ionization chamber to improve particle identification of heavy ion beams with $z_i \geq 70$,” 2024.
- [16] R. Strittmatter and B. Wehring, “Fragment atomic-number identification using a gas ionization chamber in fission yield measurements,” *Nuclear Instruments and Methods*, vol. 166, no. 3, pp. 473–481, 1979.
- [17] L. Canete, D. Doherty, G. Lotay, D. Seweryniak, C. Campbell, M. Carpenter, W. Catford, K. Chipps, J. Henderson, R. Izzard, R. Janssens, H. Jayatissa, J. Jos, A. Kennington, F. Kondev, A. Korichi, T. Lauritsen, C. Mller-Gatermann, C. Paxman, and S. Zhu, “Confirmation of a new resonance in si 26 and contribution of classical novae to the galactic abundance of al 26,” *Physical Review C*, vol. 108, 09 2023.
- [18] J. Lindhard and A. H. So/rensen, “Relativistic theory of stopping for heavy ions,” *Phys. Rev. A*, vol. 53, pp. 2443–2456, Apr 1996.
- [19] S. Kumar and P. Diwan, “Energy loss and straggling of α -particles in ag and sn metallic foils,” *Journal of Radiation Research and Applied Sciences*, vol. 8, no. 4, pp. 538–543, 2015.
- [20] H. Weick, H. Geissel, C. Scheidenberger, F. Attallah, D. Cortina, M. Hausmann, G. Mützenber, T. Radon, H. Schatz, K. Schmidt, J. Stadlmann, K. Sümmerer, and M. Winkler, “Drastic enhancement of energy-loss straggling of relativistic heavy ions due to charge-state fluctuations,” *Phys. Rev. Lett.*, vol. 85, pp. 2725–2728, Sep 2000.

- [21] M. Mutterer, P. Grimm, H. Heckwolf, J. Pannicke, W. Spreng, and J. P. Theobald, “Response of gas scintillators to heavy charged particles,” in *Detectors in Heavy-Ion Reactions* (W. von Oertzen, ed.), (Berlin, Heidelberg), pp. 63–79, Springer Berlin Heidelberg, 1983.
- [22] L. Kalousis, “Calibration of photomultiplier tubes,” *Journal of Instrumentation*, vol. 18, p. P07016, jul 2023.
- [23] HAMAMATSU, *PHOTOMULTIPLIER TUBES - Basics and Applications*.
- [24] K. Abe, K. Hiraide, K. Ichimura, Y. Kishimoto, K. Kobayashi, M. Kobayashi, S. Moriyama, M. Nakahata, H. Ogawa, K. Sato, H. Sekiya, T. Suzuki, O. Takachio, A. Takeda, S. Tasaka, M. Yamashita, B. Yang, N. Kim, Y. Kim, Y. Itow, K. Kanzawa, K. Masuda, K. Martens, Y. Suzuki, B. D. Xu, K. Miuchi, N. Oka, Y. Takeuchi, Y. Kim, K. Lee, M. Lee, Y. Fukuda, M. Miyasaka, K. Nishijima, K. Fushimi, G. Kanzaki, and S. Nakamura, “A measurement of the scintillation decay time constant of nuclear recoils in liquid xenon with the xmass-i detector,” *Journal of Instrumentation*, vol. 13, p. P12032, dec 2018.
- [25] C. Henriques, J. Teixeira, P. Silva, R. Mano, J. dos Santos, and C. Monteiro, “Understanding the xenon primary scintillation yield for cutting-edge rare event experiments,” *Journal of Cosmology and Astroparticle Physics*, vol. 2024, p. 041, jun 2024.
- [26] I. Murayama and S. Nakamura, “Time profile of the scintillation from liquid and gaseous xenon,” *Nuclear Instruments and Methods in Physics Research Section A: Accelerators, Spectrometers, Detectors and Associated Equipment*, vol. 763, pp. 533–537, 2014.
- [27] E. Morikawa, R. Reininger, P. Grtler, V. Saile, and P. Laporte, “Argon, krypton, and xenon excimer luminescence: From the dilute gas to the condensed phase,” *The Journal of Chemical Physics*, vol. 91, pp. 1469–1477, 08 1989.
- [28] A. Hitachi, T. Takahashi, N. Funayama, K. Masuda, J. Kikuchi, and T. Doke, “Effect of ionization density on the time dependence of luminescence from liquid argon and xenon,” *Phys. Rev. B*, vol. 27, pp. 5279–5285, May 1983.
- [29] O. Njoya, T. Tsang, M. Tarka, W. Fairbank, K. Kumar, T. Rao, T. Wager, S. A. Kharusi, G. Anton, I. Arnquist, I. Badhrees, P. Barbeau, D. Beck, V. Belov, T. Bhatta, J. Brodsky, E. Brown, T. Brunner, E. Caden, G. Cao, L. Cao, W. Cen, C. Chambers, B. Chana, S. Charlebois, M. Chiu, B. Cleveland, M. Coon, A. Craycraft, J. Dalmasson, T. Daniels, L. Darroch, S. Daugherty, A. De St. Croix, A. Der Mesrobian-Kabakian, R. DeVoe, M. Di Vacri, J. Dilling, Y. Ding, M. Dolinski, A. Dragone, J. Echevers, M. Elbeltagi, L. Fabris, D. Fairbank, J. Farine, S. Ferrara, S. Feyzbakhsh, R. Fontaine, A. Fucarino, G. Gallina, P. Gautam, G. Giacomini, D. Goeldi, R. Gornea, G. Gratta, E. Hansen, M. Heffner, E. Hoppe, J. Hl, A. House, M. Hughes, A. Iverson, A. Jamil, M. Jewell, X. Jiang, A. Karelin, L. Kaufman, D. Kodroff, T. Koffas,

- R. Krcken, A. Kuchenkov, Y. Lan, A. Larson, K. Leach, B. Lenardo, D. Leonard, G. Li, S. Li, Z. Li, C. Licciardi, Y. Lin, P. Lv, R. MacLellan, T. McElroy, M. Medina-Peregrina, T. Michel, B. Mong, D. Moore, K. Murray, P. Nakarmi, C. Natzke, R. Newby, Z. Ning, F. Nolet, O. Nusair, K. Odgers, A. Odian, M. Oriunno, J. Orrell, G. Ortega, I. Ostrovskiy, C. Overman, S. Parent, A. Piepke, A. Pocar, J.-F. Pratte, V. Radeka, E. Raguzin, S. Rescia, F. Retire, M. Richman, A. Robinson, T. Rossignol, P. Rowson, N. Roy, J. Runge, R. Saldanha, S. Sangiorgio, K. Skarpaas, A. Soma, G. St-Hilaire, V. Stekhanov, T. Stiegler, X. Sun, J. Todd, T. Tolba, T. Totev, R. Tsang, F. Vachon, V. Veeraraghavan, S. Viel, G. Visser, C. Vivo-Vilches, J.-L. Vuilleumier, M. Wagenpfeil, M. Walent, Q. Wang, M. Ward, J. Watkins, M. Weber, W. Wei, L. Wen, U. Wichoski, S. Wu, W. Wu, X. Wu, Q. Xia, H. Yang, L. Yang, Y.-R. Yen, O. Zeldovich, J. Zhao, Y. Zhou, and T. Ziegler, “Measurements of electron transport in liquid and gas xenon using a laser-driven photocathode,” *Nuclear Instruments and Methods in Physics Research Section A: Accelerators, Spectrometers, Detectors and Associated Equipment*, vol. 972, p. 163965, 2020.
- [30] R. Chandrasekharan, A. Knecht, M. Messina, C. Regenfus, and A. Rubbia, “High efficiency detection of argon scintillation light of 128 nm using laapds,” in *IEEE Nuclear Science Symposium Conference Record, 2005*, vol. 1, pp. 181–185, 2005.
- [31] R. Mano, C. Henriques, C. M. B. Monteiro, and J. Teixeira, “Studies of primary and secondary scintillation yield in krypton,” in *XeSAT2022 International Workshop on Applications of Noble Gas Xenon to Science and Technology*, (Coimbra, Portugal), May 2022. Accessed: 2025-04-13.
- [32] C. Henriques, J. Teixeira, P. Silva, R. Mano, J. dos Santos, and C. Monteiro, “Understanding the xenon primary scintillation yield for cutting-edge rare event experiments,” *Journal of Cosmology and Astroparticle Physics*, vol. 2024, p. 041, jun 2024.
- [33] A. Trindade, J. Escada, M. R. Silva, A. Marques, F. Borges, and F. Santos, “Absolute primary scintillation yield in gaseous xenon and in xenon trimethylamine mixtures,” *Nuclear Instruments and Methods in Physics Research Section A: Accelerators, Spectrometers, Detectors and Associated Equipment*, vol. 1049, p. 168038, 2023.
- [34] M. Saito, T. Nishikawa, and M. Miyajima, “Electric field dependence of luminescence due to alpha particles in gaseous xenon and the energy expended per photon,” *IEEE Transactions on Nuclear Science*, vol. 51, no. 5, pp. 2125–2130, 2004.
- [35] C. M. B. Monteiro, L. M. P. Fernandes, J. A. M. Lopes, L. C. C. Coelho, J. F. C. A. Veloso, J. M. F. dos Santos, K. Giboni, and E. Aprile, “Secondary scintillation yield in pure xenon,” *Journal of Instrumentation*, vol. 2, p. P05001, may 2007.
- [36] S. Agostinelli, J. Allison, K. Amako, J. Apostolakis, H. Araujo, P. Arce, M. Asai, D. Axen, S. Banerjee, G. Barrand, F. Behner, L. Bellagamba, J. Boudreau, L. Broglia, A. Brunengo, H. Burkhardt, S. Chauvie, J. Chuma, R. Chytracsek, G. Cooperman,

- G. Cosmo, P. Degtyarenko, A. Dell’Acqua, G. Depaola, D. Dietrich, R. Enami, A. Feli-
ciello, C. Ferguson, H. Fesefeldt, G. Folger, F. Foppiano, A. Forti, S. Garelli, S. Giani,
R. Giannitrapani, D. Gibin, J. Gmez Cadenas, I. Gonzlez, G. Gracia Abril, G. Greeni-
aus, W. Greiner, V. Grichine, A. Grossheim, S. Guatelli, P. Gumplinger, R. Hamatsu,
K. Hashimoto, H. Hasui, A. Heikkinen, A. Howard, V. Ivanchenko, A. Johnson, F. Jones,
J. Kallenbach, N. Kanaya, M. Kawabata, Y. Kawabata, M. Kawaguti, S. Kelner,
P. Kent, A. Kimura, T. Kodama, R. Kokoulin, M. Kossov, H. Kurashige, E. Lamanna,
T. Lampn, V. Lara, V. Lefebure, F. Lei, M. Liendl, W. Lockman, F. Longo, S. Magni,
M. Maire, E. Medernach, K. Minamimoto, P. Mora de Freitas, Y. Morita, K. Murakami,
M. Nagamatu, R. Nartallo, P. Nieminen, T. Nishimura, K. Ohtsubo, M. Okamura,
S. O’Neale, Y. Oohata, K. Paech, J. Perl, A. Pfeiffer, M. Pia, F. Ranjard, A. Rybin,
S. Sadilov, E. Di Salvo, G. Santin, T. Sasaki, N. Savvas, Y. Sawada, S. Scherer, S. Sei,
V. Sirotenko, D. Smith, N. Starkov, H. Stoecker, J. Sulkimo, M. Takahata, S. Tanaka,
E. Tcherniaev, E. Safai Tehrani, M. Tropeano, P. Truscott, H. Uno, L. Urban, P. Urban,
M. Verderi, A. Walkden, W. Wander, H. Weber, J. Wellisch, T. Wenaus, D. Williams,
D. Wright, T. Yamada, H. Yoshida, and D. Zschesche, “Geant4a simulation toolkit,”
*Nuclear Instruments and Methods in Physics Research Section A: Accelerators, Spec-
trometers, Detectors and Associated Equipment*, vol. 506, no. 3, pp. 250–303, 2003.
- [37] G. collaboration, “examples/extended/optical/lxe/src/lxedetectorconstruction.cc.”
- [38] E. Aprile and T. Doke, “Liquid xenon detectors for particle physics and astrophysics,”
Reviews of Modern Physics, vol. 82, p. 20532097, July 2010.
- [39] HAMAMATSU PHOTONICS K.K., *PHOTOMULTIPLIER TUBE R8520-406/R8520-
506*, Nov. 2021.
- [40] E. Aprile, K. Arisaka, F. Arneodo, A. Askin, L. Baudis, A. Behrens, E. Brown, J. Car-
doso, B. Choi, D. Cline, S. Fattori, A. Ferella, K. Giboni, A. Kish, C. Lam, R. Lang,
K. Lim, J. Lopes, T. Marrodn Undagoitia, Y. Mei, A. Melgarejo Fernandez, K. Ni,
U. Oberlack, S. Orrigo, E. Pantic, G. Plante, A. Ribeiro, R. Santorelli, J. dos Santos,
M. Schumann, P. Shagin, A. Teymourian, E. Tziaferi, H. Wang, and M. Yamashita,
“The xenon100 dark matter experiment,” *Astroparticle Physics*, vol. 35, no. 9, pp. 573–
590, 2012.
- [41] M. Instruments, “Model 722c dual convection-enhanced pirani capacitance manometer,”
n.d. Accessed: 2025-03-03.
- [42] N. Ackerman, J. Albert, M. Auger, D. Auty, I. Badhrees, P. Barbeau, L. Bartoszek,
E. Baussan, V. Belov, C. Benitez-Medina, T. Bhatta, M. Breidenbach, T. Brunner,
G. Cao, W. Cen, C. Chambers, B. Cleveland, R. Conley, S. Cook, and T. Ziegler,
“The exo-200 detector, part ii: auxiliary systems,” *Journal of Instrumentation*, vol. 17,
p. P02015, 02 2022.
- [43] P. University, “Xenon properties,” n.d. Accessed: 2025-03-03.

- [44] W. Ziegler, J. Mullins, and A. Berquist, “Calculation of the vapor pressure and heats of vaporization and sublimation of liquids and solids below one atmosphere pressure. viii. xenon,” *Eng. Exp. Stn.*, 1966.
- [45] H. H. Podgurski and F. N. Davis, “Thermal transpiration at low pressure. the vapor pressure of xenon below 90k.,” *The Journal of Physical Chemistry*, vol. 65, no. 8, pp. 1343–1348, 1961.
- [46] A. GRTTER and J. C. SHORROCK, “Vapour pressures of xenon (77180 k) and krypton (77130 k),” *Nature*, vol. 204, pp. 1084–1085, 1964.
- [47] M. Instruments, “103170027sh - product information,” n.d. Accessed: 2025-03-03.
- [48] K. J. L. Company, “423-imag cold cathode gauge,” n.d. Accessed: 2025-03-03.
- [49] mesytec GmbH & Co., *Software Module MDPP32-QDC*.
- [50] Tektronix, *Arbitrary Function Generators - AFG3000C Series Datasheet*, December 2012.
- [51] Silanna UV, *SF1 Series Far UV-C Light Emitting Diode*, July 2023.
- [52] H. Claus, “Ozone generation by ultraviolet lamps,” *Photochemistry and Photobiology*, vol. 97, no. 3, pp. 471–476, 2021.
- [53] P. Schneider and F. Xhafa, “Biographies,” in *Anomaly Detection and Complex Event Processing over IoT Data Streams*, Academic Press, 2022.
- [54] V. N. Gudivada and K. Arbabifard, “Chapter 3 - open-source libraries, application frameworks, and workflow systems for nlp,” in *Computational Analysis and Understanding of Natural Languages: Principles, Methods and Applications* (V. N. Gudivada and C. Rao, eds.), vol. 38 of *Handbook of Statistics*, pp. 31–50, Elsevier, 2018.
- [55] P. Janardhanan, “Project repositories for machine learning with tensorflow,” *Procedia Computer Science*, vol. 171, pp. 188–196, 2020. Third International Conference on Computing and Network Communications (CoCoNet’19).
- [56] T. Le-Duc, H. Nguyen-Xuan, and J. Lee, “Sequential motion optimization with short-term adaptive moment estimation for deep learning problems,” *Engineering Applications of Artificial Intelligence*, vol. 129, p. 107593, 2024.
- [57] A. Pansky, A. Breskin, A. Buzulutskov, R. Chechik, V. Elkind, and J. Va’vra, “The scintillation of cf4 and its relevance to detection science,” *Nuclear Instruments and Methods in Physics Research Section A: Accelerators, Spectrometers, Detectors and Associated Equipment*, vol. 354, no. 2, pp. 262–269, 1995.

- [58] F. P. Santos, T. H. V. T. Dias, A. D. Stauffer, and C. A. N. Conde, “Three-dimensional monte carlo calculation of the vuv electroluminescence and other electron transport parameters in xenon,” *Journal of Physics D: Applied Physics*, vol. 27, p. 42, jan 1994.
- [59] Z. He, “Review of the shockleyramo theorem and its application in semiconductor gamma-ray detectors,” *Nuclear Instruments and Methods in Physics Research Section A: Accelerators, Spectrometers, Detectors and Associated Equipment*, vol. 463, no. 1, pp. 250–267, 2001.
- [60] G. F. Knoll, *Radiation detection and measurement; 4th ed.* New York, NY: Wiley, 2010.

APPENDIX A. Channel Mapping

TBA: GitHub link with all of my code.

Slot	HV Channel	HV Adapter	HV Adapter Pin (In)	Decoupler Board	Decoupler Circuit (HV)	Decoupler Circuit (PMT)	Cable Pin	PMT Location	PMT Serial	Decoupler Circuit (Sig)	IDC Pin	IDC Pin	MDPP Module	MDPP Channel
5	16	4	TB2_2	4	9	9 C	2 S1-B1	LV2050	9	4	9	0x0001	24	
5	18	4	TB2_3	4	10	10 C	3 S1-B2	LV2029	10	4	10	0x0001	25	
5	20	4	TB2_4	4	11	11 C	4 S1-B3	LV2060	11	4	11	0x0001	26	
5	1	4	TB2_5	4	12	12 C	5 S1-B4	LV2148	12	4	12	0x0001	27	
5	3	4	TB2_6	4	13	13 C	6 S1-B5	LV2125	13	4	13	0x0001	28	
8	47	8	TB2_2	8	9	9 A	1 S1-L1	LV2098	9	8	9	0x0003	24	
8	46	8	TB2_3	8	10	10 A	2 S1-L2	LV2117	10	8	10	0x0003	25	
8	45	8	TB2_4	8	11	11 A	3 S1-L3	LV2064	11	8	11	0x0003	26	
8	43	8	TB2_5	8	12	12 A	4 S1-L4	LV2087	12	8	12	0x0003	27	
8	16	7	TB2_2	7	9	9 A	5 S1-L5	LV2165	9	7	9	0x0003	8	
8	18	7	TB2_3	7	10	10 A	6 S1-L6	LV2192	10	7	10	0x0003	9	
8	2	7	TB1_2	7	2	2 B	25 S1-L7	LV2131	2	7	2	0x0003	1	
8	4	7	TB1_3	7	3	3 B	24 S1-L8	LV2075	3	7	3	0x0003	2	
8	6	7	TB1_4	7	4	4 B	23 S1-L9	LV2140	4	7	4	0x0003	3	
8	8	7	TB1_5	7	5	5 B	22 S1-L10	LV2194	5	7	5	0x0003	4	
1	26	3	TB1_7	3	7	7 D	4 S1-R1	LV2123	7	3	7	0x0001	6	
1	24	3	TB1_6	3	6	6 D	3 S1-R2	LV1760	6	3	6	0x0001	5	
1	25	3	TB1_5	3	5	5 D	2 S1-R3	LV2077	5	3	5	0x0001	4	
1	27	3	TB1_4	3	4	4 D	1 S1-R4	LV2186	4	3	4	0x0001	3	
1	12	1	TB1_7	1	7	7 E	1 S1-R5	LV2190	7	1	7	0x0000	6	
1	14	1	TB1_8	1	8	8 E	2 S1-R6	LV2187	8	1	8	0x0000	7	
1	16	1	TB2_2	1	9	9 E	3 S1-R7	LV2095	9	1	9	0x0000	8	
1	18	1	TB2_3	1	10	10 E	4 S1-R8	LV2091	10	1	10	0x0000	9	
1	20	1	TB2_4	1	11	11 E	5 S1-R9	LV1785	11	1	11	0x0000	10	
5	14	4	TB1_8	4	8	8 C	1 S1-R10	LV2100	8	4	8	0x0001	23	
8	10	7	TB1_6	7	6	6 B	21 S1-T1	LV2138	6	7	6	0x0003	5	
8	12	7	TB1_7	7	7	7 B	20 S1-T2	LV2085	7	7	7	0x0003	6	
1	32	3	TB2_3	3	10	10 D	7 S1-T3	LV1762	10	3	10	0x0001	9	
1	30	3	TB2_2	3	9	9 D	6 S1-T4	LV2177	9	3	9	0x0001	8	

Figure A.1

Slot	HV Channel	HV Adapter	HV Adapter Pin (In)	Decoupler Board	Decoupler Circuit (HV)	Decoupler Circuit (PMT)	Cable	PMT Pin Location	PMT Serial	Decoupler Circuit (Sig)	IDC Pin	IDC Module	IDPP Channel
5	38	6	TB2_6	6	13	13 B	14 S2-T4	LV2086	13	6	13	0x0002	28
5	36	6	TB2_5	6	12	12 B	15 S2-T5	LV2119	12	6	12	0x0002	27
5	45	5	TB2_4	5	11	11 C	14 S3-B1	LV2200	11	5	11	0x0002	10
5	46	5	TB2_3	5	10	10 C	15 S3-B2	LV2083	10	5	10	0x0002	9
5	47	5	TB2_2	5	9	9 C	16 S3-B3	LV2079	9	5	9	0x0002	8
5	23	5	TB1_8	5	8	8 C	17 S3-B4	LV2176	8	5	8	0x0002	7
5	22	5	TB1_7	5	7	7 C	18 S3-B5	LV2136	7	5	7	0x0002	6
8	0	7	TB1_1	7	1	1 A	13 S3-L1	LV2139	1	7	1	0x0003	0
8	23	8	TB1_8	8	8	8 A	14 S3-L2	LV2047	8	8	8	0x0003	23
8	22	8	TB1_7	8	7	7 A	15 S3-L3	LV2054	7	8	7	0x0003	22
8	21	8	TB1_6	8	6	6 A	16 S3-L4	LV2162	6	8	6	0x0003	21
8	19	8	TB1_5	8	5	5 A	17 S3-L5	LV2159	5	8	5	0x0003	20
8	17	8	TB1_4	8	4	4 A	18 S3-L6	LV2147	4	8	4	0x0003	19
1	31	3	TB1_2	3	2	2 B	13 S3-L7	LV2171	2	3	2	0x0001	1
1	33	3	TB1_1	3	1	1 B	12 S3-L8	LV2069	1	3	1	0x0001	0
5	28	6	TB1_8	6	8	8 B	11 S3-L9	LV2145	8	6	8	0x0002	23
5	26	6	TB1_7	6	7	7 B	10 S3-L10	LV2106	7	6	7	0x0002	22
5	12	4	TB1_7	4	7	7 D	19 S3-R1	LV2096	7	4	7	0x0001	22
1	29	3	TB1_3	3	3	3 D	18 S3-R2	LV2178	3	3	3	0x0001	2
1	39	2	TB2_7	2	14	14 D	17 S3-R3	LV2089	14	2	14	0x0000	29
1	41	2	TB2_6	2	13	13 D	16 S3-R4	LV2160	13	2	13	0x0000	28
1	43	2	TB2_5	2	12	12 D	15 S3-R5	LV2152	12	2	12	0x0000	27
1	0	1	TB1_1	1	1	1 E	11 S3-R6	LV2081	1	1	1	0x0000	0
1	2	1	TB1_2	1	2	2 E	12 S3-R7	LV2034	2	1	2	0x0000	1
1	4	1	TB1_3	1	3	3 E	13 S3-R8	LV2175	3	1	3	0x0000	2
1	46	2	TB2_3	2	10	10 E	14 S3-R9	LV2071	10	2	10	0x0000	25
5	37	5	TB2_8	5	15	15 C	13 S3-R10	LV2120	15	5	15	0x0002	14
5	24	6	TB1_6	6	6	6 B	9 S3-T1	LV2126	6	6	6	0x0002	21
5	25	6	TB1_5	6	5	5 B	8 S3-T2	LV2063	5	6	5	0x0002	20

Figure A.3

5	6	4	TB1_4	4	4	4	4	D	22 S3-T3	LV2062	4	4	4	0x0001	19
5	8	4	TB1_5	4	4	5	5	D	21 S3-T4	LV2090	5	4	5	0x0001	20
5	10	4	TB1_6	4	4	6	6	D	20 S3-T5	LV2122	6	4	6	0x0001	21
5	35	5	TB2_9	5	16	16	16	C	25 S4-B1	LV2128	16	5	16	0x0002	15
5	11	5	TB1_1	5	1	1	1	C	24 S4-B2	LV2167	1	5	1	0x0002	0
5	13	5	TB1_2	5	2	2	2	C	23 S4-B3	LV2031	2	5	2	0x0002	1
5	15	5	TB1_3	5	3	3	3	C	22 S4-B4	LV2065	3	5	3	0x0002	2
5	17	5	TB1_4	5	4	4	4	C	21 S4-B5	LV2144	4	5	4	0x0002	3
5	31	6	TB1_2	6	2	2	2	B	5 S4-L1	LV2094	2	6	2	0x0002	17
5	29	6	TB1_3	6	3	3	3	B	6 S4-L2	LV2067	3	6	3	0x0002	18
5	27	6	TB1_4	6	4	4	4	B	7 S4-L3	LV2066	4	6	4	0x0002	19
8	41	8	TB2_6	8	13	13	13	A	25 S4-L4	LV2163	13	8	13	0x0003	28
8	39	8	TB2_7	8	14	14	14	A	24 S4-L5	LV2030	14	8	14	0x0003	29
8	37	8	TB2_8	8	15	15	15	A	23 S4-L6	LV2164	15	8	15	0x0003	30
8	35	8	TB2_9	8	16	16	16	A	22 S4-L7	LV2174	16	8	16	0x0003	31
8	11	8	TB1_1	8	1	1	1	A	21 S4-L8	LV2078	1	8	1	0x0003	16
8	13	8	TB1_2	8	2	2	2	A	20 S4-L9	LV2052	2	8	2	0x0003	17
8	15	8	TB1_3	8	3	3	3	A	19 S4-L10	LV2093	3	8	3	0x0003	18
5	19	5	TB1_5	5	5	5	5	C	20 S4-R1	LV2127	5	5	5	0x0002	4
5	21	5	TB1_6	5	6	6	6	C	19 S4-R2	LV2057	6	5	6	0x0002	5
1	17	2	TB1_4	2	4	4	4	E	20 S4-R3	LV2137	4	2	4	0x0000	19
1	19	2	TB1_5	2	5	5	5	E	19 S4-R4	LV2184	5	2	5	0x0000	20
1	21	2	TB1_6	2	6	6	6	E	18 S4-R5	LV2188	6	2	6	0x0000	21
1	22	2	TB1_7	2	7	7	7	E	17 S4-R6	LV2191	7	2	7	0x0000	22
1	23	2	TB1_8	2	8	8	8	E	16 S4-R7	LV2073	8	2	8	0x0000	23
1	47	2	TB2_2	2	9	9	9	E	15 S4-R8	LV2092	9	2	9	0x0000	24
5	4	4	TB1_3	4	3	3	3	D	23 S4-R9	LV2074	3	4	3	0x0001	18
5	2	4	TB1_2	4	2	2	2	D	24 S4-R10	LV2124	2	4	2	0x0001	17
5	0	4	TB1_1	4	1	1	1	D	25 S4-T1	LV2199	1	4	1	0x0001	16
5	40	6	TB2_7	6	14	14	14	B	1 S4-T2	LV2084	14	6	14	0x0002	29
5	42	6	TB2_8	6	15	15	15	B	2 S4-T3	LV2169	15	6	15	0x0002	30
5	44	6	TB2_9	6	16	16	16	B	3 S4-T4	LV2155	16	6	16	0x0002	31
5	33	6	TB1_1	6	1	1	1	B	4 S4-T5	LV2146	1	6	1	0x0002	16

Figure A.4

APPENDIX B. Arduino Motor Controller Code